

**The South American Subduction Zone: A study of
Rheological Parameters using 3D Finite Element
Modelling**

Dissertation

zur Erlangung des akademischen Grades doctor rerum naturalium
(Dr. rer. nat.)

vorgelegt dem Rat der Chemisch-Geowissenschaftlichen Fakultät der
Friedrich-Schiller-Universität Jena

von M.Sc.-Mathematics, Rekha Sharma
geboren am 13.10.1980 in Panipat, Indien

Gutachter

1. PD Dr. Thomas Jahr, FSU Jena
2. Prof. Dr. Gerhard Jentzsch, FSU Jena
3. Prof. Dr. Hans-Jürgen Götze, CAU Kiel

Tag der öffentlichen Verteidigung: 20 September 2013

**The South American Subduction Zone: A study of
Rheological Parameters using 3D Finite Element
Modelling**

Dissertation

for the obtainment of the academic degree doctor rerum naturalium
(Dr. rer. nat.)

submitted to the Council of the Faculty of Chemistry and Geosciences
of the Friedrich-Schiller-University Jena

by M.Sc.-Mathematics, Rekha Sharma
born on 13.10.1980 in Panipat, India

This dissertation is dedicated to my husband and son.

Zusammenfassung

Subduktion an Plattenrändern umfasst eine Vielzahl komplexer Prozesse. Zum Verständnis dieser Prozesse ist fundiertes Wissen über Materialparameter und kombinierte mechanische Effekte der Plattenbewegung nötig. Die Südamerikanische Subduktionszone zählt zu den interessantesten Subduktionszonen überhaupt. Das Abtauchen der ozeanischen Nazcaplatte unter die Südamerikaplatte führten zur Entstehung der Anden entlang der westlichen Plattengrenze Südamerikas. Es gibt Hinweise, dass die regionale Rheologie und die physikalischen Parameter wie Trench-Geometrie, Kopplung zwischen den Platten, Abtauchwinkel, Geschwindigkeit der überschiebenden Platte, etc., Einfluss auf die großräumige tektonische Deformation haben.

In dieser Arbeit wurden 3D finite Elemente Modelle entwickelt, um die Rheologie der Südamerikanischen Subduktionszone zu untersuchen. Der Einfluss von kombinierten mechanischen Prozessen der Plattenbewegung und der Kopplungsintensität zwischen den Platten auf die Deformationen ist hier von besonderem Interesse. Zusätzlich werden Korrelationen zwischen Deformationen in der oberen Platte und physikalischen Parametern, z.B. kontinentale Krustenmächtigkeit, kontinentale Plattengeschwindigkeit, Abtauchwinkel, sowie schiefe Plattenkonvergenz, untersucht. Dazu werden unterschiedliche Reibungskoeffizienten in der Kopplungszone und unterschiedliche Randbedingungen angesetzt.

Für die numerischen Tests werden zwei Segmente der südamerikanischen Subduktionszone mit unterschiedlicher Geometrie ausgewählt, die durch den Hangwinkel (α) und den mittleren Abtauchwinkel (β) charakterisiert sind. Das erste Modellierungsgebiet beschreibt die nördlichen Anden (20°S-25°S) mit $\alpha = 4.7^\circ$ und dem steilen Abtauchwinkel $\beta = 18.4^\circ$ während das südliche Modellierungsgebiet die Anden im Bereich 36°S - 40°S mit $\alpha = 2.3^\circ$ und dem flachen Abtauchwinkel $\beta = 13.4^\circ$ darstellt. Beide Modell-Varianten bestehen aus sechs homogenen Einheiten mit unterschiedlichen rheologischen Parametern. Die Kopplungszone zwischen den Platten reicht von ca. 10 km bis ca. 50 km Tiefe. Die Reibungszone hat deshalb eine Länge von 126 km für das nördliche Modell und 172 km für das südliche Modell. Die Modelle resultieren in Deformationen in der überschiebenden Platte für eine Modelllaufzeit von 500000 Jahren. Einerseits

ist diese Laufzeit kurz genug im Vergleich zum Prozess der Gebirgsbildung und andererseits ist sie lang genug um großräumige Deformationen zu modellieren.

Die Sensitivitäts-Analyse für das nördliche Andenmodell zeigt, dass ein Reibungskoeffizient von $\mu = 0.14$ in der Kopplungszone in 500000 Jahren eine Hebung von 103 m im Bereich des Altiplano-Plateaus verursacht, entsprechend einer Hebungsrate von 0.2 mm/yr für das Anden-Plateau. Dies stimmt gut mit geologisch bestimmten Hebungsraten für das Plateau überein. Weiterhin passt dieser Koeffizient gut zu anderen numerischen Abschätzungen.

Unter Ansatz einer Zug-Geschwindigkeit (slab pull velocity) an der abtauchenden Platte tritt eine Hebung in der oberen Platte nur auf, wenn sich diese mit mehr als 2 cm/yr in Trenchrichtung bewegt. Bei Geschwindigkeiten kleiner als 2 cm/yr überwiegt die Zugkraft der abtauchenden Platte und es kommt zu keiner Hebung in der oberen Platte. Eine Erhöhung des Reibungskoeffizienten in der Kopplungszone reduziert die Hebungsrate.

Wird nur die Zugkraft (slab pull) angesetzt, tritt keine Hebung in der Oberplatte auf. Die Kombination aus slab pull Geschwindigkeit und Gravitation verursacht Subsidenz in der Oberplatte für alle Reibungskoeffizienten ($\mu = 0.1, 0.2, 0.5$). Bei Vernachlässigung der Reibung ($\mu = 0.0$) zeigt das Modell eine geringere Hebung in Trench-Nähe, während höhere Reibung eine verstärkte Subsidenz bewirkt.

Es ist eine Korrelation zwischen der Hebung und der Mächtigkeit der oberen Platte festzustellen, geringere Mächtigkeit führt zu stärkerer Hebung. Für das Modell mit dünner kontinentaler Kruste (40 km) führt beispielsweise ein Reibungskoeffizient zwischen 0.3 und 0.35 zu einer Hebungsrate von 0.2 mm/yr im Altiplano-Plateau.

Der Abtauchwinkel der subduzierenden Platte spielt eine wichtige Rolle für die Deformationsraten in der Oberplatte. Im Vergleich mit dem nördlichen Andenmodell mit $\beta = 18.4^\circ$ zeigt das südliche Andenmodell mit $\beta = 13.4^\circ$ geringere Hebung im fore-arc jedoch stärkere Hebung im back-arc Bereich. Eine schief angesetzte Plattenbewegung der Nazcaplatte führt zu Subsidenz in der Oberplatte.

Die Sensitivitäts-Analyse zeigt, dass die Randbedingungen die Mechanik der Kopplungszone steuern. Die Deformationen in der oberen Platte hängen stark von den gewählten Randbedingungen ab. Daher tragen die Ergebnisse dieser Arbeit

wesentlich zu einem besseren Verständnis der Komplexität der geodynamischen Prozesse in der Südamerikanischen Subduktionszone bei. Dies gilt ebenso für vereinfachte wie auch für auf realistischer Geometrie basierende Modelle. Die geometrischen Parameter (z.B. Abtauchwinkel, Alter der subduzierenden Platte, kontinentale Krustenmächtigkeit) haben starke Auswirkungen auf die Deformationen in der überschiebenden Platte. Daher sollten die Randbedingungen möglichst realistisch aus geologischen und geophysikalischen Methoden abgeleitet eingehen um damit das Verständnis der komplexen Prozesse in Subduktionszonen durch geodynamische Modellierungen weiterhin zu erhöhen.

Summary

Subduction at plate margins is a complex process and its understanding requires a thorough knowledge of the material parameters and the mechanical effects of the plate movement. One of the most interesting subduction zone is the South American subduction zone which is formed due to the subduction of oceanic Nazca plate beneath the South American continental plate. This oceanic-continental subduction results in the formation of the Andean mountain belts along the western margin of the South American plate. There are evidences of regional rheological control and the influence of physical parameters such as strength of coupled plate interface, overriding plate movement, and the slab dip on the first order tectonic deformation.

In this project, 3D finite element modelling is carried out to test the rheology of the South American subduction zone by means of the commercial software package Abaqus. The combined mechanical effect of the plate movement and the strength of the coupled plate interface on the development of the overriding plate deformation are of primary interest. In addition, correlation between the overriding plate deformation and the physical parameters (thickness of the continental crust, continental drift velocity, convergence obliquity, and dip of subducting slab) are also tested.

Two study areas, one from the Northern Andes (20°S-25°S) and another from the Southern Andes (36°S-40°S) having different geometric features are chosen. Both geometries are constrained with the average slope angle (α) and average slab dip angle (β). Both models contain six homogeneous units with different rheological parameters. A frictionally coupled zone is assigned between the subducting and the overriding plate with average updip and downdip limit of 10 km and 50 km, respectively. The frictionally coupled zone is 126 km wide in the Northern Andean segment model and 172 km wide in the Southern Andean segment model. The strength of the frictionally coupled zone is assigned by applying different coefficients of friction. Subduction is simulated by applying velocity boundary conditions. The overriding plate deformation is calculated for the period of 500000 years. Though this time period is short as compared to the geological time span, but is sufficient to observe first order deformation pattern.

The sensitivity analysis of the Northern Andean model shows that the increase in strength of the frictionally coupled zone only amplifies the drag of the subducting plate and decreases the amount of uplift of the overriding plate. The coefficient of friction ($\mu = 0.14$) produces the geological estimated uplift rate of 0.2 mm/yr for the Altiplano plateau region. The calculated coefficient of friction also fits well to the other numerical estimates for the Northern Andes.

The combined mechanical effects of slab pull velocity and the gravity force create subsidence in the overriding plate for all coefficients of friction ($\mu = 0.1, 0.2, 0.5$). The overriding plate subsidence increases with increase in coefficient of friction. In the case of frictionless plate interface ($\mu = 0.0$), the model shows a little uplift only close to the trench. The oblique subduction of subducting plate leads to subsidence in the overriding plate for all coefficients of friction ($\mu = 0.0, 0.1, 0.2, 0.5$).

The uplift in the overriding plate was generated when the trenchward overriding plate moves with the rate ≥ 2 cm/yr. Trenchward overriding plate movement rate ≤ 2 cm/yr does not overcome the dragging effect of the subducting plate and fails to generate overriding plate uplift.

The uplift of the overriding plate is observed to be dependent on its crustal thickness. Decrease in the crustal thickness of the overriding plate implies increase in its uplift. The Northern Andean model with thin continental crust (40 km) requires a higher coefficient of friction ($0.3 < \mu < 0.35$) to produce the geological estimated uplift rate of 0.2 mm/yr for the Altiplano plateau.

The dip angle of the subducting slab is observed as an important parameter for controlling the overriding plate deformation pattern. The Southern Andean model with shallower dip angle ($\beta = 13.4^\circ$) produces lower uplift in the fore-arc region but higher uplift in the back-arc region as compared to the Northern Andean model having a steep slab dip angle ($\beta = 18.4^\circ$).

The present study shows that the boundary conditions and the physical parameters regulate the mechanics of the frictionally coupled zone and in turn, the overriding plate deformation. Hence, the findings of this study will be helpful in further understanding of the complexity of geodynamic processes of the South American subduction zone based on realistic geometry as well as for the general subduction zone related investigations. The physical parameters such as thickness of the

continental crust and the slab dip have strong influence on the overriding plate deformation. These constraints should be derived in most realistic sense by using a multidisciplinary integrative approach using geological observations and geophysical studies in order to further increase the understanding of the complex processes of subduction zones by geodynamic modelling.

Contents

Zusammenfassung	I
Summary	IV
1 Introduction	1
2 The South America subduction zone	12
2.1 Tectonic setting	12
2.1.1 Northern/Central Andes	13
2.1.2 Southern Andes	15
2.2 Available data	16
2.2.1 Seismic velocity model	16
2.2.2 Uplift estimation	18
3 Basic Theories	19
3.1 Continuum mechanics and Rheology	19
3.2 Rheological classes	21
3.2.1 Elastic rheology	21
3.2.2 Plastic rheology	22
3.2.3 General yield criterion	23
3.2.4 Mohr-Coulomb criterion	23
3.2.5 Plastic Flow	25
3.3 Finite Element Method/Analysis (FEM/FEA)	26
3.3.1 Finite Element Method	26
3.3.2 Abaqus implementation of FEM	27
4 Results	34
4.1 The 3D Finite Element Model	34
4.1.1 Initial assumptions	34
4.1.2 Model geometry	34
4.1.3 Discretization/meshing of geometry	37
4.1.4 Contact sliding	38
4.1.5 The Boundary conditions and applied load	41

Contents	VIII
4.1.6 Rheological parameters	42
4.2 Vertical Deformation	43
4.2.1 Model I: Reference model	45
4.2.2 Model II: Simultaneous slab pull and overriding velocities	47
4.2.3 Model III: Slab pull velocity only	49
4.2.4 Effect of the thickness of continental crust	51
4.2.5 Effect of varying continental drift velocity	52
4.2.6 Effect of oblique convergence	52
4.2.7 Effect of slab dip	53
5 Discussion and conclusion	55
Bibliography	68
Appendix	i
Acknowledgements	I
Selbstständigkeitserklärung	II

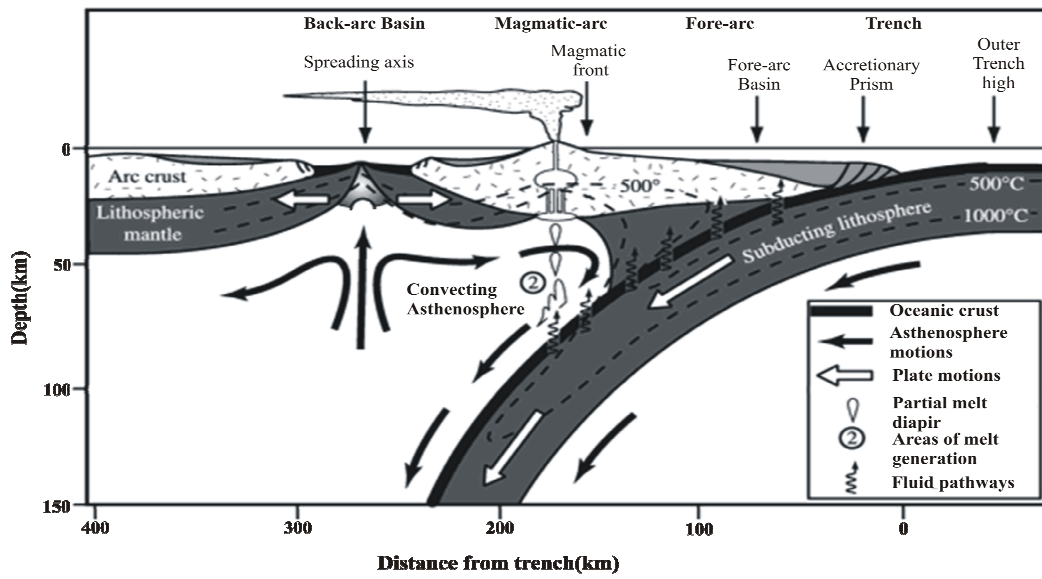
1 Introduction

The Earth and its processes always has been a subject of curiosity for the human race. The Earth processes such as movement of plates, generation of earthquakes, formation of volcanoes, and building of mountains attract the researchers for a long time. The Earth consists of mainly 3 layers: lithosphere, mantle, and core. There are two types of lithosphere: 1) the oceanic lithosphere, which is associated with oceanic crust and exists in the ocean basins and 2) the continental lithosphere, which is associated with continental crust.

In the theory of plate tectonics the lithosphere is divided into an interlocking network of blocks termed “plates”. These plates are considered to be internally rigid and their boundaries can be considered in three forms (Isacks et al., 1968). First are the oceanic ridges, which are characterized by diverging plates and also called as “constructive plate margins”. Secondly, the trenches are the boundaries where two plates are converging by the mechanism of the oceanic lithosphere of one of the plates being thrust under the other and absorbed into the sub-lithospheric mantle. They are also called as “destructive plate margins”; the third are the transform faults and are marked by tangential motions, in which adjacent plates in relative motion undergo neither destruction nor construction. The relative motion is usually parallel to the fault. They are also called as conservative plate margins (Kearey et al., 2008).

Subduction is the process that takes place at the convergent boundaries by which one tectonic plate moves under another tectonic plate and sinks into the mantle as the plates converge. Regions where this process occurs are known as subduction zones (Figure 1.1a). Subduction has a very important role in the recycling of the surface material by mixing it back to the deep Earth and introducing significant chemical variations back into the mantle (Christensen and Hofmann, 1994; Hofmann, 1997). Furthermore, it is also responsible for driving plate motions, mountain building, and the growth of new continental crust (Forsyth and Uyeda, 1975; Davidson and Arculus, 2006). In addition to playing the central role in the Earth tectonics, melt generation, and crustal surface (vertical and horizontal) deformations subduction zones profoundly impact on terrestrial life. Earthquakes and violent eruptions due to subduction zones cause widespread and unpredictable death and destruction.

a)



b)

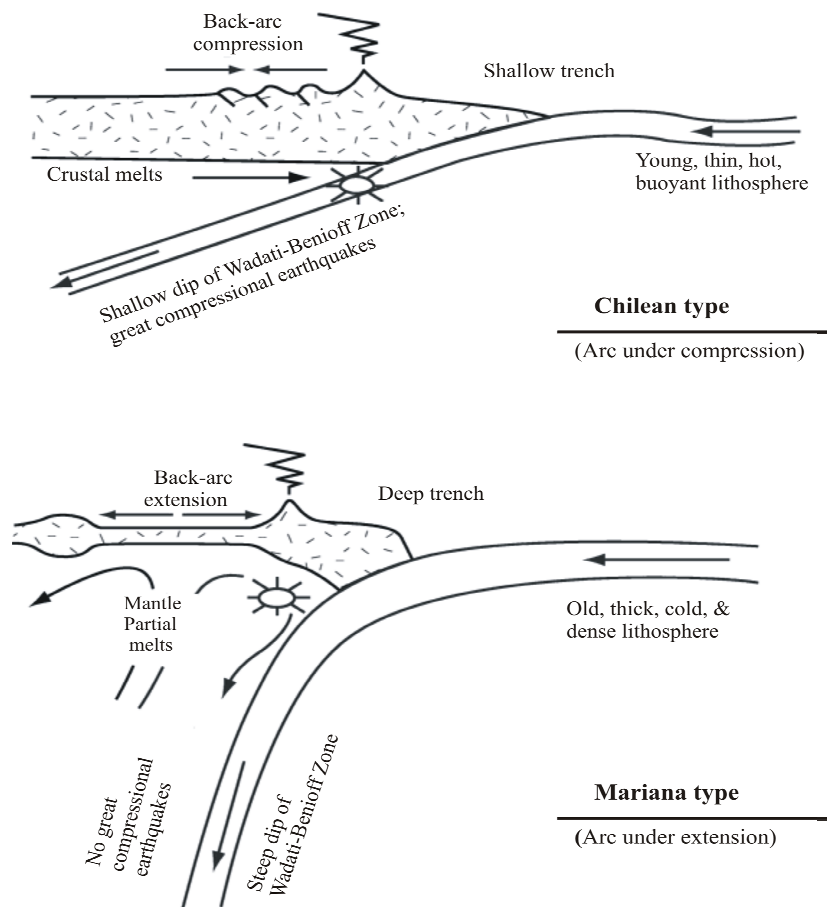


Figure 1.1. a) Structure of subduction zone (after Stern, 2002). b) Types of subduction zone based on the age of the underthrusting lithosphere and the absolute motion of the overriding plate (after Uyeda and Kanomari, 1979; Stern, 2002).

Subduction is a complex dynamic process, which occurs over long time scale and to large depths and integrates small scale with large scale phenomena. Uyeda and Kanamori (1979) propose two major types of the subduction, the Mariana and the Chilean types. These types are defined by an extensional and a compressive tectonic regime within the overriding plate, respectively (Figure 1.1b).

The subduction rate is measured in cm/yr, with the average rate of convergence being approximately 2 to 8 cm/yr (Defant, 1998). Some subduction zones extend from the Earth's surface down to the 660 km transition zone. When the functional cycle of the subduction zone is spectacularly disrupted due to continental crust, it may result in the building of mountain ranges such as the "Andes" and the "Himalayas" (Allmendinger et al., 1997; O'Brien, 2001). Some subduction zones are long-lived such as the Andean subduction zone, which is over 100 million years old whereas others have just initiated such as the New Hebrides and Puysegur subduction zones (Pacific ocean, near Vanuatu and south Tasman Sea).

The Andes are one of the largest active plate-boundary zones, forming a mountainous region which extends over 5000 km along the western margin of South America as a result of the subduction of the oceanic Nazca plate beneath the South American plate (Dewey and Bird, 1970; Pardo-Casas and Molnar, 1987) (Figure 1.2). The Andes show substantial variation in the tectonic style and evolution along their length, as well as several major changes in trend. Allmendinger et al. (1997) proposed that uplift of the Andes began ca. 25 Myr ago due to concomitant accelerated convergence between the Nazca and the South American plates. Early theories of formation of the Andes propose that it may be due to crustal growth by magmatic processes, but other studies of structural shortening estimation and symmetric paleomagnetically evaluations which defined rotation on the northern and southern flanks of the Altiplano imply that the uplift of the Andes result from non-uniform crustal shortening, with maximum shortening and consequent thickening at the centre of the Andean orocline (Isacks, 1988; Gregory-Wodzicki, 2000).

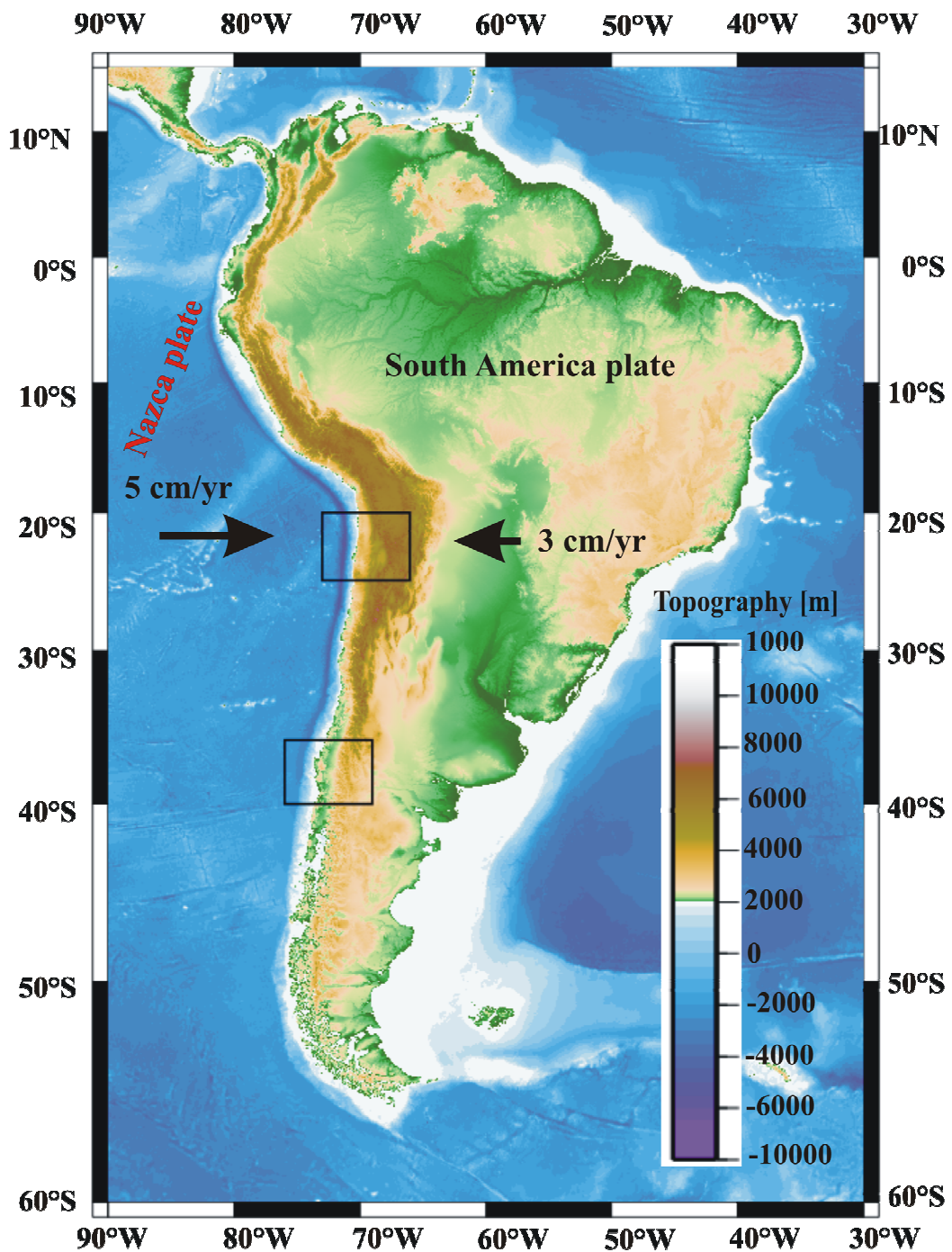


Figure 1.2. Map view of South American subduction zone. Black rectangles mark the investigation areas of this work, black arrows indicate the plate velocities (Somoza, 1998 and Silver et al., 1998).

Most researchers propose that crustal shortening due to the convergence between the subducting Nazca plate and the overriding South American plate is the major cause for the Andean uplift (Dewey and Bird, 1970; Isacks, 1988; Sheffels, 1990; Baby et al., 1992a; Dewey and Lamb, 1992; Allmendinger et al., 1997; Liu et al., 2002; Sobolev et al., 2006). The GPS (Global positioning system) data over the Central Andes also show 30-40 mm/yr crustal shortening across the Andes

(Leffler et al., 1997; Norabuena et al., 1998; Norabuena et al., 1999; Kendrick et al., 2001). The seismic data as well as the geological data also show crustal shortening concentrated in the sub-Andean thrust belt at a much lower rate (Suarez et al., 1983; Sheffels, 1990; Schmitz, 1994). Klotz et al. (2006) use Global positioning system and observed that the earthquake cycle dominates the contemporary surface deformation of the Central and Southern Andes.

Liu et al. (2002) showed the relationship between instantaneous crustal motion reflected by the GPS data and long-term crustal shortening in geological records using a simple viscoelastic-plastic model. They simulated the spatial distribution of the Andean crustal shortening in a 3D finite element model. They showed nearly uniform short-term velocity gradients across the Andes, consistent with the GPS data, and concentrated long-term crustal shortening in the sub-Andean thrust zone, consistent with the geological observations. Gravitational collapse in the high Andes is shown to be consistent with modern earthquake mechanisms, and the change of topographic loading along the Andes may explain the along-strike variation of extension directions indicated by seismic data. They explored the effects of the boundary conditions and basal shear in the model for possible causes of the reported changes in the orientation of crustal extension through the late Cenozoic.

Sobolev et al. (2006) examined the factors which control the intensity of the tectonic shortening by using the coupled thermo-mechanical numerical modelling technique and they inferred that the fast and accelerating westward drift of the South American plate as the most important factor. Further, they proposed that the crustal structure of the overriding plate and shear coupling at the plates interface are also important factors.

In addition, they also demonstrated an important role of the processes such as lithospheric delamination triggered by the gabbro-eclogite transformation in the thickened continental lower crust, and mechanical failure of the sediment cover at the shield margin which leads to mechanical weakening of the overriding plate during tectonic shortening.

Some authors also propose that there is a relationship between rising of a large mountain range and climate change. The mountains act as a barrier to the atmospheric circulation and affect the upper atmosphere flow patterns; which in turn affect the patterns of the precipitation and seasonal heating. It may lead to

climate change and thus, increases the rate of chemical weathering (Ruddiman and Kutzbach, 1989; Raymo and Ruddiman, 1992; Broccoli and Manabe, 1997; Lamb and Davis, 2003).

There is a causal link between the rise of a large mountain range and climate change. In Central South America, climate controlled sediment starvation might cause high shear stress which in turn supports the high Andes formation (Lamb and Davis, 2003). The marked global cooling trend observed since the Eocene might be due the mountain building (Raymo and Ruddiman, 1992).

The mechanism of the subduction process can only be understood by using a multidisciplinary integrative approach using geological observations, geophysical studies with chemical fingerprinting of materials recycled in the subduction system, and studies of subduction dynamics in space and time. Cattin et al. (1997) studied the effect of long term coupling in the subduction zones on fore-arc topography using a 2D finite element model. They assumed that the traction arising from the friction is one of the stresses acting on topography. Further, they proposed that the intrinsic coefficient of friction for the small rock samples may be high ($\mu \sim 0.6-0.8$); however the effective coefficient of friction less than 0.2 produces the consistent topography of the fore-arc region of Northern Chile.

In another study, Hassani et al. (1997) used a 2D finite element modelling approach to model the subduction of the oceanic lithospheric plate beneath the continental lithosphere. They showed that both the stress system in the plates and the surface topography are strongly dependent on the density contrast between lithosphere and asthenosphere ($\Delta\rho = \rho_L - \rho_A$) and the coefficient of friction along the subduction plane. Extension and back arc rifting corresponds to a positive density contrast and a low coefficient of friction, while negative $\Delta\rho$ values and/or high friction leads to a compressional regime. They also proposed that the coexistence of trench-arc compression and back-arc tension is only possible for a coefficient of friction lower than 0.1.

On the basis of paleotopography estimates from the upper crustal deformation, marine facies, geochemistry of volcanic rocks, climate from fossil floras, erosion rates, erosion surfaces, fission-track ages, and rates of terrigenous flux, Gregory-Wodzicki (2000) estimated the geological uplift rates and suggested the uplift rate for Central Andes up to 0.1 mm/yr in the early and middle Miocene, increasing to

0.2–0.3 mm/yr in the Miocene to present. Most of the uplift represents surface uplift as the Altiplano has experienced little erosion since the Miocene.

Variations such as surface plates velocities and buoyancy of the subducting lithosphere are likely to occur during the evolution of the subduction zone. Buiter et al. (2001) estimated the vertical surface displacements at the convergent plate margins resulting from such imposed variations. They developed the 2D numerical model in which the lithospheric plates have an effective elastic thickness as well as the subducting plate is driven by its negative buoyancy and a velocity at its surface side boundary. They found that a decrease in the buoyancy of the subducting material leads to a depression of the plate margins and increase in subducting material buoyancy leads to uplift of the plate margins. In addition, they showed that an increase in friction along the subduction fault deepens the overriding plate margin. They concluded that vertical surface displacements during ongoing subduction may reach a magnitude of a few kilometres on the overriding and subducting plate margins.

Commonly, the role of a trenchward moving continental plate for the growth of topography is neglected in both modelling and field studies. Instead, forces exerted by the down going plate on the continental plate as well as inter plate coupling are thought to be responsible for the deformation of the upper plate (Jordan et al., 1983; Bott et al., 1989; Dewey and Lamb, 1992; Shemenda, 1993; Willett et al., 1993; Gephart, 1994; Stern, 2002; Lamb and Davis, 2003). Hampel and Pfiffner (2006) presented 2D finite element models and analysed the role of the trenchward motion of the upper plate and inter plate coupling in the development of topography at the convergent margins. They demonstrated that trenchward motion of the continental plate plays a key role for the development of mountain belts at convergent margins.

The deformation patterns of the fore-arc wedges along the Chilean convergent margin vary significantly, despite having similar plate kinematic conditions (Hoffman-Rothe et al., 2006). Kellner (2007) carried out the analysis of the fore-arc deformation on two regions of the Chilean convergent margin at 20°S–24°S and 37°S–42°S. She examined the influence of different rheological approaches and varying physical properties of the fore-arc to identify and constrain the parameters controlling the difference in surface deformation between the two regions. She demonstrated that a small slab dip, a high coefficient of basal

friction, a high obliquity of convergence, and a high Young's modulus favour localisation of deformation in the fore-arc wedge.

In another study, Babeyko and Sobolev (2008) analysed stresses in the subducting plate using the high resolution 2D thermo-mechanical model with realistic viscoelastic-plastic rheology. They demonstrated that the unbending stress is the dominant stress at 50-100 km depth for the shallow dipping overridden slabs.

The Chilean Andes extend north-south for about 3000 km over the subducting Nazca plate, and show evidences of local rheological controls on first order tectonic features. Gerbault et al. (2009) tested rheological parameters of the subduction zone using numerical models with slab pull and upper plate convergence and calculate the development of stress and strain over a time period of 4 Myr. They studied the effects of subduction interface strength, arc and fore-arc crust rheology, and arc temperature on the development of superficial near surface faulting as well as viscous shear zones in the mantle. They showed that the deformation geometries are controlled by the intersection of the subduction interface with continental rheological heterogeneities. They also concluded that upper plate weakness and interface strength have an impact on the upper plate shortening and trench advance.

The absolute plate motions are considered to be a key factor for the upper plate behaviour, the slab geometry, and the trench migration (Jarrard, 1986; McCaffrey, 1994; Lallemand et al., 2005; Heuret et al., 2007). The subducting plate, overriding plate, and mantle have a combined effect on the active convergent margins shape. Van Dinther et al. (2010) developed a viscoelastic mechanical finite element model in which the subducting plate, overriding plate, and the mantle interact dynamically. When a slab interacted solely with the mantle flow, it showed that local non-induced mantle flow influences slab geometry and kinematics. Further, they showed that the trenchward moving overriding plate indents the slab and thereby enforces trench retreat and decreases the slab dip.

Bonnardot et al. (2008) developed a 3D mechanical numerical model and analysed the impact of the plate boundary geometry parameters (such as the inter-plate friction and the lithosphere–asthenosphere density contrast) on the deformation of the upper plate. They observed that oceanward convexity causes an accumulation of the subducted material beneath the upper plate and induces an important uplift of the convex area. On the contrary, the material escapes from an

oceanward concavity and provokes subsidence in the fore-arc zone. These processes induce preferential zones of weakness in the overriding plate and provide explanations for some local stress regime variations along convergent margins.

Gibert et al. (2012) studied the relationship between the subduction kinematics, overriding plate deformation, and the evolution of slab geometry using a 2D finite element numerical model. They observed two different styles of the subduction that depend on the overriding plate velocity v_{op} : If $v_{op} > 0$, the slab lies forward on the 660 km discontinuity (style 1), and if $v_{op} \leq 0$, the slab lies backward on the discontinuity (style 2).

Some authors also developed density models showing the mass distributions in the South American subduction zone (Strunk, 1990; Kirchner et al., 1996; Kösters, 1998; Tassara et al., 2006; Tašárová, 2007; Prezzi et al., 2009; Tassara and Echaurren, 2012).

Tassara et al. (2006) developed a density model (T06) by forward modelling the Bouguer gravity anomaly under the constraints of published geophysical data. This provides a continental-scale representation of the internal structure of the South American plate. Various researchers used this model for a number of quantitative approaches (Mamani et al., 2008; Pérez-Gussinyé et al., 2008; Melnick et al., 2009; Farías et al. 2010; Zeumann, 2013).

Further, Tassara and Echaurren (2012) presented an upgraded version of the 3D density model of the Nazca Slab and Andean margin with increased along-strike resolution of the model as compared to T06.

Recently, Zeumann (2013) also developed a 3D finite element model for the Andean subduction zone. She used the T06 density model as the structural basis for the dynamic modelling. She showed a subsidence rate of -5 to -9 mm/yr in the offshore fore-arc in the northern part but an uplift rate of 2 to 4 mm/yr for the southern fore-arc region. Further, she found that the whole model has compressional (negative values) east-west strain, except an area in the centre of the model within the fore-arc region. She observed highest compression in the Precordillera and Western Cordillera (arc region) and higher compressional strain in the southern part (-0.006) as compared to the northern part (-0.005). She assumed that it might be due to the trench geometry.

The direct relation between the subduction process and the devastating earthquakes and active volcanism emphasise a social need for a better understanding of the subduction process. Previous studies have augmented our understanding of the different aspects of the subduction processes and the combined mechanical links between the subducting plate, mantle flow, and the surface deformation. The subduction process plays a very important role in the geodynamical and geochemical phenomena that shape our Earth. However, past research has made it very clear that several fundamental questions still remain unanswered. The most important are embedded in the lack of a common behaviour of global subduction zones (Uyeda and Kanamori, 1979).

The Andean mountains are the consequence of the subduction of the oceanic Nazca plate. Despite of uniform convergence of the Nazca plate, the Andean orogen along its length displays a significant distinction in structure, volcanism, subducting slab geometry, deep lithospheric structure, and geological history (Jordan et al., 1983; Isacks, 1988; Cahill and Isacks, 1992; Yáñez and Cembrano, 2004; Tassara, 2005; Hoffmann-Rothe et al., 2006).

The Nazca-South America plate interface is considered to be highly coupled as compared to other subduction zones such as Marianas and it is highly prone to some of the largest earthquakes on Earth (Scholz and Campos, 1995; Conrad et al., 2004). It has been suggested that plate coupling, or the level of long term shear stress along the plate interface depends on several parameters such as subduction velocity, slab dip, and the amount of trench sediments (Jarrad, 1986; Kanamori, 1986; Ruff, 1989; Scholz, 1990; Scholz and Champos, 1995; Wang and Suyehiro, 1999; Lamb and Davis, 2003; Yáñez and Cembrano, 2004). There are also evidences of variation in along-strike plate coupling along the Andean margin (Yáñez and Cembrano, 2004; Hoffmann-Rothe et al., 2006).

The degree of the plate coupling gives a measure of interaction between the subducting and overriding plates and is still not well understood. Its determination assists in the identification of earthquake prone regions of the subduction zone. Therefore, it is necessary to identify and understand the plate coupling process for the mitigation of earthquake hazards.

The mechanical behaviour of the geometry as well as of the material can be studied by using continuum mechanics approach adapted in Finite Element Method (FEM). FEM simulation produces reliable results and has a strong

theoretical foundation. The commercial software Abaqus applies the finite element method approach and is also well accepted in geoscientific communities to model subduction related processes (Hetzl and Hampel, 2005; Hergert and Heidbach, 2006; Ellis et al., 2006; Gassmüller, 2011; Köther et al., 2012; Zeumann et al., 2013).

In the present work, the 3D finite element modelling is carried out for better understanding of the rheological parameters affecting the deformation of the overriding plate for the Andean subduction zone. Two regions having different subducting slab geometries are chosen. One area from the Northern Andes (20°S-25°S) with 18.4° as slab dip angle and a second area from the Southern Andes (36°S-40°S) with 13.4° as the slab dip angle. The physical parameters such as frictionally coupled plate movement, thickness of continental crust, and magnitude of the overriding velocity are considered for analysis. In addition, the behaviour of oblique subduction is also considered. To examine the effect of temperature on the overriding plate deformation, a thermo-mechanical model is also simulated.

This work is carried out within the project IMOSAGA (Integrated Modelling Of Satellite and Airborne Gravity data of Active plate margins), the extension of NOGAPSGRAV (NOvel Geophysical And Petrological applications of new-generation Satellite-derived GRAVity data with a focus on hazardous and frontier regions). These projects are one part of the priority program "Mass transport and mass distribution in the system Earth" (SPP1257) of the German Research Foundation (DFG) and are carried out in the cooperation with the university of Kiel and TU Munich.

2 The South American subduction zone

2.1 Tectonic setting

The Andes are tectonically segmented mountain range extending along the western margin of the South American plate. The geological characteristics of the Andean orogen vary significantly along and across the strike. Many studies relate these differences to the type and role of the subducting slab in particular along strike variations in slab dip, slab age, and convergence obliquity (Jordan et al., 1983; Lavenu and Cembrano, 1999; Gutscher et al., 2000; Stern, 2002; Lamb and Davis, 2003; Yáñez and Cembrano, 2004, Hoffmann-Rothe et al., 2006; Kellner, 2007). The wide-slab of the South American subduction zone implies the curved geometry of the trench and the mountain building (Schellart et al., 2007). The Nazca plate subducts at an angle of about 5° – 10° beneath the South American plate between 2° S– 15° S and 28° S– 33.5° S and forms “flat-slab” zones. The steeply dipping zones between 15° S to 28° S correspond to the areas of the young volcanism and are termed as “steep-slab” zones (Gregory-Wodzicki, 2000). There is also variation along the strike in the fore-arc wedge geometry and it depends on the slab dip angle (β) and the margin slope angle (α) (Hoffmann-Rothe et al., 2006).

It has been suggested that differences in the coupling zone strength from north to south are related to the sedimentary fill in the trench (Lamb and Davies, 2003). Further, Hoffmann-Rothe et al. (2006) found decrease in the effective coefficient of the inter-face friction by 16% towards the south. Bangs and Cande (1997) also suggested that the thickness of the sedimentary fill in the trench is more than 1.5 km and less than 0.5 km to the south and north of the Juan Fernandez Ridge, respectively.

Some studies propose that the cenozoic tectonic shortening of the South American plate over the subducting Nazca plate forms the second largest plateau on the Earth (Isacks, 1988; Allmendinger and Gubbels, 1996; Allmendinger et al., 1997; Lamb et al., 1997; Kley and Monaldi, 1998; Giese et al., 1999; Liu et al., 2002; Sobolev et al., 2006). The magnitude and the timing for the shortening vary significantly along the strike. The back-arc shortening in the Central Andes at 21° S started almost 50 Myr ago (Oncken et al., 2006). In contrast, the trench-normal compression in the Southern Andes accumulated less than 20 km of

crustal shortening and in the Early Pliocene shortening even stopped (Kley et al., 1999; Folguera et al., 2002). One of the possible reasons for decreasing the upper plate shortening in the Southern Andes is the reduction in the sedimentary fill in the trench towards the south (Dewey and Lamb, 1992; Klotz et al., 2001; Brooks et al., 2003). Sobolev et al. (2006) also suggested that the fast and accelerating westward drift of the South American plate is the most important factor for controlling the intensity of the South American plate shortening. Other studies propose that the degree of coupling of the overriding and the subducting plate or the relative motion of the trench and overriding plate is responsible for high topography of the Andes (Russo and Silver, 1996; Gutscher et al., 2000; Lamb and Davies, 2003; Hampel and Pfiffner, 2006; Oncken et al., 2006).

2.1.1 Northern/Central Andes

The Nazca plate subducts at a dip angle of 25° - 35° below the South American continental plate between the 18° S- 28° S and creates the Andean orogen (Barazangi and Isacks, 1976). The orogen between 18° S- 22° S is approximately 700 km wide and has a ca. 70-75 km thick crust (ANCORP Working Group, 1999, 2003). The orogen is further subdivided into three different structural units as the fore-arc, volcanic-arc, and the back-arc. Because of continuous subduction for the last 200 Myr, the fore-arc is further subdivided into distinct geological units with varying topography (Coastal Cordillera of 1000-3000 m elevation; longitudinal Central depression, and a Precordillera of elevation of 2000-4000 m). Then further to the east is the Western Cordillera having an active zone of stratovolcanoes with elevations of more than 6000 m. Adjacent to this, is the Altiplano, with 3700 m as an average topography. East of the Altiplano, is the Eastern Cordillera. Then further east of the Eastern Cordillera, are the Sub-Andean ranges dominated by an active fold-and-thrust belt with a width of 150-200 km and elevations of less than 500 m (Figure 2.1a) (Gerbault et al., 2009). The present active magmatic arc is located about 200 km away from the trench and above 100 km from the Wadati-Benioff zone (Cahill and Isacks, 1992; ANCORP Working Group, 1999).

The Atacama Fault Zone (AFZ, Figure 2.1b) more than 100 km long between the 20° S- 30° S is the excellent trench-parallel structure of the northern Chilean Coastal Cordillera and is formed in the Jurassic as a left-lateral, intra-arc fault (Scheuber and González, 1999; Gonzáles et al., 2003; Riquelme et al., 2003;

Cembrano et al., 2005). Since the Miocene, the AFZ has not been active as a major strike-slip system but, Dewey and Lamb (1992) estimated less than 1 mm/yr of dextral strike-slip since the Pliocene.

The Precordilleran Fault System (PFS, Figure 2.1b) is formed as an intra-arc trench parallel structure in the Paleogene magmatic arc migrating towards east since the late Eocene (Reutter et al., 1991). The PFS has been reactivated many times in the fore-arc with mainly sinistral strike-slip displacements (Reutter et al., 1996). Due to the Precordillera uplift in the Neogene, the PFS changed its displacement direction to the normal and dextral slip of the order of several hundred meters.

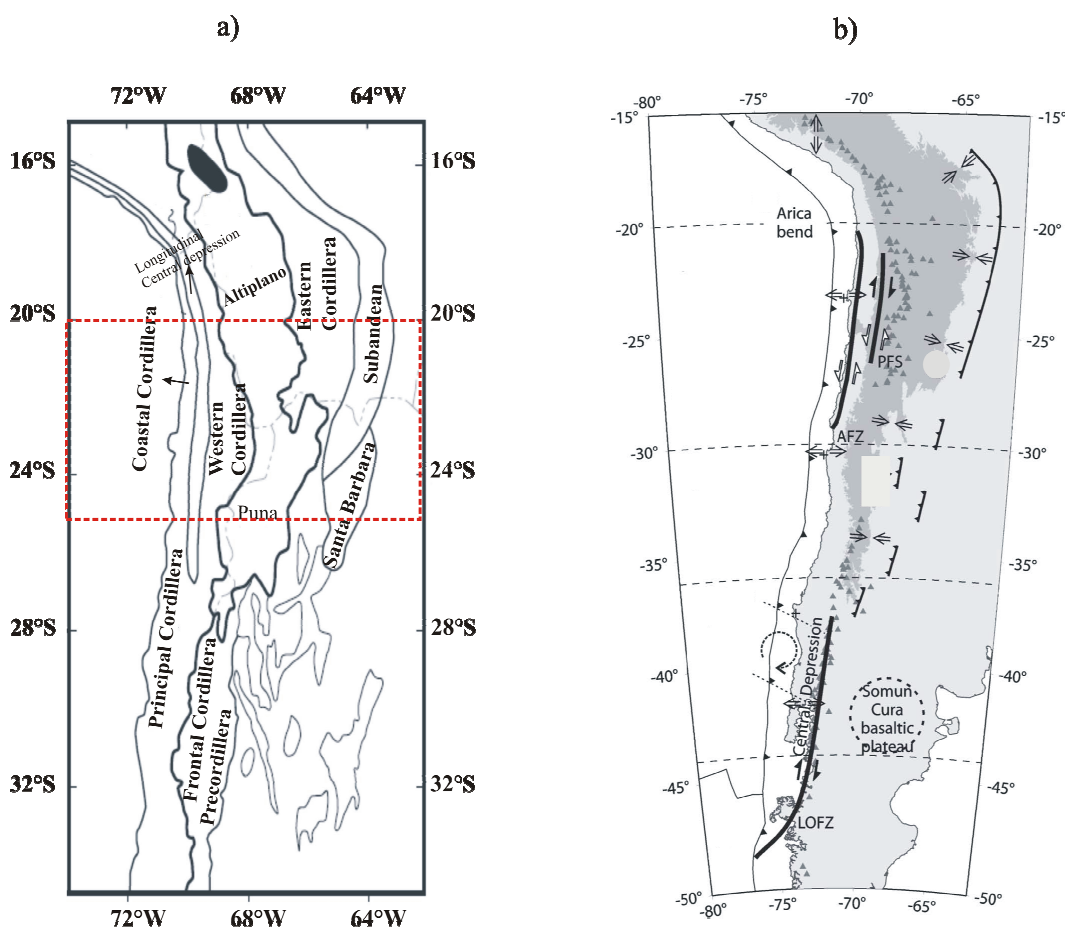


Figure 2.1. Geological map of South American subduction zone. a) Major geological units (after Gregory-Wodzicki, 2000). The red rectangle is the investigation area of this work. b) Major fault system of the South American plate (after Hoffmann-Rothe et al., 2006). Dark shading marks topography ≥ 2000 m elevation. Pairs of solid arrows denote the modern strike-slip fault direction, hollow arrows represents the past senses of slip. Triangles denote Holocene volcanoes. LOFZ: Liquiñe-Ofqui fault zone; AFZ: Atacama Fault Zone; PFS: Precordilleran Fault System.

From the 2D flexural analysis, Tassara (2005) showed that the fore-arc region has maximum rigidities between the 15°S-23°S and these decrease gradually towards the south and sharply towards the plateau. The main orogen (elevations higher than 3000 m) is very weak along the entire Central Andes.

Variation in the wind pattern along the strike controls the precipitation distribution along the Chilean margin (Campetella and Vera, 2002). The upper plate denudation is responsible for sediment thickness within the trench and it strongly depends on the precipitation.

2.1.2 Southern Andes

As compared to the Central Andean segment, the mean height of the southern Andes is less than 2000 m south of 33°S. The width of the orogen is ~300 km (E-W) and the crustal thickness below the magmatic arc is about 35-40 km (Bohm et al., 2002; Lüth et al., 2003).

The continental morphotectonics of the southern Andean segment is divided into three units (Cordillera, longitudinal depression, and main Cordillera). The fore-arc is composed of the Coastal platform, Coastal Cordillera and the Central Valley (longitudinal valley). The Coastal platform has shelf deposits of the late Cretaceous to Quaternary marine and minor continental deposits (Pineda, 1986). The Coastal Cordillera is a narrow belt with 10-100 km width. Its height varies from N-S with 1500 m at the Nahuelbuta (38°S) and few hundred meters at the Valdivia region (40°S-41°S). The Central Valley contains about 2 km of the Pliocene and Quaternary sediments, unconformably overlying the late Oligocene to Miocene volcano-sedimentary basin (Muñoz et al., 2000; Jordan et al., 2001). It extends from 36°S-39°S and from 40°S-42°S.

The Principal Cordillera coincides with the axis of the Jurassic magmatic arc and has occupied a relatively stationary position (Mpodosis and Ramos, 1989). The mean elevation of the Principal Cordillera is decreased from ~2700 m (36°) to ~1000 m (42°S). The subduction related voluminous magmatism is related to the Principal Cordillera from Jurassic to recent (López-Escobar, 1984; Hildreth and Moorbath, 1988; Lucassen et al., 2004; North Patagonian Batholith south of 40°S, Pankhurst et al., 1999).

The Liquiñe-Ofqui fault zone (LOFZ) as major geological fault is present between 37.5°S-47.5°S and runs parallel to the Southern Volcanic Arc. It is about 1100 km

long having maximum width of 100 m (Hervé, 1976; Cembrano et al., 1996, 2000; Vietor and Echter, 2006). It is a dextral intra-arc transforms fault and runs from the Liquiñe hot springs in the north to the Ofqui Isthmus in the south, where the Antarctic plate meets the Nazca plate and the South American plate at Chile Triple Junction.

2.2 Available data

2.2.1 Seismic velocity model

In 1996, a 400 km east-west seismic reflection profile named ANCORP (Andean Continental Research Project) was accomplished at 21°S as a combined reflection and refraction observations (Figure 2.2). It started at the Chilean coast, moves eastwards and terminates in Bolivia. The ANCORP profile and integrated geophysical experiments observe the subduction of the Nazca plate under the South American plate. The onshore reflection and wide-angle line continued previously acquired offshore reflection data from CINCA'95 project. Together these data result in a seismic transect from the Pacific Ocean to the Brazilian craton with a length of more than 800 km.

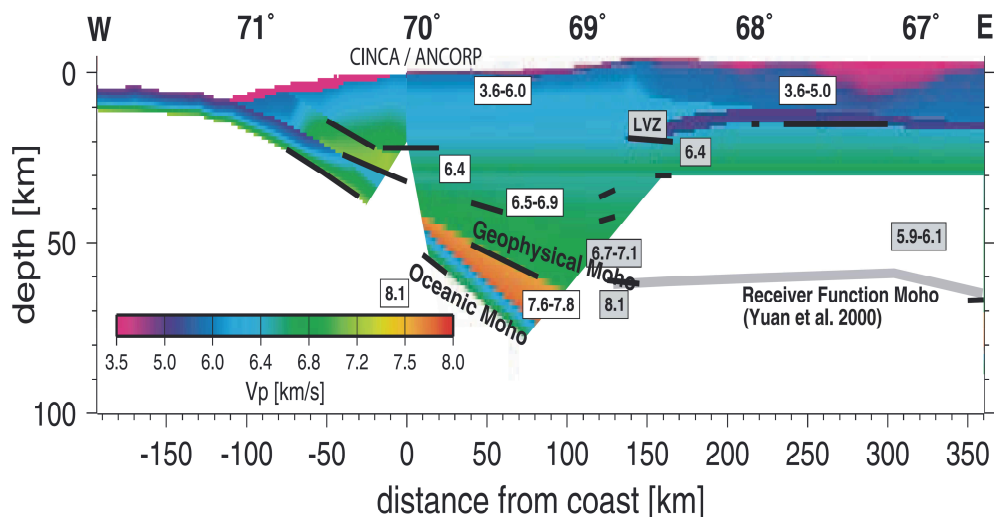


Figure 2.2. Velocity model along ANCORP transects (21°S) extended by offshore velocity observation of CINCA'95 experiments (ANCORP Working Group, 2003).

Figure 2.2 shows that v_p velocity of the fore-arc region (71°W–69°W) increases down to 50-55 km depth from 3.6 km/s to ~7 km/s.

The ISSA 2000 (Integrated Seismological experiment in the Southern Andes) experiments comprised of a seismic refraction profile along 39°S (Figure 2.3) that

recorded chemical shots fired in both the Pacific Ocean and in the Chilean Main Cordillera. ISSA 2000 wide angle data result in a 2D crustal velocity model having three main features.

- The uppermost 20 km of the crust show the lateral heterogeneity with average velocity of approximately 6.1 km/s in the fore-arc and approximately 6.4 km/s in the magmatic arc. Beneath the magmatic arc the upper crust is roughly 10 km thick and the lower crust is characterized by a high velocity of about 6.8 km/s at shallow depth. In contrast, the thickness of the upper crust in the fore-arc is 15 km and shows lower velocities of $v_p = 6.5$ -6.6 km/s at its base.
- The oceanic moho was observed by a seismic refraction profile at approximately 55 km depth beneath the Coastal Cordillera.
- Between the lower continental crust and the subducting oceanic crust a wedge shaped structure occurs beneath the fore-arc. The upper eastern part of this layer can be attributed to the continental mantle which is supposed to be deeper than 40 km under the arc. In the upper western part the P-wave velocity is considerably lower than that usually recorded for typical mantle.

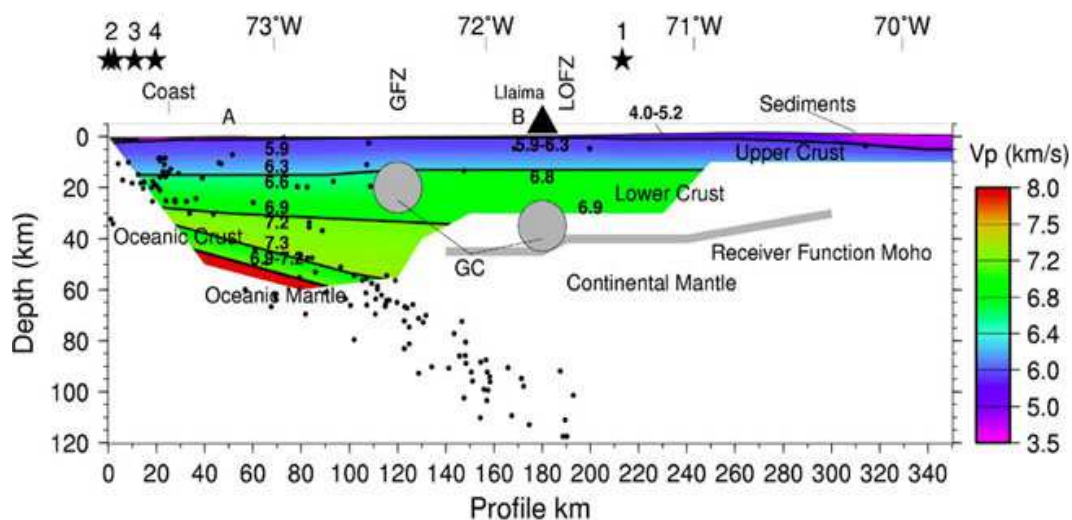


Figure 2.3. Velocity model at 39°S obtained by the ISSA 2000 experiment (Lüth et al., 2003). The gray circular patches indicate locations of good electrical (GC) conductors according to Brasse and Soyer (2001). Black dots indicate the earthquake hypocenters located from the ISSA 2000 passive seismological experiment (Bohm et al., 2002).

2.2.2 Uplift estimation

The work from Lamb and Hooke (1997) and Gregory-Wodzicki (2000) allow constraints to be placed on the timing and the rate of uplift in different morphotectonic provinces in the Central Andes (15°S-18°S). Gregory-Wodzicki (2000) used the estimation of crustal shortening and landscape development in the Western Cordillera, Altiplano, and Eastern Cordillera through the late Cenozoic and suggested that the subdomain of the Central Andes reached no more than half of its present height by 18–25 Myr ago. On the basis of paleoelevation estimates from the crustal shortening and the Chucal and Jakokkota floras, Gregory-Wodzicki (2000) suggested that the Altiplano reached about 25%–30% of its modern elevation in the early Miocene and had reached 50% by 10 Myr ago.

The paleobotanical evidences of central Andes imply a surface uplift of 2300–3400 m from Miocene to present. The estimation from Gregory-Wodzicki (2000) suggests uplift rates up to 0.1 mm/yr in the early and middle Miocene, increasing to 0.2–0.3 mm/yr in the Miocene to present (Table 2.1). Because the Altiplano has experienced little erosion since the Miocene, we can assume that most of the uplift represents surface uplift.

Table 2.1. Uplift estimation (after Gregory-Wodzicki 2000)

Area	Time period	Rate (mm/yr)
Altiplano	(19-25) to 60 Myr	0.02-0.03
Altiplano	11 to (19-25) Myr	0-0.1
Altiplano	Present to 11Myr	0.2-0.3
Eastern Cordillera, Central Andes	(14-21) to 10 Myr	0-0.4
Eastern Cordillera, Central Andes	Present to 10 Myr	0.2-0.3
Eastern Cordillera, Northern Andes	(4-5) to (11-16) Myr	0.03-0.05
Eastern Cordillera, Northern Andes	2.7 ± 0.6 to (4-5) Myr	0.6-3.0
Eastern Cordillera, Northern Andes	Present to 2.7 ± 0.6 Myr	0

3 Basic Theories

3.1 Continuum mechanics and Rheology

Rheology is a branch of Physics which includes the study of flow of materials. The rheological behaviour such as elastic, plastic, and viscoelastic are present in the nature. The nature of deformation depends on the material rheology and the stresses applied on it. A material is considered as fluid independently of its atomic structure when it flows under constant stresses. Its fluidity depends on external conditions e.g. temperature, pressure, and duration of loading (Ranalli, 1995). Understanding of rheology plays an important role for studying the deformation and flow related to geophysical and geodynamical processes. Undoubtedly, the mechanical and thermal processes included in these Earth processes can not be resolved without recognition to rheology.

There are two major approaches for studying rheology. First is the continuum-mechanics (macroscopic) and second is the discrete-mechanics (microscopic). Continuum mechanics deals with the analysis of the kinematics and mechanical behaviour of materials modelled as a continuous body. Continuum mechanics describes the properties of the materials without formal reference to the atomic processes, which governs the behaviour (Ranalli, 1995). The description of Earth materials like rocks as a continuum allows us to investigate many aspect of their rheology. So continuum mechanics approach is an essential tool and can lift us to the long way in the study of geophysical and geodynamic processes.

Stress tensor

Stress is the intensity of internal forces acting between particles of a body across imaginary internal surfaces.

The state of stress at a point is defined as totality of all stress vectors $\overset{n}{T}$ at that point and gives this relation as shown in equation 3.1a (Chen and Han, 2007)

$$\lim_{\Delta A \rightarrow 0} \frac{F_n}{\Delta A} = T = \overset{n}{T} \quad (n = 1, 2, 3 \text{ for 3D}) \quad (3.1a)$$

where ΔA is the surface area passing through a point with a unit vector \mathbf{n} normal to the area ΔA and F_n is the resultant force due to the action across the area ΔA of the material. The nine quantities required to define the three stress vectors ($\overset{1}{T}$,

T^2, T^3) called the components of stress tensor and can be represented by 3×3 matrix form as in equation 3.1b

$$\sigma_{ij} = \begin{bmatrix} T^1 \\ T^2 \\ T^3 \\ T^3 \\ T^1 \end{bmatrix} = \begin{bmatrix} \sigma_{11} & \sigma_{12} & \sigma_{13} \\ \sigma_{21} & \sigma_{22} & \sigma_{23} \\ \sigma_{31} & \sigma_{32} & \sigma_{33} \end{bmatrix} \quad (3.1b)$$

where $\sigma_{11}, \sigma_{22}, \sigma_{33}$ are the normal components of stress, $\sigma_{12}, \sigma_{13}, \sigma_{23}$ are shear components of the stress. In general the stress vector T^i is associated with coordinate plane X_1, X_2, X_3 and can be written as in equation 3.1c

$$T^i = \sigma_{ij} e_j \quad (i, j = 1, 2, 3) \quad (3.1c)$$

where σ_{ij} is the j -th component of stress vector T^i acting on an area element (at point) whose normal is in the direction of the positive X_i -axis. Because the stress tensor is symmetric, so the components of the stress vector acting on an arbitrary plane \mathbf{n} at a given point in terms of the component of stress tensor σ_{ij} at that point can be written as in equation 3.1d

$$T_i^n = \sigma_{ji} n_j \quad (n, i, j = 1, 2, 3) \quad (3.1d)$$

Equations of equilibrium

A three-dimensional continuum shows balance of stresses with the following system of equations 3.2a-c (Ranalli, 1995)

$$\frac{\partial \sigma_{11}}{\partial x_1} + \frac{\partial \sigma_{21}}{\partial x_2} + \frac{\partial \sigma_{31}}{\partial x_3} + \rho X_1 = 0 \quad (3.2a)$$

$$\frac{\partial \sigma_{12}}{\partial x_1} + \frac{\partial \sigma_{22}}{\partial x_2} + \frac{\partial \sigma_{32}}{\partial x_3} + \rho X_2 = 0 \quad (3.2b)$$

$$\frac{\partial \sigma_{13}}{\partial x_1} + \frac{\partial \sigma_{23}}{\partial x_2} + \frac{\partial \sigma_{33}}{\partial x_3} + \rho X_3 = 0 \quad (3.2c)$$

where ρ denotes the density of the material. After applying gravity (g) load in the vertical direction pointing upwards, the components of body force become $X_1 = X_2 = 0, X_3 = -g$, then equation (3.2c) changes to equation (3.2d).

$$\frac{\partial \sigma_{13}}{\partial x_1} + \frac{\partial \sigma_{23}}{\partial x_2} + \frac{\partial \sigma_{33}}{\partial x_3} = \rho g \quad (3.2d)$$

This system of differential equations describes the response of a continuum due to applied boundary conditions and can be solved numerically.

3.2 Rheological classes

The rheological behaviour of the materials depends on the level of applied stresses. Materials can be divided into different rheological classes based on their nature of deformational response with respect to the stresses.

3.2.1 Elastic rheology

The crystalline materials (like rocks) at low pressure and temperature show elastic behaviour. Elasticity has wide application in the geodynamics. The upper lithosphere can be considered as elastic for loads of duration of the order of hundred to millions of years. Furthermore, the whole Earth behaves elastically with imperfections for loads of short duration (Ranalli, 1995). The behaviour of elastic material is shown in Figure 3.1a. The rheological properties of elasticity have the following characteristics:

- Instantaneous deformation upon application of load.
- Instantaneous and total recovery upon removal of load.
- Linear proportionality between stress and strain.

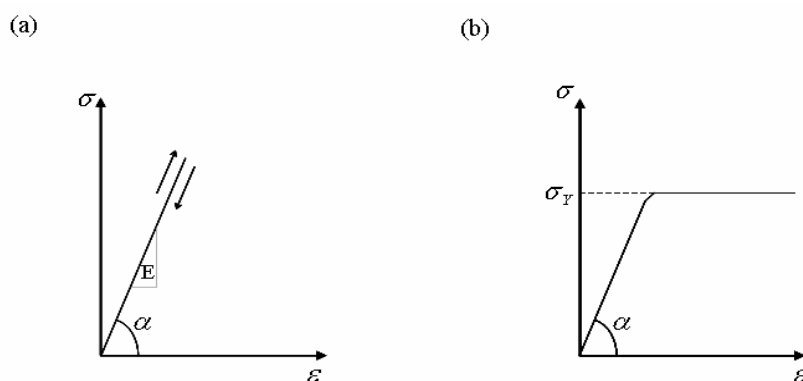


Figure 3.1. The rheological response of an elastic and a plastic body: (a) Linear correlation between the stress (σ) and strain (ϵ) in an elastic body. Arrows denotes the loading/unloading path. (b) Relation between stress (σ) and strain (ϵ) in a plastic body. Material behaves elastically below the yield stress (σ_y) and then deform in a ductile manner having constant stress with increasing strain. α = friction angle (after Kellner, 2007).

The theoretical models for perfect elasticity follow the generalized Hooke's law, which assumes that the components of stress at any point within the elastic medium are homogeneous linear functions of components of strain and can be written in the form of equation 3.3 (Ranalli, 1995)

$$\sigma_{ij} = C_{ijkl} \varepsilon_{kl} \quad (i,j,k,l = 1,2,3) \quad (3.3)$$

where C_{ijkl} represents elastic parameters. Since σ_{ij} and ε_{kl} are symmetric tensors therefore, have only six components. Thus maximum 36 elastic parameters are independent. For isotropic materials, in which elastic behaviour does not depend on direction and these parameters reduce to 2. So Hooke's law takes the form of equation 3.4

$$\sigma_{ij} = \lambda \varepsilon_{kk} \delta_{ij} + 2\mu \varepsilon_{ij} \quad (3.4)$$

where δ_{ij} is the Kronecker delta, λ and μ and are two elastic parameters termed as Lamé's constants. Young's modulus (E) and Poisson's ratio (ν) can be calculated with the equation 3.5

$$E = \frac{\mu(3\lambda + 2\mu)}{\lambda + \mu} \quad \nu = \frac{\lambda}{2(\lambda + \mu)} \quad (3.5)$$

3.2.2 Plastic rheology

The plastic material behaviour is shown in Figure 3.1b. Materials with plastic rheology have the following characteristics:

- The linear elastic behaviour applies only below critical stress (elastic limit) of the material.
- Above the elastic limit deformation is at first non-linear and when the deviatoric stress reaches a value σ_Y termed the yield stress, the material fails.
- Failure can result either in discontinuous deformation (fracture) when material shows loss of stability along an approximately well defined structure surface, or in irrecoverable continuous deformation (plastic flow) when the material yields without any apparent loss of continuity.

3.2.3 General yield criteria

The yield criterion defines the elastic limits of a material under combined states of stress. In general the elastic limit or yield stress is a function of the state of stress σ_{ij} and, the yield condition can generally be expressed as in equation 3.6 (Chen and Han, 2007)

$$f(\sigma_{ij}, K_1, K_2, \dots) = 0 \quad (3.6)$$

where K_1, K_2, \dots are material constants, which are determined experimentally. Since the stress state at a point is characterised by the principal stresses. So the general yield condition (equation 3.6) becomes equation 3.7

$$f(\sigma_1, \sigma_2, \sigma_3, K_1, K_2, \dots) = 0 \quad (3.7)$$

For hydrostatic pressure dependent material such as rocks yielding conditions equation 3.7 changes to equation 3.8

$$f(I_1, J_2, J_3, K_1, K_2, \dots) = 0 \quad (3.8)$$

where I_1, J_2, J_3 are the first, second and third stress invariant, respectively.

3.2.4 Mohr-Coulomb criterion

The Mohr criterion is based on the assumption that the maximum shear stress is the only decisive measure of the impending failure. This criterion considers the limiting shear stress τ in a plane to be a function of the normal stress σ in the same plane at a point and can be written as in equation 3.9

$$|\tau| = f(\sigma) \quad (3.9)$$

where $f(\sigma)$ is the experimentally determined yield function. Figure 3.2 shows the graphical representation of the Mohr-Coulomb criterion. Equation 3.9 means that failure of material occurs if the radius of the largest principal circle is tangent to the envelop curve $f(\sigma)$. The Mohr criterion allows declining the effect of mean stress or the hydrostatic stress. The simplest form of Mohr's envelop $f(\sigma)$ is a straight line, as illustrated in Figure 3.2. The equation for the straight line envelop is known as Coulomb's equation and it is represented as in equation 3.10

$$|\tau| = c - \sigma \tan \phi \quad (3.10)$$

In equation 3.10, c is the cohesion and ϕ is the angle of internal friction; both are the material constants. τ and σ are the shear and normal stress, respectively, acting on the plane where failure occurs. According to this criterion the larger the pressure $-\sigma$, the higher is the shear that material can sustain. In Figure 3.2, the large Mohr circle with its centre $\left(\frac{1}{2}(\sigma_1 + \sigma_3), 0\right)$ and radius $\frac{1}{2}(\sigma_1 - \sigma_3)$ gives equation 3.11

$$\tau = \frac{\sigma_1 - \sigma_3}{2} \cos \phi \quad \text{and} \quad \sigma = \frac{\sigma_1 + \sigma_3}{2} + \frac{\sigma_1 - \sigma_3}{2} \sin \phi \quad (3.11)$$

Using equation 3.11 in equation 3.10, the Mohr-Coulomb criterion (equation 3.10) changes to equation 3.12 (Chen and Han, 2007)

$$\frac{1}{2}(\sigma_1 - \sigma_3) \cos \phi = c - \left[\frac{1}{2}(\sigma_1 + \sigma_3) + \frac{\sigma_1 - \sigma_3}{2} \sin \phi \right] \tan \phi$$

$$\text{for } \sigma_1 \geq \sigma_2 \geq \sigma_3 \quad (3.12)$$

Rearranging terms of equation 3.12 gives equation 3.13

$$\sigma_1 \frac{1 + \sin \phi}{2c \cos \phi} - \sigma_3 \frac{1 - \sin \phi}{2c \cos \phi} = 1 \quad (3.13)$$

The strength of a Mohr-Coulomb material in the uniaxial compression and uniaxial tension, respectively be given as in equation 3.14

$$f'_c = \frac{2c \cos \phi}{1 - \sin \phi} \quad \text{and} \quad f'_t = \frac{2c \cos \phi}{1 + \sin \phi} \quad (3.14)$$

Then the Mohr-Coulomb criterion reduces to equation 3.15

$$\frac{\sigma_1}{f'_t} - \frac{\sigma_3}{f'_c} = 1 \quad \text{for} \quad \sigma_1 \geq \sigma_2 \geq \sigma_3 \quad (3.15)$$

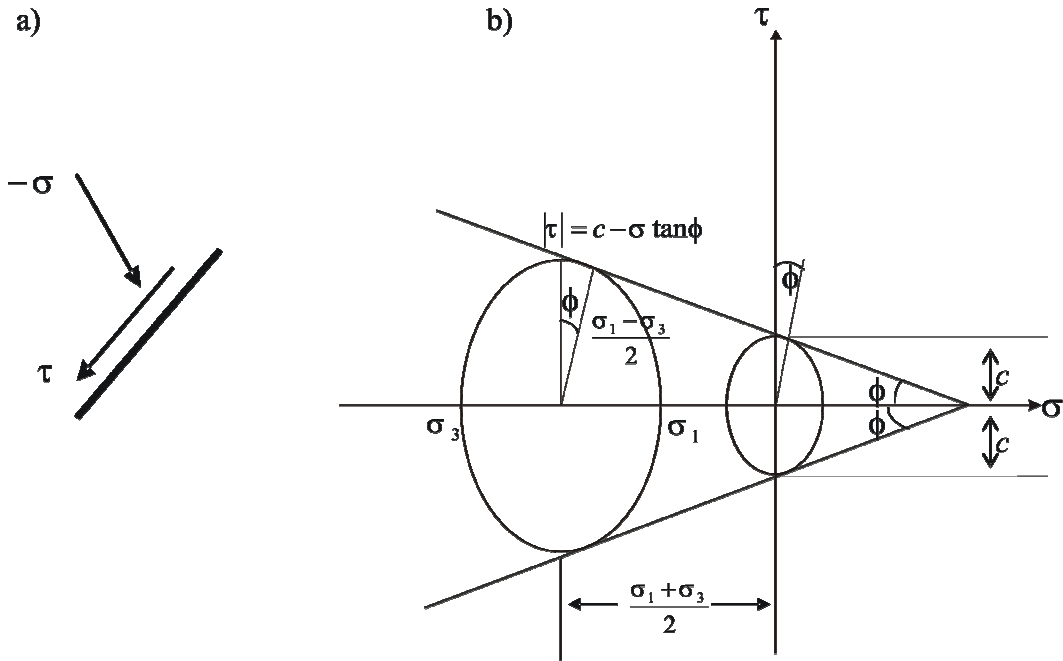


Figure 3.2. Mohr-Coulomb criterion: (a) The Coulomb friction over a plane with shear and normal stress τ and $-\sigma$, respectively (after Piaras Kelly, 2012). (b) Mohr-Coulomb failure criterion: with straight line as a failure envelope (after Chen and Han, 2007).

3.2.5 Plastic Flow

If plastic material satisfies equation 3.6, then it flows plastically and satisfies the following equation 3.16

$$d\varepsilon_{ij}^p = d\lambda \frac{\partial g}{\partial \sigma_{ij}} \quad (3.16)$$

where g is the plastic potential function and $d\lambda$ is a positive scalar factor of proportionality, which is non zero only when plastic deformation occurs. For the special case when the yield function coincides with the plastic potential function, $f = g$, then equation 3.16 becomes equation 3.17

$$d\varepsilon_{ij}^p = d\lambda \frac{f}{\partial \sigma_{ij}} \quad (3.17)$$

equation 3.17 is called “associated flow rule” because plastic flow is associated with yield criterion. While the associated plasticity can be applied successfully on the metals, whereas it is less applicable to the Earth materials such as rocks. For Earth materials the most appropriate form of plasticity is non-associated plasticity, in which the yield function is not associated with the plastic potential function and satisfies the condition $f \neq g$.

3.3 Finite Element Method/Analysis (FEM/FEA)

The finite element method (FEM) is a numerical technique based on discretization of a continuous space for finding approximate solutions of Partial Differential Equations (PDE) and their systems. Initial hypothetical assumptions are made, resulting in an approximation of realistic problems. The FEM analysis needs approximations of the geometry as compared to the analytical method. The accuracy of a FEM solution depends on the assumptions chosen in the geometry design, physical laws, boundary conditions, and load required to define the state of the elements. The flexibility of FEM permits a field simulation including precise geometries, isotropic or anisotropic material with any material laws, heterogeneous rheological layering, time-dependent solutions, contact, and Coulomb friction criteria between different units of geometry. Furthermore, the FEM has also a solid theoretical foundation which makes this method more reliable and in many cases makes it possible to mathematically analyse and estimate the error in the approximate finite element solution. Thus, FEM is an appropriate tool for modelling the realistic Earth deformation processes.

The Finite Element Analysis (FEA) was first developed in 1943 by R. Courant (http://www.sv.vt.edu/classes/MSE2094_NoteBook/97ClassProj/num/widas/history.html). FEA consists of a material model in which specific conditions were applied and their effects were analysed. There are two common ways of FEA: 2D analysis, and 3D analysis. 2D analysis conserves simplicity and allows the analysis to be run on any computer but it tends to yield less accurate results as compared to real situations. However in 3D analysis, the process is complex and produces more realistic results but it requires a specific computing system. In this study, analysis of surface deformation associated with the South American subduction zone was performed with a commercial finite element system 'Abaqus' (Abaqus Analysis User's Manual, 2010).

3.3.1 Finite Element Method

Pre-processing

A finite element analysis on a software system requires the following information for pre-processing:

- Locations of nodes on geometry.
- Elements and their type for connecting nodes.

- Properties of material used for analysis.
- Elements and nodes sets for applying initial conditions, boundary conditions, and load.
- Contact Formulation.
- Type of analysis.

Solution process

- After pre-processing, the finite element solution is processed by solving a set of simultaneous algebraic equations 3.18

$$[\mathbf{K}] \{\mathbf{u}\} = \{\mathbf{F}\} \quad (3.18)$$

where u is the displacement vector, $u = [u_1, u_2, \dots, u_n]$, F is the loading vector, $F = [F_1, F_2, \dots, F_n]$ and K is $n \times n$ matrix called stiffness matrix. The force is usually known, displacement is unknown and stiffness describes the characteristic properties of the elements. The order of the stiffness matrix is the same as the total number of directions in which motion is possible.

- Parameters such as strain and stress at the elements are calculated by solving the system of equations (equation 3.18) having unknown quantities at the nodes (e.g., displacements).

3.3.2 Abaqus implementation of FEM

Abaqus is appropriate software for finite element analysis (Abaqus Analysis User's Manual, 2010). Abaqus is designed to solve problems ranging from relatively simple linear analyses to the most challenging nonlinear simulations. Abaqus consists of three main analysis products: Abaqus/Standard, Abaqus/Explicit, and Abaqus/CFD. In this project, Abaqus/Standard is used for modelling and analysis of surface deformation associated with the South American subduction zone. Abaqus/Standard is a general-purpose analysis product that helps to solve a wide range of linear and nonlinear problems involving the static and quasi-static mechanical problems. Abaqus /CAE or Complete Abaqus Environment is used for both modelling and analysis of mechanical components and assemblies and to visualizing the FEA results. Abaqus contains an extensive library of elements having both linear and quadratic

geometric order, which can model virtually any geometry. The Abaqus material library provides a comprehensive coverage of linear and nonlinear as well as isotropic and anisotropic material properties. Abaqus provides linear elasticity, viscoelasticity, Drucker-Prager plasticity, and Mohr-Coulomb plasticity to the materials. It is possible to apply associated and non-associated plasticity. Abaqus/Standard provides a variety of methods to specify initial conditions (e.g. initial stress field due to gravity), boundary conditions (e.g. displacements, velocities), loads (e.g. gravity, pressure), and predefined fields for various analysis types. A complete Abaqus analysis usually consists of three distinct stages: pre-processing, simulation, and post-processing as shown in Figure 3.3. These three stages are linked together by files.

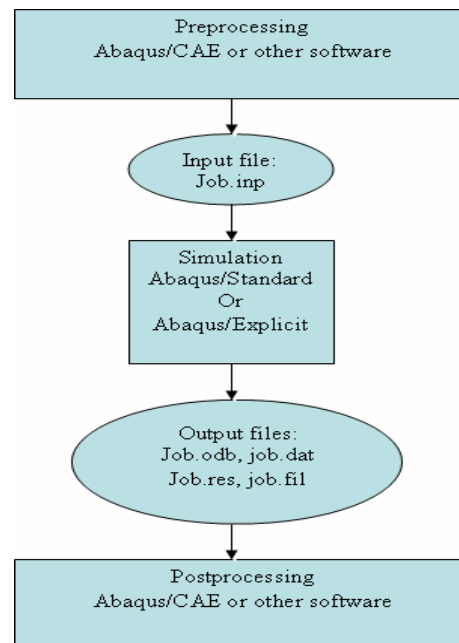


Figure 3.3. Flow chart showing the different stages of complete Abaqus analysis and all the three stages are linked to one another by files (after Abaqus Analysis User's Manual, 2010).

The availability of a wide range of rheologies and the ability to handle the three dimensional complexities makes Abaqus popular among the geoscientific community (Hetzl and Hampel, 2005; Hergert and Heidbach, 2006; Ellis et al., 2006; Gassmüller, 2011; Köther et al., 2012; Zeumann et al., 2013).

Contact formulation

The contact between two bodies can be defined in Abaqus by using the contact pairs approach. In the present work, the surface based contact pairs approach was

applied. Every contact pair is assigned a contact formulation with interaction property. In Abaqus/Standard when a contact pair has two surfaces; they are not allowed to include the identical nodes. Abaqus applies master-slave definition on the surface-based contact pairs and in this the master surface can penetrate the slave surface but reverse is not allowed. The selection of slave and master surfaces is the choice of the user. To avoid solution convergence problems, it is suggested to choose the finer meshed surface as a slave surface and the coarse meshed surface as a master surface (Abaqus Analysis User's Manual, 2010).

Coulomb friction model

The interaction between contact pairs is assigned by defining a contact property model to the contacting pairs. In this project, the Coulomb friction model was selected to create friction between the frictionally coupled part of the model, and the rest of the contact pairs have frictionless contact properties. The Coulomb friction model relates the maximum allowable frictional (shear) stress across the interface to the contact pressure between the contacting bodies by defining the value of friction coefficient at the interface. In the Coulomb friction model, two contacting surfaces can carry shear stresses up to a certain magnitude across their interface before they start sliding relative to one another; this state is known as 'sticking'. The Coulomb friction model defines this critical shear stress (τ_{crit}) at which sliding of the surfaces starts as a fraction of the contact pressure (p) between the surfaces as in equation 3.19 (Abaqus Analysis User's Manual, 2010)

$$\tau_{crit} = \mu p \quad (3.19)$$

where μ denotes the friction coefficient. The stick/slip calculations determine when a point passes from sticking to slipping or from slipping to sticking. For a three dimensional simulation, there are two orthogonal components of shear stress, τ_1 and τ_2 , along the interface between the two bodies. These components act in the slip directions of the contact surfaces. Abaqus combines the two shear stress components into an "equivalent shear stress ($\bar{\tau}$)" for the stick/slip calculations, where $\bar{\tau} = \sqrt{\tau_1^2 + \tau_2^2}$. The stick/slip calculations define a surface shown in Figure 3.4 (for a two-dimensional representation) in the contact pressure–shear stress space along which a point passes from sticking to slipping.

In the 3D case, sliding of the surface starts when the shear stress reaches the equivalent shear stress ($\bar{\tau}$) value.

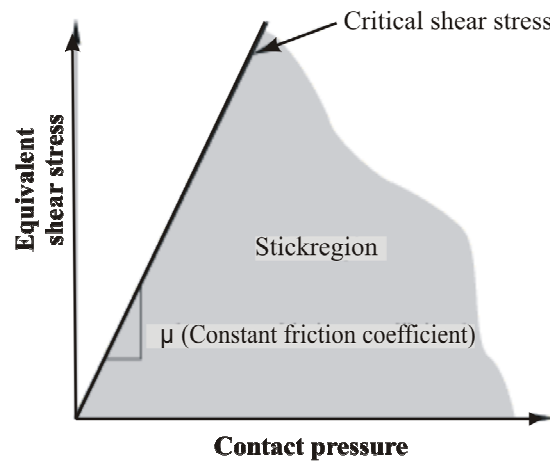


Figure 3.4. Stick/slip regions for the basic Coulomb friction model in the contact pressure-equivalent shear stress space; the shaded region denotes the sticking region where no slip occurs (Abaqus Analysis User's Manual, 2010).

The Mohr-Coulomb yield criterion

The Mohr-Coulomb criterion assumes that yield occurs when the shear stress on any point in a material reaches a value that depends linearly on the normal stress in the same plane. The Mohr-Coulomb model is based on plotting Mohr's circle for states of stress at yield in the plane of the maximum and minimum principal stresses. The yield line is the line that touches these Mohr's circles as represent in Figure 3.5 (Abaqus Analysis User's manual, 2010).

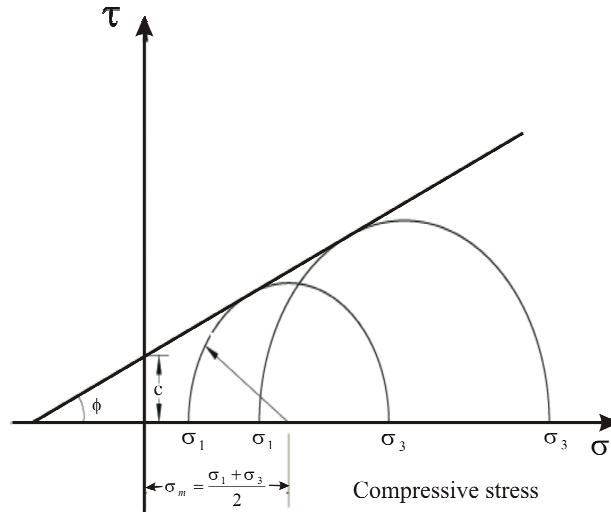


Figure 3.5. The Mohr-Coulomb yield model for Abaqus: c is the material cohesion; ϕ is the friction angle (Abaqus Analysis User's manual, 2010).

The Mohr-Coulomb model is defined by equation 3.20

$$\tau = c - \sigma \tan \phi \quad (3.20)$$

where σ is negative in compression and positive for extension. The Mohr's circle gives equations 3.21 and 3.22

$$\tau = s \cos \phi \quad (3.21)$$

$$\sigma = \sigma_m + \sin \phi \quad (3.22)$$

Substituting for τ and σ , multiplying both sides by $\cos \phi$, and reducing, the Mohr-Coulomb model can be written as equation 3.23

$$s + \sigma_m \sin \phi - \cos \phi = 0 \quad (3.23)$$

where $s = \frac{1}{2}(\sigma_1 - \sigma_3)$, is half of the difference between the maximum principal stress (σ_1) and the minimum principal stress (σ_3) and is therefore, the maximum shear stress

$$\sigma_m = \frac{1}{2}(\sigma_1 + \sigma_3) \quad (3.24)$$

Equation 3.24, is the average of the maximum and minimum principal stresses, and ϕ is the friction angle. For general states of stress the model is more conveniently written in terms of three stress invariants as in equation 3.25 (Abaqus Analysis User's Manual, 2010)

$$F = R_{mc} q - p \tan \phi - c = 0 \quad (3.25)$$

where

$$R_{mc}(\Theta, \phi) = \frac{1}{\sqrt{3} \cos \phi} \sin \left(\Theta + \frac{\pi}{3} \right) + \frac{1}{3} \cos \left(\Theta + \frac{\pi}{3} \right) \tan \phi$$

ϕ is the slope of the Mohr-Coulomb yield surface in the p - $R_{mc}q$ stress plane in Figure 3.6a, which is commonly referred to as the friction angle of the material.

c is the cohesion of the material; and Θ is the deviatoric polar angle defined as

$$\cos(3\Theta) = \left(\frac{r}{q} \right)^3 \quad (3.25a)$$

and

$$p = -\frac{1}{3} \text{trace}(\boldsymbol{\sigma}) \quad \text{is the equivalent pressure stress} \quad (3.25b)$$

where

$$\text{trace}(\boldsymbol{\sigma}) = \sigma_1 + \sigma_2 + \sigma_3$$

$$q = \sqrt{\frac{3}{2} (\mathbf{S} : \mathbf{S})} \quad \text{is the Mises equivalent stress} \quad (3.25c)$$

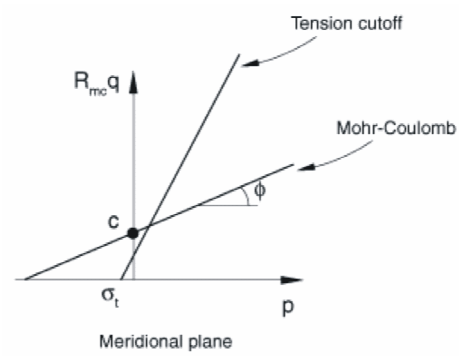
$$r = \left(\frac{9}{2} \mathbf{S} \cdot \mathbf{S} : \mathbf{S} \right)^{\frac{1}{3}} \quad \text{is the third invariant of deviatoric stress} \quad (3.25d)$$

and

$$\mathbf{S} = \boldsymbol{\sigma} + p\mathbf{I} \quad \text{is the deviatoric stress} \quad (3.25e)$$

where $\boldsymbol{\sigma}$ and \mathbf{I} are the stress and identity tensor, respectively. The friction angle ϕ controls the shape of the yield surface in the deviatoric plane as shown in Figure 3.6b. The friction angle range is $0^\circ \leq \phi < 90^\circ$. In the case of $\phi = 0^\circ$ the Mohr-Coulomb model reduces to the pressure-independent Tresca model with a perfectly hexagonal deviatoric section. In the case of $\phi = 90^\circ$ the Mohr-Coulomb model reduces to the “tension cut-off” Rankine model with a triangular deviatoric section.

a)



b)

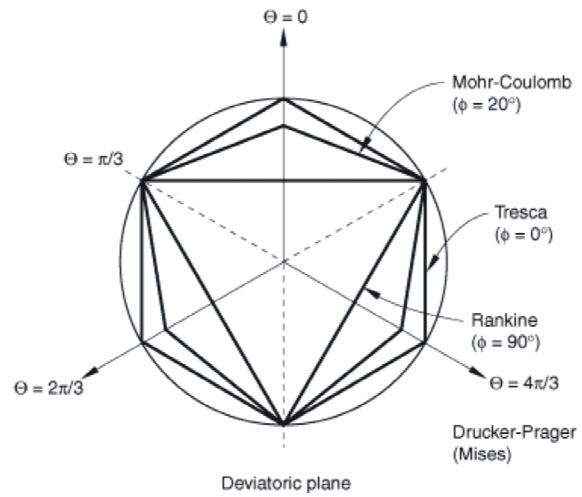


Figure 3.6. Mohr-Coulomb and tension cutoff surfaces. a) In meridional plane. b) In deviatoric plane (Abaqus Analysis User's Manual, 2010).

4 Results

4.1 The 3D Finite Element Model

This section presents the model geometry, the discretization of continuum geometry, used initial conditions, boundary conditions, and applied load to the models. The deformation of the overriding plate of the South American subduction zone, as a result from the applied initial conditions, load and boundary conditions to the models are presented in the next section. Two sets of model geometries are chosen named as ‘Northern segment model’ and ‘Southern segment model’ to carry out the present project. Both models are different in their geometric features. The slab dip and topographic slope angles are different for both models, which are chosen from Hoffmann-Rothe et al. (2006). The geometries of the Northern segment model and Southern segment model correspond to the Northern Andes (20°S-25°S) and the Southern Andes (36°S-40°S). Geometries of both models are highly simplified in order to understand the control of geometry and homogenous rheological layering on the deformation pattern of the overriding plate.

4.1.1 Initial assumptions

The following assumptions are considered as the most important:

- The generalised geometry reflects the first order feature of the geological units.
- The spherical shape of the Earth is ignored.
- The rheological properties are assigned in the form of homogeneous layering.

4.1.2 Model Geometry

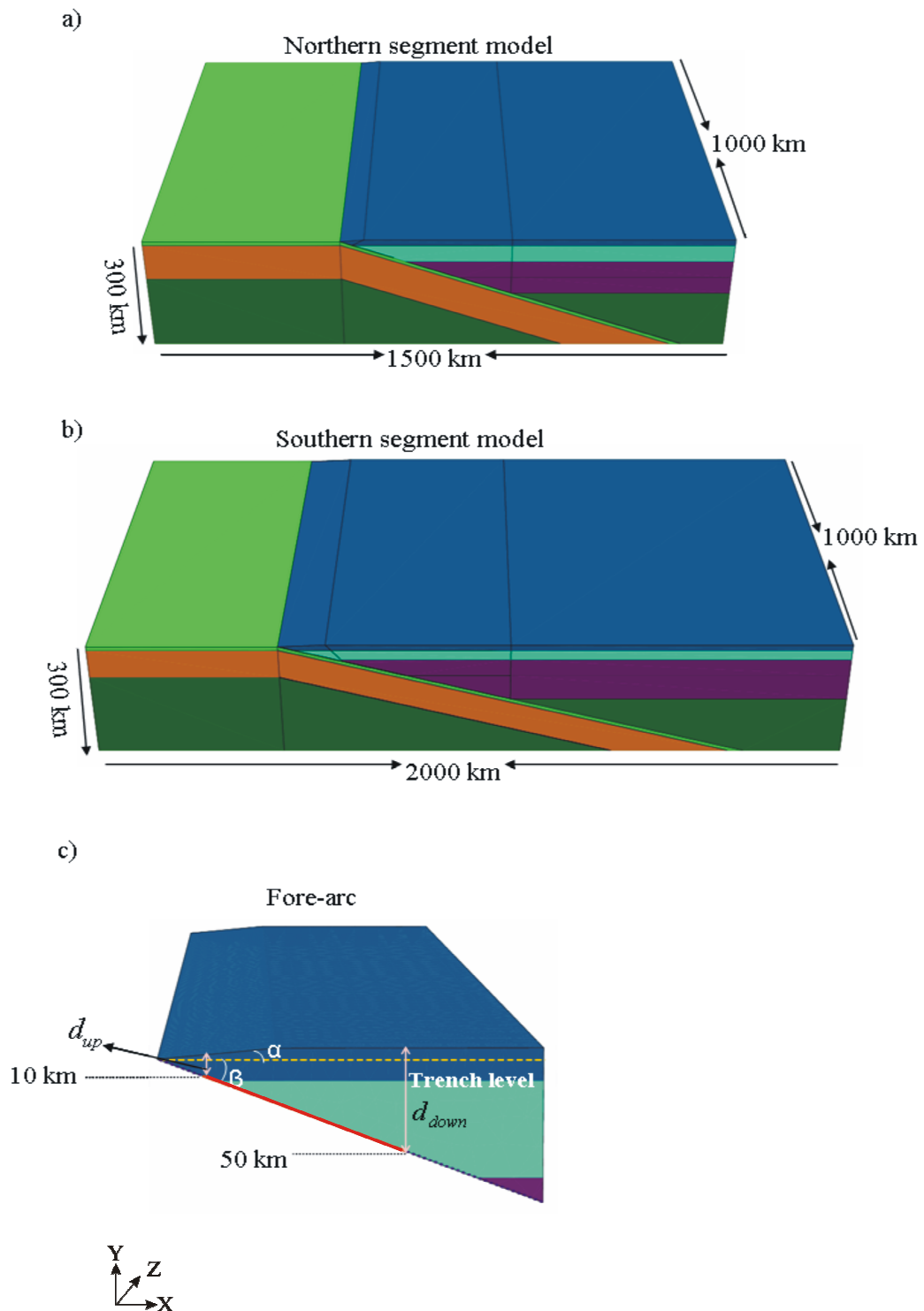
Figure 4.1 presents the geometry of the models. The depth extent (along Y-axis) for both models is taken to be 300 km. East-West expansion (along X-axis) is 1500 km and 2000 km for Northern and Southern segment model, respectively. The subducting slab is longer to reach the depth of 300 km in the Southern segment model (with shallower dip angle). Both models have 1000 km expansion in North-South (along Z-axis) direction. The large expansion is chosen in order to minimize the boundary effects. Both models consist of four different parts representing four different units:

- Oceanic lithosphere
 - a) *Oceanic crust (OC)*
 - b) *Oceanic mantle (OM)*
- Continental lithosphere
 - a) *Continental upper crust (CUC)*
 - b) *Continental lower crust (CLC)*
 - c) *Continental mantle (CM)*
- Oceanic asthenosphere (OA)
- Continental asthenosphere (CA)

All these units are assembled in the commercial finite element software Abaqus (Abaqus User's Manual, 2010) and assigned contact interaction properties (friction or frictionless). In both models, there is a frictionally coupled zone at the interface between the overriding plate and the subducting plate and shown by the red line in Figure 4.1c. All other units of the models have frictionless contact interaction.

Stein and Stein (1992) showed that limiting oceanic lithospheric plate thickness is the crucial parameter in determining the best fit to the thermal observations. Fowler (2005) compared thermal parameters for the oceanic lithosphere and suggest 95 ± 10 km as the thickness of the oceanic lithospheric plate for the "Global depth and heat flow model 1" (GDH1) (see also Stein and Stein, 1992). The thickness of the oceanic lithosphere in the present study is based on the "GDH1" model having a depth of 105 km for the Northern segment model and 85 km for the Southern segment model, as the oceanic lithosphere of the Southern Andes is younger than of the Northern Andes. The thickness of the crust of the oceanic lithosphere is 10 km for both models. The thickness of the continental upper crust is 15 km and is 45 km for continental lower crust. The mantle region below the continental crust has a thickness of 90 km.

Hoffmann-Rothe et al. (2006) estimated the geometry of the fore-arc wedge between the trench line and the 50 km depth contour of the slab with the averaged slab dip angle and the averaged slope angle for the South American subduction zone with the assumption that the fore-arc crust has constant internal strength.



Further, they considered the interaction force between the overriding and subducting plates as the potential factor controlling the deformation of the fore-arc of the South American subduction zone. The interaction force depends directly on the geometry of the subducting slab. Therefore, the geometries of models are constrained by the averaged slab dip angle (β) and averaged topography slope angle (α) as shown in Figure 4.1c. The dip of the slab is assumed to be a constant and taken as 18.4° for the Northern segment model and 13.4° for the Southern segment model. In the models, the topography of the wedges is simplified using averaged topography for the Northern and Southern segment and is taken 4.7° and 2.3° for the northern and southern segments, respectively.

4.1.3 Discretization/meshing of geometry

The model geometries were discretized or meshed into continuum linear 3D tetrahedron elements (named as C3D4 in Abaqus). The average mesh resolution for asthenosphere is 70 km and the average size of elements for oceanic lithosphere is 10 km. As the slab dip angle for the Southern segment model is shallower than for the Northern segment model, which in turn gives a shallower fore-arc in the Southern segment model as compared to the Northern segment model and therefore was meshed with smaller size tetrahedron elements. The average size of elements for the continental lithosphere is 20 km and 15 km for the Northern and Southern segment model, respectively. Figure 4.2 shows the meshed geometry of the models.

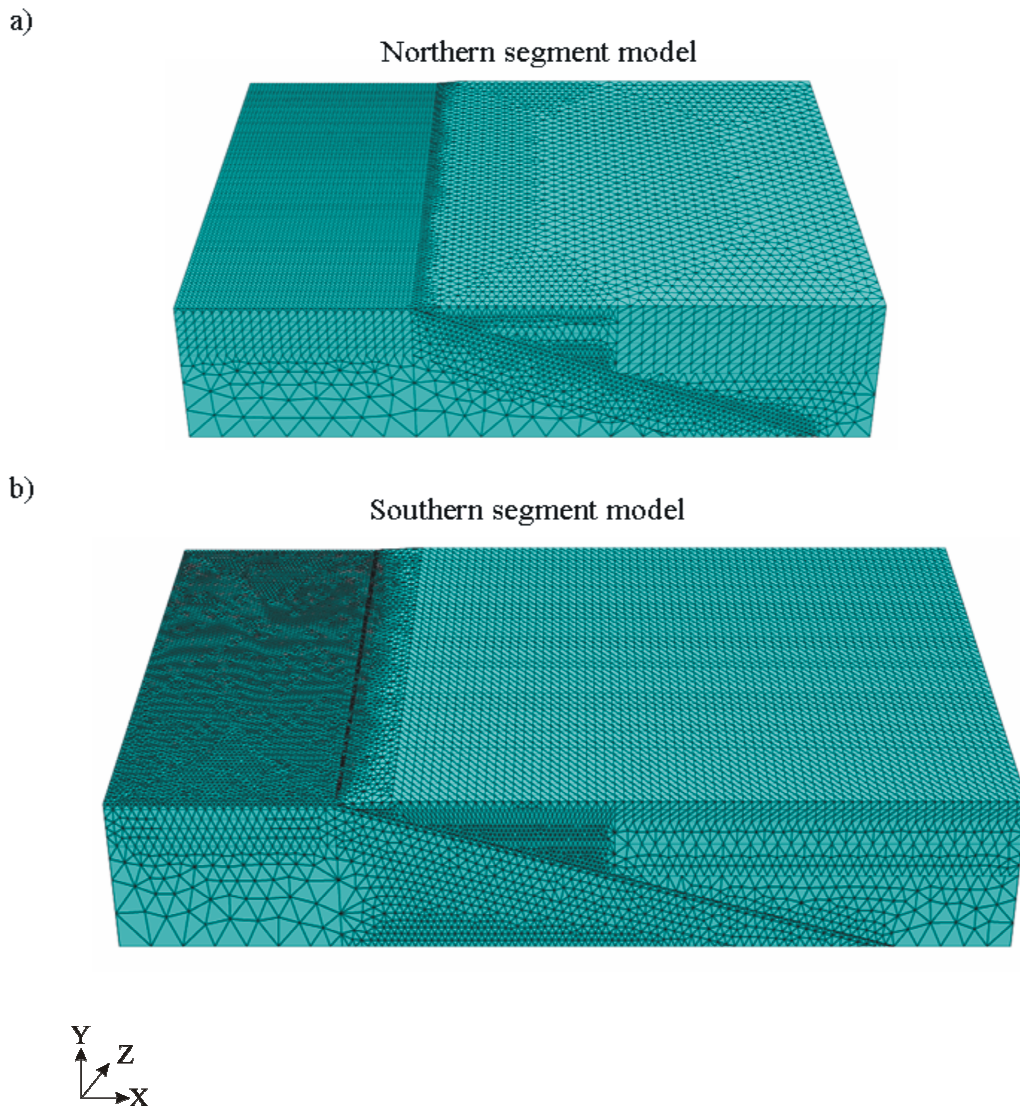


Figure 4.2. The discretized geometries with 3D linear tetrahedron elements for both models: a) The Northern segment model: Total number of elements = 535989. b) The Southern segment model: Total number of elements = 627177.

4.1.4 Contact sliding

After meshing, every contact surface was assigned a contact interaction property (friction or frictionless sliding). The Altiplano-Puna Plateau was created as a consequence of tectonic shortening which occurred in the Central Andes during the Cenozoic (Isacks, 1988; Allmendinger and Gubbels, 1996; Allmendinger et al., 1997; Lamb et al., 1997; Kley and Monaldi, 1998; Giese et al., 1999). Lamb and Davis (2003) argued that the aridization of the global climate decreased the sedimentary fill in the trench and lead to increase in plate coupling in the late Cenozoic. For investigating the effect of varying plate coupling on the upper plate deformation, a frictionally coupled zone between the overriding plate and the subducting plate was developed in the models as shown in Figure 4.3 and the red

line representing the frictionally coupled zone between the subducting and the overriding plate. All other contact interfaces have frictionless sliding. Both models have the identical contact properties.

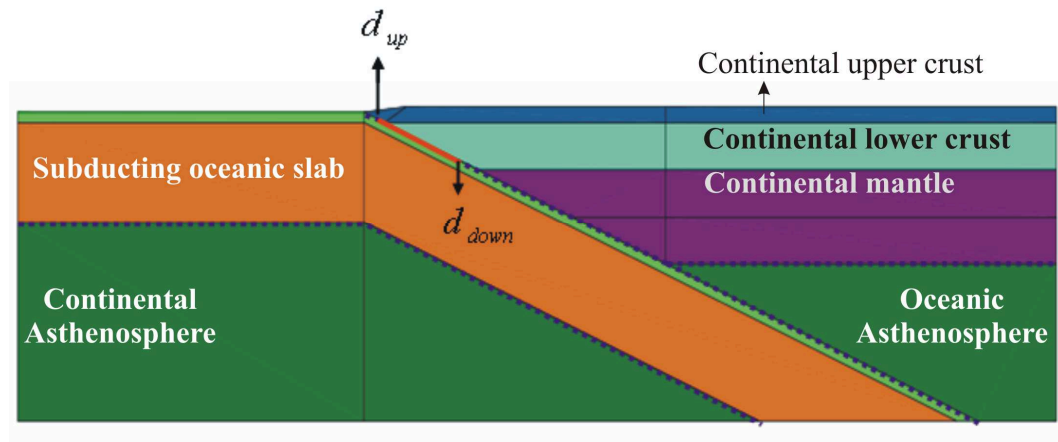


Figure 4.3. 2D view of the model showing applied contact interactions: the red line represents the frictionally coupled zone between the subducting and the overriding plates. d_{up} and d_{down} are the updip and downdip limits of the frictionally coupled zone and taken as average value of 10 km and 50 km, respectively. The purple dotted line denotes the frictionless contact interaction.

The interface coupling was explained by the distribution of asperities (the locked zones that resist the motion between two plates, where the inter-seismic strain accumulates and results in a release of high seismic moment at the time of rupture) on the plate interface (Kanamori, 1986; Pacheco et al., 1993; Scholz, 1998; Lay and Schwartz, 2004). Ruff and Kanamori (1983) related directly the maximum earthquake size to the asperity distribution on the fault plane and also suggested that all subduction zones are noticeably uncoupled below 40 km depth. The coupling force (shear force) at the coupled plate interface is the main factor affecting the plate coupling (asperities) differences at different subduction zones. The coupling force (F_0) resulting from the shear stresses over a frictionally coupled plate interface in a subduction zone is given by equation 4.1 (Wang and He, 1999).

$$F_0 = \frac{1}{2} \mu' W (d_1 + d_2) \rho g \quad (4.1)$$

where μ' is the coefficient of friction, W is the downdip width of the coupled zone, d_1 and d_2 are the depths of its updip and downdip ends, respectively, ρ is the density and g is acceleration due to gravity. Equation 4.1 shows that the shear

force at a coupled interface depends on the width of the frictionally coupled part of the interface (W), depth of updip (d_1) and downdip (d_2) ends of coupled zone and to the effective coefficient of friction (μ').

After Wang and Suyehiro (1999) the downdip limit of the seismogenic zone can be taken for the depth extent of the frictionally coupled zone. On the basis of inter-plate thrust earthquakes ($M > 6$), Tichelaar and Ruff (1991) estimated the seismic coupling depth as 48–53 km in the southern region of 28°S, while the northern domain of this latitude has 36–41 km as the maximum coupling depth. The GPS observations from Klotz et al. (2001) suggested a non uniform coupling depth pattern along-strike of the South American subduction zone, and this coupling depth is about 33 km in the north of 30°S, while south of 35°S the coupling depth reaches nearly 50 km. Temperature has a control on the frictionally coupled zone. The updip transition from stable to stick-slip sliding occurs at about 100°C i.e. depth of about 2 to 10 km; while the downdip transition from stick-slip to stable sliding on the plate interface takes place at 350°C (Oleskevich et al., 1999). In the old oceanic crust subduction, temperature of 350°C on the thrust interface often reaches below the depth of 50-60 km, which is too deep, since thrust earthquakes are not observed at those depths. For this case Tichelaar and Ruff (1991, 1993) and Oleskevich et al. (1999) suggested that the stable-sliding appears at the depth where the subducting slab meets the fore-arc continental Moho at an average depth of 35-50 km.

In addition to the updip and downdip limits of the frictionally coupled interface, the coefficient of friction at the plate interface also plays an important role in deforming the overriding plate. Sobolev et al. (2006) argued that the shear coupling at the plate interface controls the intensity of tectonic shortening in the Andean Orogeny and suggested 0.05 and 0.015 as the friction coefficients for Central and Southern Andes, respectively. Their Central Andean finite element model with a friction coefficient of $\mu > 0.10$ resulted in slab break-off and termination of subduction. Kellner (2007) suggested a coefficient of friction of 0.4 and 0.33 for the northern and southern segment, respectively.

For establishing a frictional contact (asperities) between the overriding and subducting plate average values for updip ($d_1 = 10$ km) and downdip ($d_2 = 50$ km) of the frictionally coupled zone were taken for models, giving the downdip width

of frictionally coupled (seismogenic) zone as 126 km for Northern segment model and 172 km for Southern segment model.

4.1.5 The Boundary conditions and applied load

As results of finite element analysis depend on the chosen boundary conditions, it becomes important to select the appropriate boundary conditions for simulating the behaviour of the American subduction zone to get realistic results.

For accomplishing this purpose, the whole simulation was divided into two static steps. The static response of the uniformly distributed gravity load in the model was calculated in step 1. In this step the bottom of the models was allowed only to move in the horizontal direction (X) with restriction in the other two directions. The vertical boundaries of the models were able to move only in vertical direction (Y) (Figure 4.4). The initial stress field needed for establishing the equilibrium in the model was calculated from the step 1 and results are presented in the next section 4.2.

In step 2, the velocity boundary conditions were applied to the models and were specific for individual cases. Some models had run with only slab pull velocity as boundary condition and some models had run with simultaneous slab pull and continental drift velocities. The reference model had run with ridge push velocity, slab pull velocity, and continental drift velocity as boundary conditions. The bottom of the asthenospheric unit (both oceanic and continental asthenosphere) of the model had the same boundary conditions as described in step 1 and the vertical boundaries of the asthenospheric part of the models were fixed in all directions in all cases of step 2. The bottom of the oceanic lithosphere was allowed to move horizontally and vertically (X and Y directions) and movement in third direction was fixed for this step. The left side of the oceanic lithosphere was allowed to move only in horizontal direction. The right side of the model (continental lithosphere) was allowed to move in horizontal direction only in cases where continental drift velocity was applied and for the rest of the cases the right side of the model was fixed in all directions. The applied velocity boundary conditions and gravity load for both steps are shown in Figure 4.4. Both models have identical boundary conditions and loads.

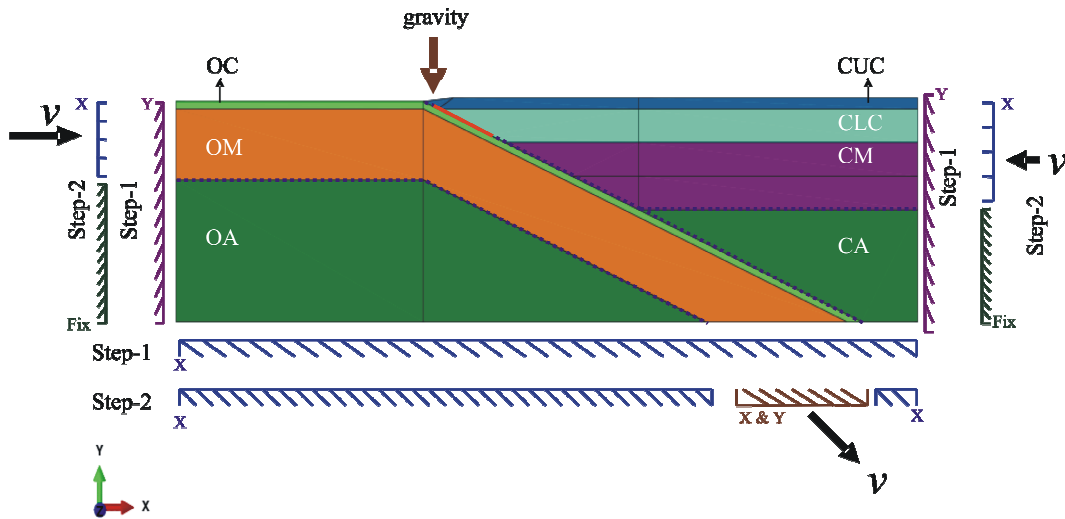


Figure 4.4. Section of the model showing the applied boundary conditions and loads for the reference model: whole simulation is divided into two steps having different boundary conditions. Blue denotes the boundary condition representing movement in X-direction. Purple denotes the boundary conditions showing movement in Y-direction. Brown marks the boundary condition representing movement in both X and Y-directions. Dark green denotes the fixed boundary condition in all directions. The black arrows represent the velocity boundary condition and the brown arrow represents the uniformly distributed gravity load. The red line shows the frictionally coupled zone and the dotted purple line denotes frictionless contact interaction. OA, oceanic asthenosphere; OM, oceanic mantle; OC, oceanic crust; CUC, continental upper crust; CLC, continental lower crust; CM, continental mantle; CA, continental asthenosphere.

4.1.6 Rheological parameters

Sobolev and Babeyko (2005) and Sobolev et al. (2006) presented the large-scale thermo-mechanical numerical model for the Central Andes with realistic viscoelastic-plastic rheology. Babeyko and Sobolev (2008) presented a zoom-in of the large-scale model of Sobolev et al. (2006) and showed the stress distribution in the viscoelasto-plastic subducting slab.

The elasto-plastic rheological parameters for both models were taken from Babeyko and Sobolev (2008). The rheological parameters used in the models are given in Table 4.1. The identical geological units of the different models have the same material properties.

Table 4.1 Material parameters used for both models (Babeyko and Sobolev, 2008)

Model unit	Density [kg/m ³]	Bulk modulus [GPa]	Young's modulus [GPa]	Poission's ratio	Friction angle [°]
Continental upper crust	2750	55	82.5	0.25	20
Continental lower crust	2950	63	94.5	0.25	20
Continental mantle	3300	122	183	0.25	10
Oceanic crust	3000	63	94.5	0.25	20
Oceanic mantle	3280	122	183	0.25	10
Asthenosphere (both oceanic & continental)	3300	122	183	0.25	10

4.2 Vertical Deformation

The main characteristic of the South American continental deformation is its remarkable variation in geological history and tectonic evolution. It is generally thought that the physical parameters such as overriding plate motion, slab width, and slab age have influence on the formation of Andes (Somoza, 1998; Hampel and Pfiffner, 2006; Iaffaldano et al., 2006; Schellart et al., 2007). The sediment thickness at the trench has relations with the overriding plate deformation by affecting the strength of coupling at the plate interface (Lamb and Davis, 2003). In addition, temperature and pressure also have a great importance in changing the deformation pattern of the South American continental plate. The aim of this study is to find the correlation between these parameters and the overriding plate deformation.

The applied plate movements and the strength of the frictionally coupled zone have combined mechanical effects on the deformation of the South American continental plate. To understand the underlying mechanism, different values for the coefficient of friction at the frictionally coupled zone between the subducting and the overriding plates were assigned to both the models and different boundary conditions for plate movement as shown in Table 4.2.

Table 4.2 Different boundary conditions applied to the models

Model	Applied boundary conditions
Model I (Reference model)	Slab pull, slab push and overriding plate velocity
Model II	Slab pull and overriding plate velocity
Model III	Only slab pull velocity

The slab pull velocity was applied at the bottom of the oceanic lithosphere and the slab push velocity was applied at the left end of oceanic lithosphere towards the trench. The overriding plate velocity was applied at the right end of the continental lithosphere towards the trench (Figure 4.4).

The coefficients of friction (μ) = 0.1, 0.2, and 0.5 were considered for all models in this study, which are in agreement with the previous estimates (Byerlee, 1978; Peacock, 1996; Hassani et al., 1997; Cattin et al., 1997; Scholz, 1990; Tichelaar and Ruff, 1993; Kellner, 2007). In addition, the frictionless ($\mu = 0.0$) plate interface was also considered to observe the effect of plate movement. The other parameters such as running time, rheology, and geometry were identical for all models unless specified. The plate movements were applied to impose the deformation in the overriding plate for 500000 years.

The movement rate for the subducting plate had been taken as 5 cm/yr and 3 cm/yr for the overriding plate for all models (Somoza, 1998; Silver et al., 1998; Sobolev et al., 2006) and was applied as kinematic boundary condition as described in Table 4.2. The applied velocity at the bottom of the oceanic lithosphere was divided in horizontal and vertical components (Table 4.3).

Table 4.3 Velocity components applied to the model

Slab dip angle (β)	v_x [cm/yr]	v_y [cm/yr]
18.4°	4.79	1.58
13.4°	4.88	1.17

The results are presented graphically for the two points on the overriding plate; at 200 km and at 400 km east of the trench. The point at 400 km east of the trench lies in between the 350 km and 450 km east of the trench corresponding to the

Altiplano plateau position. For the comparative study the point at 200 km east of the trench is chosen that corresponds to the magmatic arc. The colour coding in the legend for pictures and in the graphs is the same throughout the study. The results are assessed by evaluating the deformation rate of the overriding plate with the geological uplift rate for Altiplano plateau. In the legend for the vertical displacement, negative value represents vertical displacement in downward direction (subsidence) and a positive value represents vertical displacement in upward direction (uplift).

4.2.1 Model I: Reference model

In this model, the boundary conditions as described in Table 4.2 were applied to achieve the estimated uplift rate of 0.2 mm/yr (Gregory-Wodzicki, 2000) for the Altiplano plateau region. It was observed that the uplift rate of the overriding plate was decreased with increase in the coefficient of friction at both points 200 km and 400 km east of the trench. Further, the uplift rate was higher at a point 200 km as compared to 400 km east of the trench for the same coefficient of friction (Figure 4.6).

The combined mechanical effect of the described boundary conditions and applied gravity load at coefficient of friction ($\mu = 0.14$) created an uplift of approximately 103 m in 500000 years in the Altiplano plateau region. The uplift is shown in Figure 4.5a as a black point at a distance of approximately 400 km east of the trench.

The deformation of the overriding plate showed inverse relation with the coefficient of friction. It is shown in Figure 4.5b.

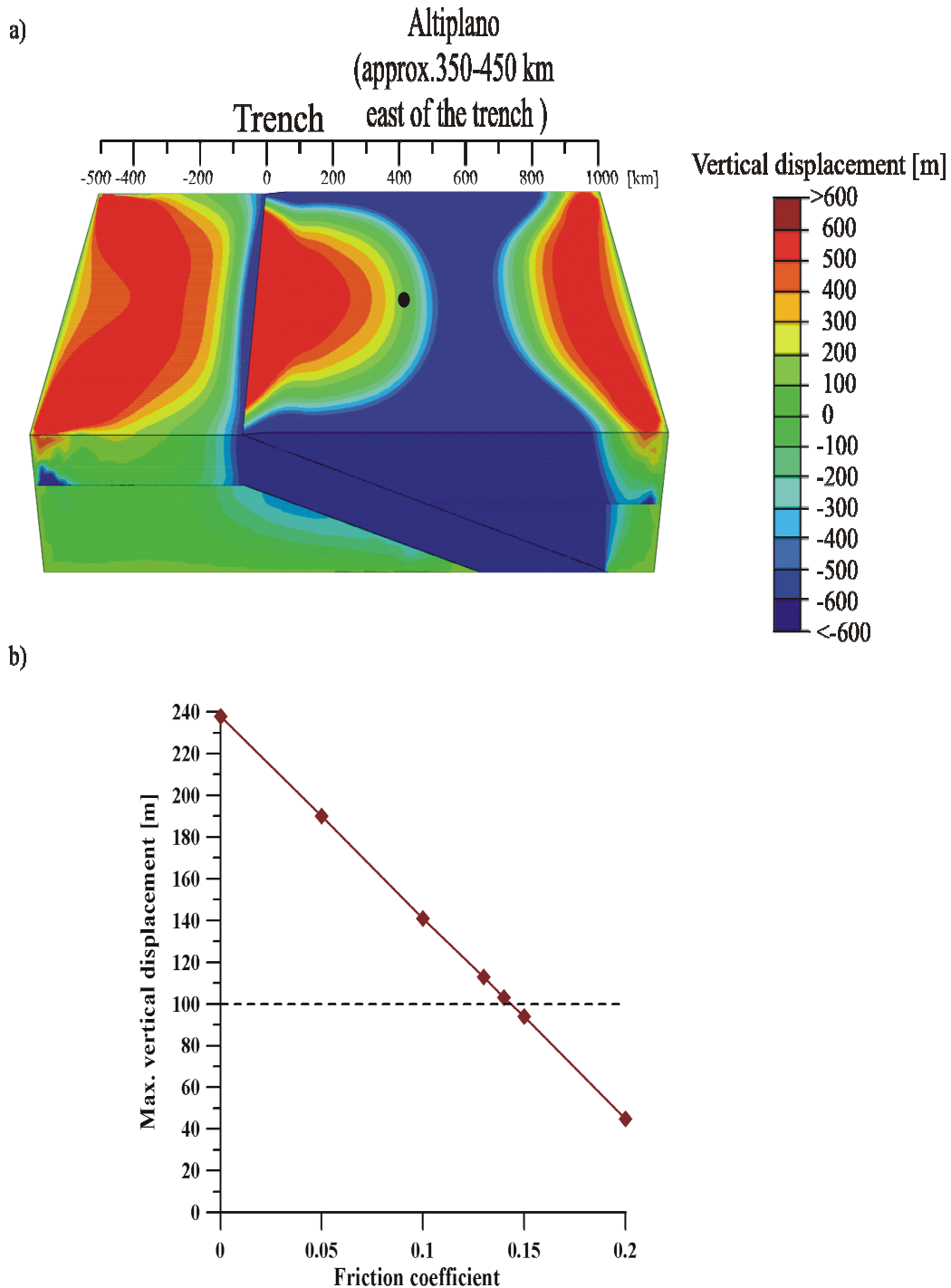


Figure 4.5. Maximum vertical displacements of the overriding plate when slab pull, slab push, and overriding plate velocities are applied simultaneously: a) For the coefficient of friction ($\mu = 0.14$) at the frictionally coupled zone. The black point represents the Altiplano region and is positioned at approximately 400 km east of the trench. b) Maximum vertical displacement at a point 400 km east of the trench as a function of inter-plate friction. The black dashed line represents the amount of uplift after 500000 years that is equivalent to the estimated geological uplift rate of 0.2 mm/yr for the Altiplano plateau by Gregory-Wodzicki (2000).

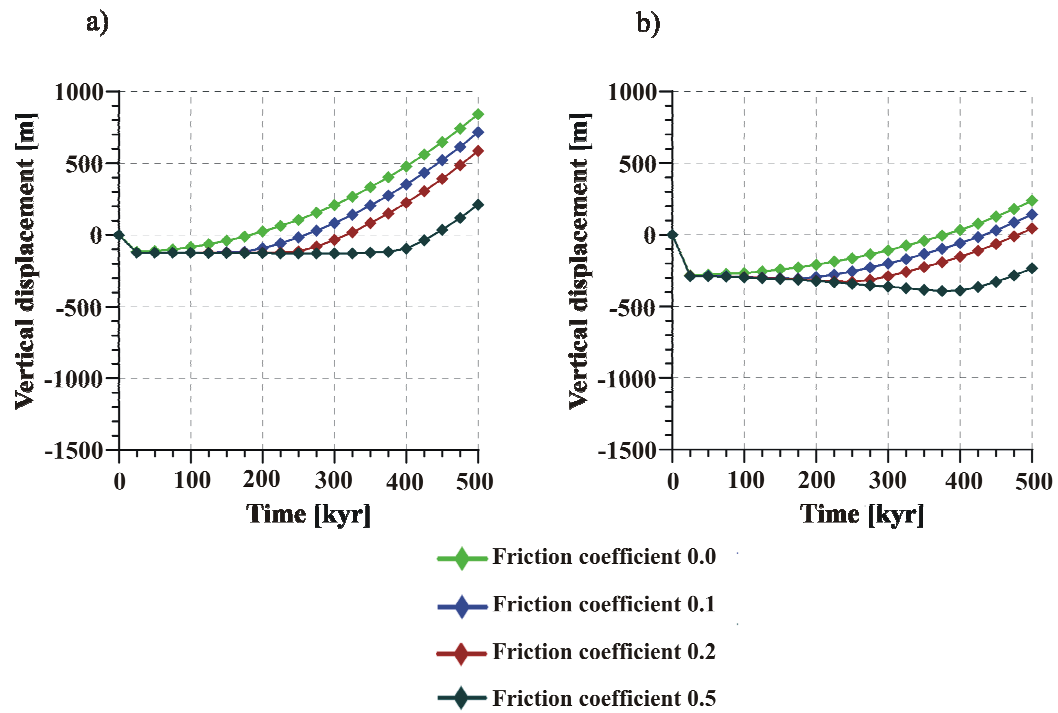


Figure 4.6. The deformation rate: a) At point 200 km east of the trench. b) At point 400 km east of the trench.

4.2.2 Model II: Simultaneous slab pull and overriding velocities

When the overriding plate moved towards the trench, uplift was created in it at both points (200 km and 400 km east of the trench). The uplift rate was found to depend on the coefficient of friction. The maximum overriding plate uplift was observed for no friction ($\mu = 0.0$) as shown in Figure 4.7a. When coefficients of friction ($\mu = 0.1, 0.2, 0.5$) were applied, the uplift rate was decreased with an increase in coefficient of friction at both points (200 and 400 km east of the trench) as shown in Figure 4.7b-d. Further, vertical displacement was calculated for both points at different coefficients of friction. At point 400 km east of the trench the model without friction ($\mu = 0.0$) created an uplift of only 23 m in 500000 years as shown in Figure 4.8. Uplift was observed at point 200 km east of the trench in the models with friction ($\mu = 0.0, 0.1, 0.2$).

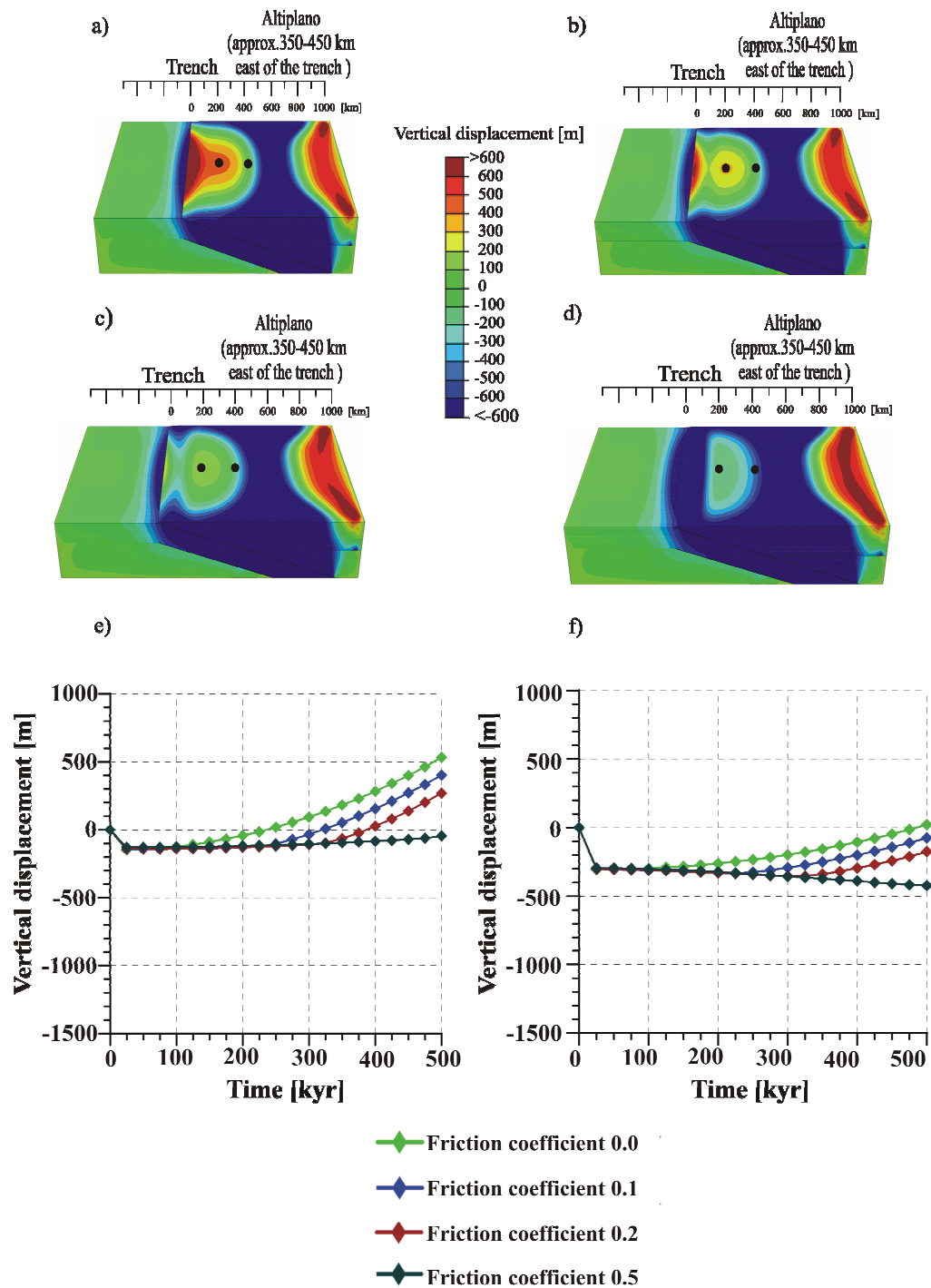


Figure 4.7. Maximum vertical displacements of the overriding plate when slab pull and overriding plate velocities are applied simultaneously: a) Without friction ($\mu = 0.0$); b) with coefficient of friction ($\mu = 0.1$); c) with coefficient of friction ($\mu = 0.2$); d) with coefficient of friction ($\mu = 0.5$); e) The deformation rate for the point 200 km east of the trench; f) The deformation rate for the point 400 km east of the trench.

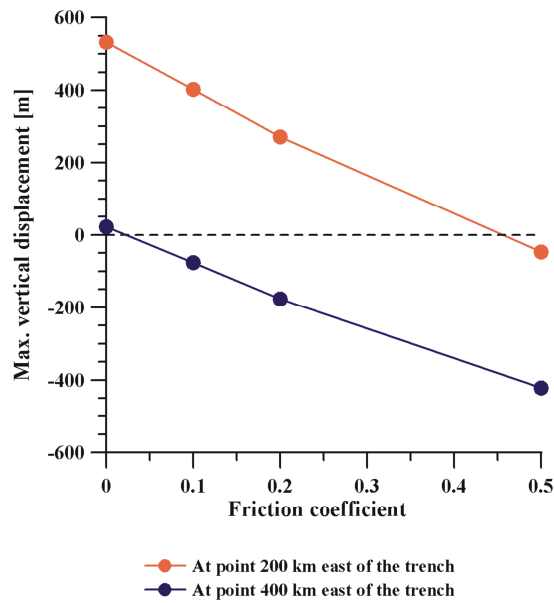


Figure 4.8. Maximum vertical displacement of the overriding plate as a function of inter-plate friction coefficient.

4.2.3 Model III: Slab pull velocity only

The combined effect of slab pull velocity and the gravity force created subsidence in the overriding plate for all coefficients of friction ($\mu = 0.1, 0.2, 0.5$) except the coefficient of friction ($\mu = 0.0$). The model without friction ($\mu = 0.0$) generated a small uplift region close to the trench up to a distance of approximately 20 km east of the trench as shown in Figure 4.9.

Figure 4.9e shows the development of vertical deformation at point 400 km east of the trench on the overriding plate with time for different coefficient of friction. For the case of zero friction ($\mu = 0.0$), the subsidence rate in the overriding plate was least and an increase in friction ($\mu = 0.1, 0.2, 0.5$) enhanced the subsidence rate of the overriding plate.

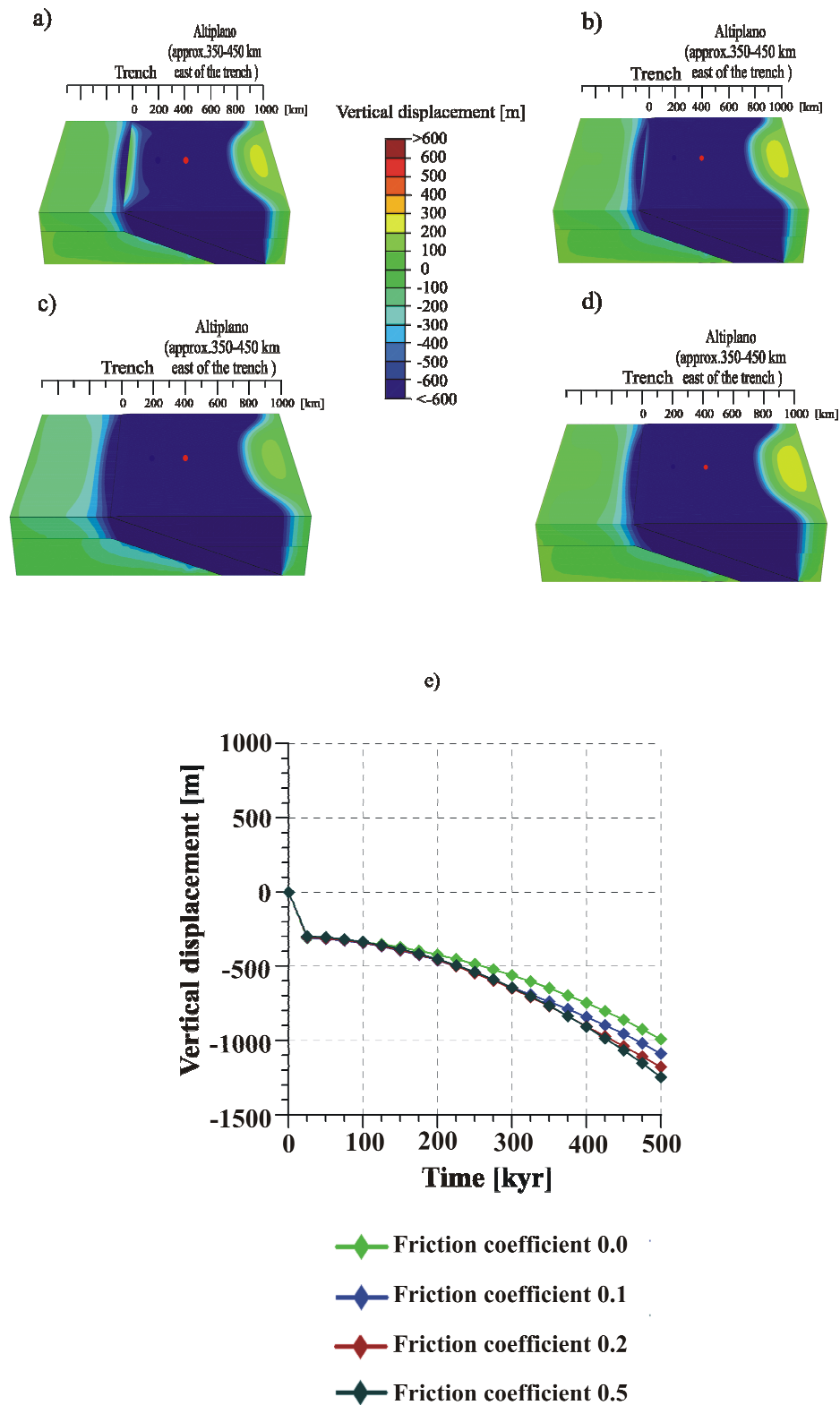


Figure 4.9. Maximum vertical displacement of the overriding plate when only slab pull velocity is applied: a) Without friction ($\mu = 0.0$); b) with coefficient of friction ($\mu = 0.1$); c) with coefficient of friction ($\mu = 0.2$); d) with coefficient of friction ($\mu = 0.5$); e) The deformation rate for the red point is visible in the model at point of 400 km east of the trench.

4.2.4 Effect of the thickness of the continental crust

To study the effect of the thickness of the continental crust on the overriding plate deformation, the thickness of the continental crust was reduced to approximately 40 km. The same boundary conditions as described for model II with reduced continental crust were applied. Further, the vertical displacement of model II was compared with the vertical displacement of this case and higher uplift was observed as compared to Model II (Figure 4.10). Models without friction ($\mu = 0.0$), having thin continental crust showed an uplift of approximately 425 m in 500000 years at point 400 km east of the trench with an uplift rate of 0.9 mm/yr for the Altiplano plateau region. It is too high as compared to the geological estimated uplift rate suggested by Gregory-Wodzicki (2000). The trend of decrease in the overriding plate uplift with the increase in inter-plate friction coefficient is the same as discussed in section 4.2.2.

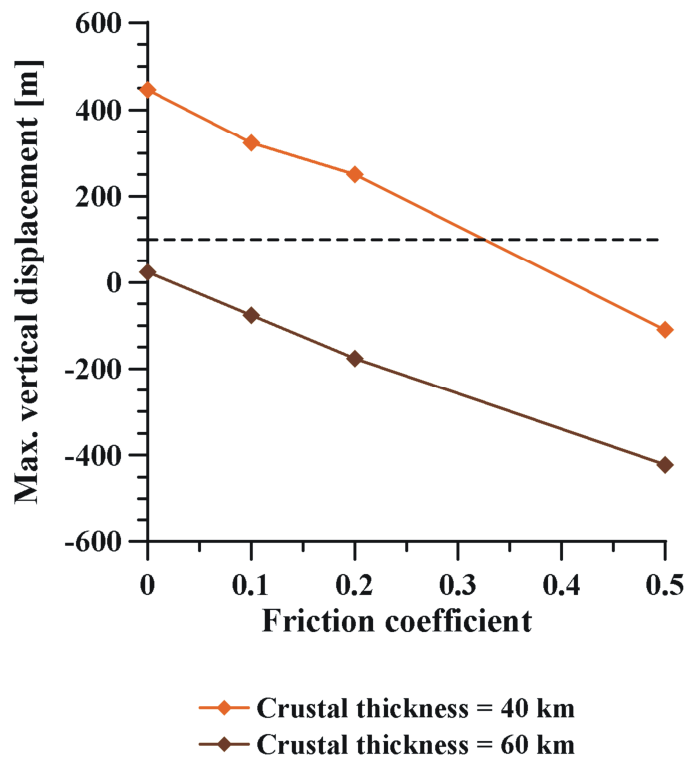


Figure 4.10. Maximum vertical displacement of the overriding plate (at a point lies on the Altiplano plateau region i.e. at 400 km east of the trench) as a function of inter-plate friction coefficient: The horizontal dashed line represents the geologically estimated uplift of 100 m for 500000 years for the Altiplano plateau, which corresponds to the uplift rate of 0.2 mm/yr for the Altiplano plateau (Gregory-Wodzicki, 2000).

In the model with a 40 km thick continental crust (thin crust), the inter-plate friction coefficient between 0.3 and 0.35 (i.e. $0.3 < \mu < 0.35$) can produce an uplift

rate of 0.2 mm/yr, comparable to geologically estimated uplift rate by Gregory-Wodzicki (2000) for the Andean plateau region.

4.2.5 Effect of varying continental drift velocity

To analyse the effect of continental drift velocity on overriding plate uplift, a varying spectrum of overriding velocities towards the trench was applied. Boundary conditions are the same as for Model II. No uplift was observed for the velocities of 1 cm/yr and 2 cm/yr; however there was uplift generation for velocity of 3 cm/yr for all coefficients of friction (Figure 4.11).

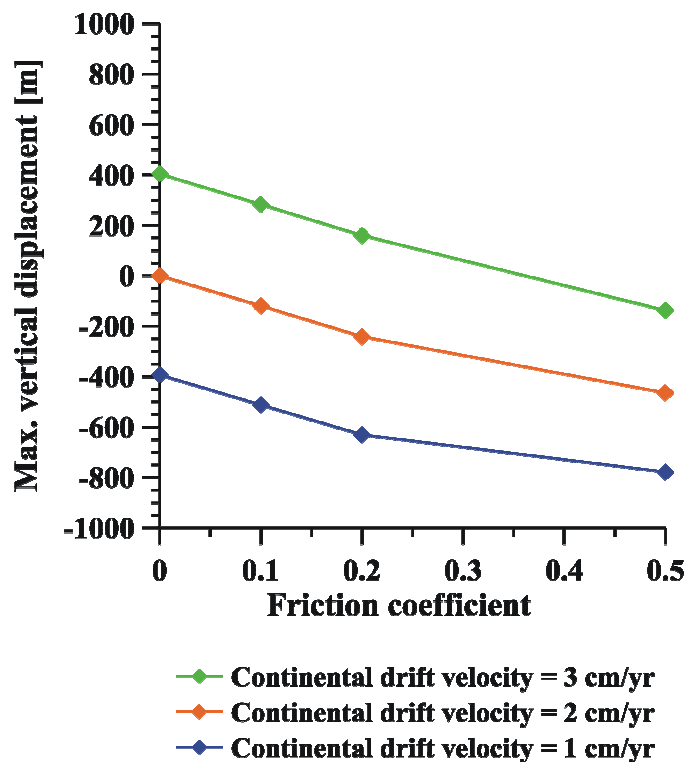


Figure 4.11. Maximum vertical displacement of the overriding plate as a function of inter-plate friction coefficient for different trench-ward continental drift velocities.

4.2.6 Effect of oblique convergence

Convergence between the subducting plate and the continental plate was simulated with a convergence angle (γ) of 20° (Kellner, 2007). The oceanic plate was moved with an oblique velocity of 5 cm/yr and the continental plate was moved with a straight velocity of 3 cm/yr towards the trench. The different coefficients of friction ($\mu = 0.0, 0.1, 0.2, 0.5$) were assigned at the frictionally coupled zone between the subducting and the overriding plate.

The model showed subsidence in the overriding plate at both points for coefficients of friction ($\mu = 0.0, 0.1, 0.2, 0.5$) except a very small uplift for no friction ($\mu = 0.0$) at point 200 km east of the trench (Figure 4.12).

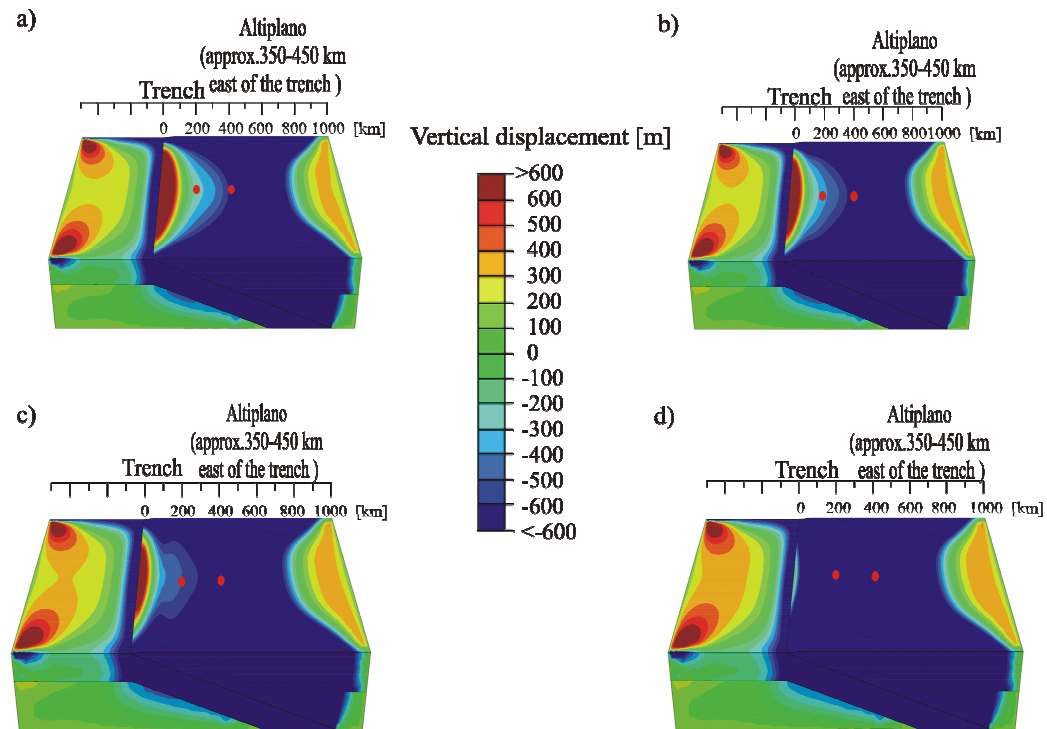


Figure 4.12. Development of vertical displacement of the overriding plate when the oblique convergence velocity of 20° angle is applied to the subducting plate for different coefficients of friction at the coupled plate interface: a) Without friction ($\mu = 0.0$); b) with coefficient of friction ($\mu = 0.1$); c) with coefficient of friction ($\mu = 0.2$); d) with coefficient of friction ($\mu = 0.5$). The red points lie at a distance of 200 km and 400 km east of the trench.

4.2.7 Effect of slab dip

To study the effect of slab dip angle, a Southern segment model with the shallower dip angle of $\beta = 13.4^\circ$ was designed in contrary to the Northern segment model which had a dip angle of $\beta = 18.4^\circ$. In this model, the oceanic plate with downward velocity (slab pull) of 5 cm/yr and the continental plate with straight velocity of 3 cm/yr were moved towards the trench. The different coefficients of friction were assigned as described previously. Figure 4.13 shows the development of vertical displacement with time for the point at 200 km and 400 km east of the trench. The uplift rate was lower as compared to model II with the dip angle of $\beta = 18.4^\circ$.

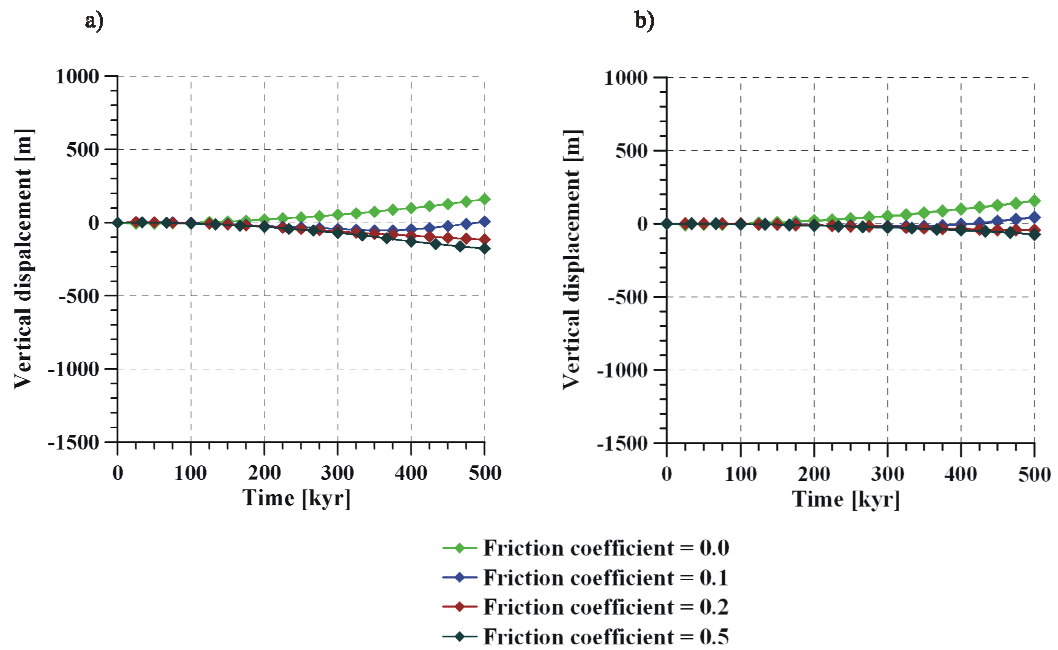


Figure 4.13. Deformation rate: a) At point 200 km east of the trench. b) At point 400 km east of the trench.

When the overriding plate deformation was compared for different slab dip angles ($\beta = 13.4^\circ$; 18.4°), the shallower subducting plate with the dip angle of $\beta = 13.4^\circ$, resulted in lower overriding plate deformation as compared to the dip angle of $\beta = 18.4^\circ$ (Figure 4.14).

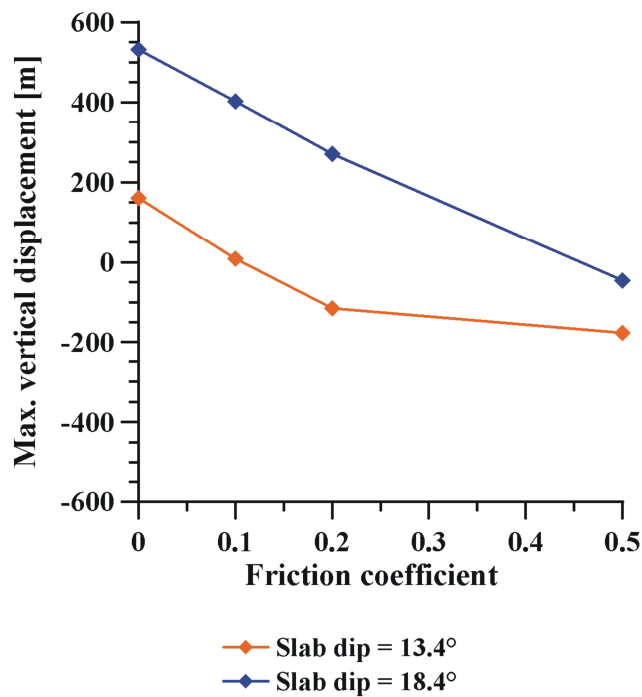


Figure 4.14. Comparison of vertical deformation as a function of inter-plate friction coefficient for different slab dip angles (β) at point 200 km east of trench.

5 Discussion and conclusion

The Earth processes such as movement of plates, generation of earthquakes, formation of volcanoes, and the mountains building are very important factors which affect the human life deeply. These processes also affect the thermal structure of the mantle, substantial surface (vertical and horizontal) deformations, and seismic energy release. Therefore, these processes play an important role in the geodynamical, geochemical, and geological phenomena that shape our Earth and attract the Earth Science community.

One of the most interesting Earth processes is subduction. It is the process that takes place at convergent boundaries by which one tectonic plate moves under another tectonic plate and sinks into the mantle as the plates converge. Subduction plays a important role in the recycling of the surface material by mixing it back to the deep Earth and introducing significant chemical variation back into the mantle (Christensen and Hofmann, 1994; Hofmann, 1997). Furthermore, it is also responsible for driving plate motions, mountain building, and the growth of new continental crust (Forsyth and Uyeda, 1975; Davidson and Arculus, 2006). When the functional cycle of the subduction zone is spectacularly disrupted due to continental crust, it may result in a mountain range building such as the Andes and the Himalayas (Allmendinger et al., 1997; O'Brien, 2001).

The Andes are one of the largest active plate-boundary zones, forming a mountainous region which extends over 5000 km along the western margin of South America as a result of the subduction of the oceanic Nazca plate beneath the South American plate (Dewey and Bird, 1970; Pardo-Casas and Molnar, 1987).

Most geophysicist propose that crustal shortening due to the convergence between the subducting Nazca plate and the overriding South American plate, is the major cause for the Andean uplift (Dewey and Bird, 1970; Isacks, 1988; Sheffels, 1990; Baby et al., 1992a; Dewey and Lamb, 1992; Allmendinger et al., 1997; Liu et al., 2002; Oncken et al., 2006; Sobolev et al., 2006).

Many researchers propose that the coupling strength at the plate interface between the Nazca and the South American plates or the motion of overriding plate plays a crucial role in the generation and maintenance of the deformation of the upper plate (Russo and Silver, 1996; Gutscher et al., 2000; Lamb and Davies, 2003;

Hampel and Pfiffner, 2006; Oncken et al., 2006). The coupling strength causes shear stress which in turn supports the high Andes formation (Lamb and Davis, 2003). To assess the role of the overriding plate and the effect of the interaction between the subducting and the overriding plate, the two crucial parameters are analysed: a) plate coupling strength defined by the inter-plate friction coefficient, and b) role of the overriding plate movement.

To achieve the estimated uplift rate of 0.2 mm/yr (Gregory-Wodzicki, 2000) for the Altiplano plateau region, the boundary conditions as described in Table 4.2 were applied to the reference model. The combined mechanical effect of the described boundary conditions and applied gravity load at a coefficient of friction $\mu = 0.14$ produce an uplift of approximately 103 m in 500000 years at point 400 km east of the trench. This gives an uplift rate of 0.2 mm/yr for the Altiplano region.

Cattin et al. (1997) studied the effect of long term coupling on the fore-arc topography for three subduction zones: northern Chile, northern Japan, and Tonga by using a 2D finite element model with specific geometry and kinematic boundary conditions. They assumed that traction arising from friction is one of the stresses acting on topography. They propose that while the intrinsic coefficient of friction for small rock samples is high ($\mu \sim 0.6-0.8$), however the friction coefficient larger than 0.2 is inconsistent with the observed topography of the fore-arc region. In the present study also, the proposed uplift rate of the Altiplano region is found consistent with the coefficient of friction ($\mu = 0.14$), which is < 0.2 and is in good agreement with Cattin et al. (1997).

In another study, the coexistence of trench-arc compression and back-arc tension is only possible for a coefficient of friction lower than 0.1 (Hassani et al., 1997). Further, Kellner (2007) proposed that the preferred coefficients of basal friction (μ_b , north = 0.4, μ_b , south = 0.33) for the Chilean subduction zone. However, it is higher compared to the present findings and it might be due to the differences between the chosen rheology and the model geometry. Sobolev et al. (2006) used coupled thermo-mechanical 2D models and showed that the thicker continental crust with the friction coefficient ($\mu=0.05$) at the Nazca-South American plate interface imitates the crustal structure and evolution of the high Central Andes. However, the thinner continental crust with a lower friction coefficient ($\mu < 0.015$) results in less shortening in the South American plate, replicating the

situation of the crustal structure and evolution of the Southern Andes. The discrepancies might be due to model set up; as they used thermo-mechanical 2D models as compared to this study and further, they employed a realistic temperature-and stress-dependent visco-elastic rheology.

When different coefficients of friction were applied, it was observed that the amount of uplift of the overriding plate at both points 200 km and 400 km east of the trench was decreased with increase in the coefficient of friction. This inverse relation between the overriding plate uplift (vertical displacement) and the inter-plate friction was also observed by Van Dinther et al. (2010) (Figure 5.1).

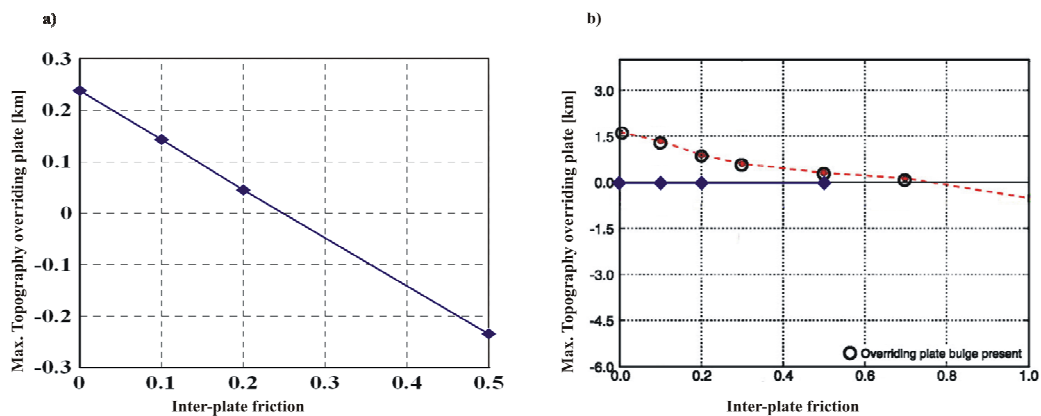


Figure 5.1. Decrease in the maximum topography of overriding plate as a function of inter-plate friction: a) From the present study: run time 500000 yr. b) Red dashed curve: from the model of Van Dinther et al., (2010): run time is 3.16 Myr. Solid dark blue curve: from the present study. Because the run time of the present study is shorter as compared to the run time of Van Dinther et al., (2010), the decreasing trend of the present study becomes nearly horizontal when it is fit to the Van Dinther et al., (2010) graph-scale.

Effect of the trenchward overriding plate movement

To analyse the effect of the trenchward overriding plate movement in the 3D geometry, the slab pull velocity and the trenchward overriding velocity were applied to the oceanic plate and overriding plate, respectively (see section 4.2.2).

With a stable (fix) overriding plate, no uplift was observed in the overriding plate. However, the uplift was generated with the trenchward overriding plate movement and it was found that increase in the friction causes decrease in uplift rate as the upper plate subsides by the drag of the subducting plate. Further, it was observed that higher friction only amplifies the drag and increases the amount of subsidence in the overriding plate. This phenomenon was also observed in

previous studies with 2D modelling approaches (Hampel and Pfiffner, 2006; Van Dinther et al., 2010).

Hampel and Pfiffner (2006) proposed that the trenchward moving overriding plate is a key factor for the development of mountain belts at the convergent margins. They showed that the subduction of the oceanic plate in the absence of an upper plate trenchward motion even with high inter-plate coupling does not support the Andean type uplift. Friction along the plate interface supports the high topography only, if the upper plate is moving towards the trench.

Buiter et al. (2001) showed that an increase in friction along the subduction fault deepens the overriding plate margin. This concept of basal friction was extrapolated to subduction inter-plate friction and was shown to control upper plate state of stress and deformation, with elasto-plastic plates (Hassani et al., 1997; Buiter et al., 2001; Hampel and Pfiffner, 2006).

Sobolev et al. (2006) suggested that the fast and accelerating westward drift of the South American plate is the most important factor for controlling the intensity of shortening in the South American plate by using a coupled thermo-mechanical numerical model. Van Dinther et al. (2010) developed a viscoelastic 2D finite element model with dynamically interaction of the subducting plate, the overriding plate, and the mantle to analyse the role of the overriding plate on the subduction zone kinematics, morphology, and the stress state. They showed that the trenchward moving overriding plate enforces trench retreat by decreasing the slab dip. They also showed that the trenchward movement of the overriding plate stimulates its over thrusting onto the slab and permits mountain building within the overriding plate. Further, they suggest that frictional resistance only dragged down the overriding plate as it is increasing, thereby resist the growth of overriding plate topography. Present finding is also in good support to the previous studies and it implies the key role of the overriding plate in the topography generation.

Effect of slab pull

The combined effect of slab pull velocity and the gravity force create subsidence in the overriding plate for all coefficients of friction ($\mu = 0.1, 0.2, 0.5$) except coefficient of friction ($\mu = 0.0$). The model without friction ($\mu = 0.0$) generated a

small uplift region close to the trench up to a distance of approximately 20 km east of the trench as shown in Figure 4.9 (see section 4.2.3).

For the case of no friction ($\mu = 0.0$), the subsidence rate in the overriding plate was least and an increase in friction ($\mu = 0.1, 0.2, 0.5$) enhanced the subsidence rate of the overriding plate. Hampel and Pfiffner (2006) also showed that the slab pull only creates subsidence in the overriding plate even with the high coupling strength. Van Dinther et al. (2010) also found the same effect of the slab pull in combination with interface friction.

Effect of the thickness of continental crust

To study the effect of the thickness of the continental crust on the overriding plate deformation, the thickness of the continental crust was reduced to approximately 40 km. When keeping the same boundary conditions with reduced continental crustal thickness, a higher uplift was observed as compared to the model with a continental crustal thickness of 60 km (see section 4.2.4). It implies the relation between the overriding plate uplift and its thickness. There might be two factors for this: 1) the gravity force and 2) the rheological change.

There is a direct relationship between the gravitational acceleration and the downward weight force (F) experienced by the object (continental crust) and can be given by the equation 5.1

$$F = ma \quad (5.1)$$

where m is the mass of continental crust and a is the acceleration due to gravity taken as $a = g = 9.8 \text{ m/s}^2$ for both models. A decrease in the thickness of the continental crust implies decrease in its mass and thus implies decrease in the downward weight force experienced by the continental crust, which in turn produces more uplift in the thinner continental crust than the thick continental crust.

Decrease in the continental crustal thickness leads to an increase in the underlying mantle thickness. The Young's modulus describes the stiffness of the material and has inverse relation with material deformation. This implies less deformation below the lower continental crust, which might in turn produce higher uplift in the thinner continental crust as compared to the thicker continental crust.

The model with a thin continental crust and without friction ($\mu = 0.0$), showed an uplift rate of 0.9 mm/yr for the Altiplano plateau region. It is too high as compared to the geological uplift rate estimated by Gregory-Wodzicki (2000). However, the model with a thin continental crust and assuming the inter-plate friction coefficient between 0.3 and 0.35 (i.e. $0.3 < \mu < 0.35$) produced an uplift rate of 0.2 mm/yr, comparable to geological estimation for the Andean plateau region. This range of the friction coefficient is higher than the suggested range for friction coefficients by other authors (Cattin et al., 1997; Sobolev et al., 2006).

Combined effect of slab dip angle and gravity

To study the effect of slab dip angle, a model with the dip angle of $\beta = 13.4^\circ$ was designed in contrary to model II which had a dip angle of $\beta = 18.4^\circ$ and it was found that the uplift rate was lower with the dip angle of $\beta = 13.4^\circ$ as compared to the dip angle of $\beta = 18.4^\circ$ at point 200 km east of the trench (fore-arc region). But at point 400 km east of the trench (back-arc region), we have a higher uplift rate for the dip angle of $\beta = 13.4^\circ$ (Figure 5.2). Buiter et al. (2001) also found that a decrease (increase) in buoyancy of the subducting material leads to a deepening (uplift) of the plate margins. This implies that the deformation in the Southern Andes is more concentrated in the back-arc segment.

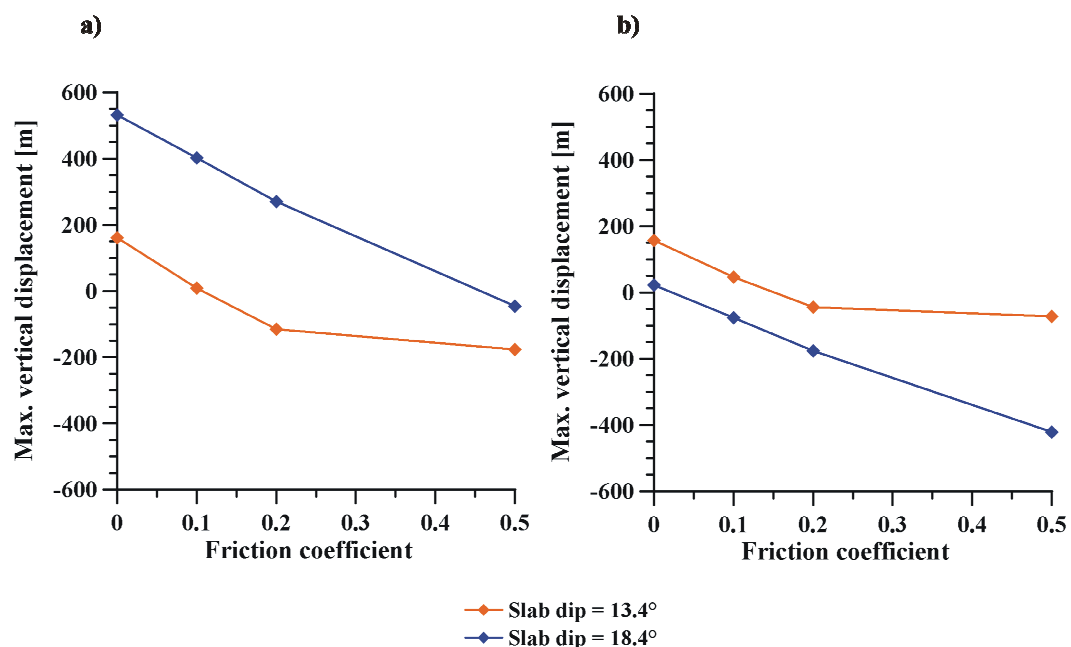


Figure 5.2. Comparison of maximum vertical displacement as a function of plate interface friction for different slab dip angles (β). a) At 200 km east of the trench. b) At 400 km east of the trench.

Another effect of the slab dip angle ($\beta = 18.4^\circ$) was also observed during the initial model run. A pattern of linear subsidence in the overriding plate was observed for the initial 25000 years irrespective of the plate interface coupling strength (Figure 5.3a). This linear subsidence pattern is more in the middle of the overriding plate. This implies the bending of the overriding plate in a concave upwards shape. Thereby is a sign of flexure in the overriding plate. In contrast, this effect is not present in the model with a shallow dip angle ($\beta = 13.4^\circ$) (Figure 5.3b). There is no pattern of subsidence during the initial time span of the subduction of the slab with dip angle of $\beta = 13.4^\circ$. It implies that slab with shallow dip provides sufficient support to the overriding plate and resists flexure in the overriding plate whereas, the slab with steep dip does not provide sufficient support to the overriding plate and the overriding plate subsidised under its own weight. This linear subsidence pattern was also observed in another study (using a slab dip angle of $\beta \sim 30^\circ$; Zeumann, 2013). It might be due to the combined effect of the slab dip angle and the gravity force.

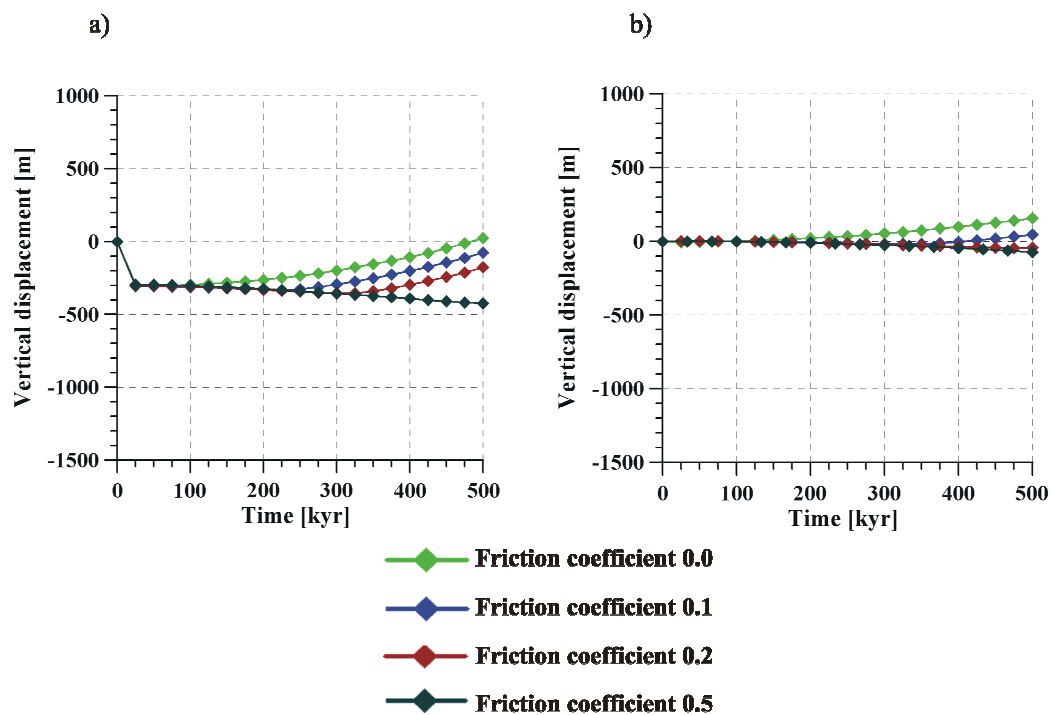


Figure 5.3. The deformation rate: a) Slab dip angle (β) = 18.4° . b) Slab dip angle (β) = 13.4° .

To check the role of gravity on the flexure, the reference model was run without gravity load and no flexure was observed in the overriding plate (Figure 5.4). Further, the uplift in the overriding plate starts developing from the beginning of

the time frame and produces uplift of over 3500 m in 500000 years (i.e. 7 mm/yr). It is very high as compared to the estimated uplift rate and it shows that the gravity also resists the uplift of the Andes.

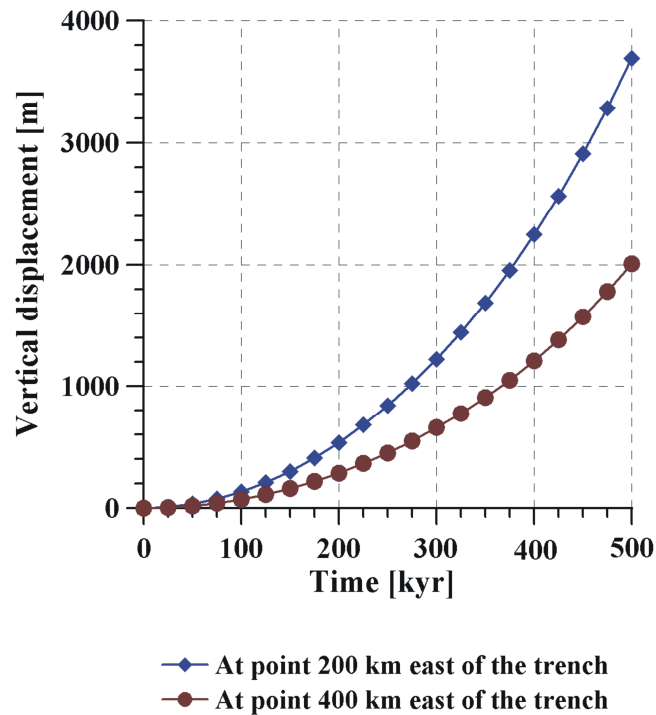


Figure 5.4. The deformation rate when gravity was ignored. The uplift rate is very high as compared to the geological estimated uplift rate for a point at 400 km east of the trench.

Comparison with GPS observations

The trench-normal velocity at point 400 km (1-2 mm/yr) east of the trench is also in agreement with the GPS derived trench-normal velocity (Figure 5.5; Hoffmann-Rothe et al., 2006).

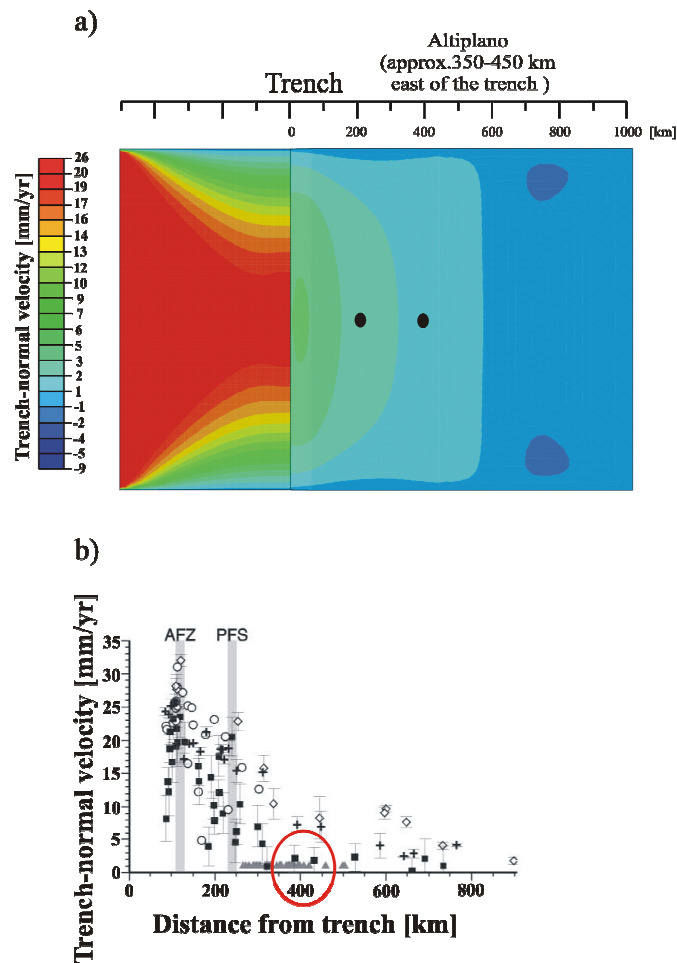


Figure 5.5. Comparison with observed GPS data. a) Trench normal component of velocity for reference model with coefficient of friction $\mu = 0.14$. b) Observed trench normal velocity for northern segment (20°S - 30°S) from various GPS data. Grey triangles at the bottom give the projected positions of volcanoes active in the Holocene. Grey vertical bars indicate the position of margin parallel strike-slip fault systems (after Hoffmann-Rothe et al., 2006). The red circle marks the velocity for the chosen point at 400 km east of the trench.

Thermo-mechanical model (Model IV)

The processes of the lithosphere (e.g. subduction) as well as of the asthenosphere are controlled by the heat derived from the Earth's interior. In the Earth heat moves by conduction, convection, advection, and radiation (Fowler, 2005). Conduction is the transfer of heat through a material by interaction within the material. In convection, heat transfer occurs through the molecules from one location to another within the material. Within the Earth, heat moves predominantly by conduction through the lithosphere (both oceanic and continental). In most of the mantle as well as through the liquid outer core, heat is generally thought to be transferred by convection. Advection is a special form of

convection, when a hot region is uplifted by the tectonic regime or by erosion and isostatic rebound, advected heat is physically lifted up with rocks. Radiation involves direct transfer of heat by electromagnetic radiation e.g. from Sun or an electric bar heater etc. (Fowler, 2005).

Fowler (2005) suggested a “plate model” for establishing the temperature distribution in the oceanic lithosphere and was used in the present study. In the plate model, the oceanic lithosphere is considered to have a constant depth. Temperature at the base of the oceanic lithosphere is considered to have the same constant value as the temperature at the vertical ridge axis. The top surface of the lithosphere is considered to have a temperature of 0° . The thermal parameters in the present study are taken from Fowler (2005).

A temperature of 1450°C at the base of oceanic lithosphere is assigned for establishing the temperature distribution in the Northern segment model. Top surface of the lithosphere is considered to have a temperature of 0°C (Fowler, 2005). In addition, at a depth of 105 km of the continental lithosphere the temperature of 1450°C was also applied. The density distribution in the continental mantle (CM) increases linearly with the depth. In addition to the thermal boundary conditions discussed above the applied mechanical boundary conditions for this model are the same as discussed in Table 4.2 (for Model II; see section 4.2.2).

Figure 5.6 shows that the density distribution of CM has strong influence on the deformation of the overriding plate. Model IV produces higher overriding plate uplift as compared to Model II (with constant density distribution in CM). The trend of decreasing uplift with increase in the coefficient of friction in Model IV is also not sharp like in Model II. It seems that the density distribution of CM affects the coupling strength of the frictionally coupled zone. Increase in the density of CM with depth decreases the downward drag of the subducting plate which in turn, creates higher overriding plate uplift in Model IV than Model II.

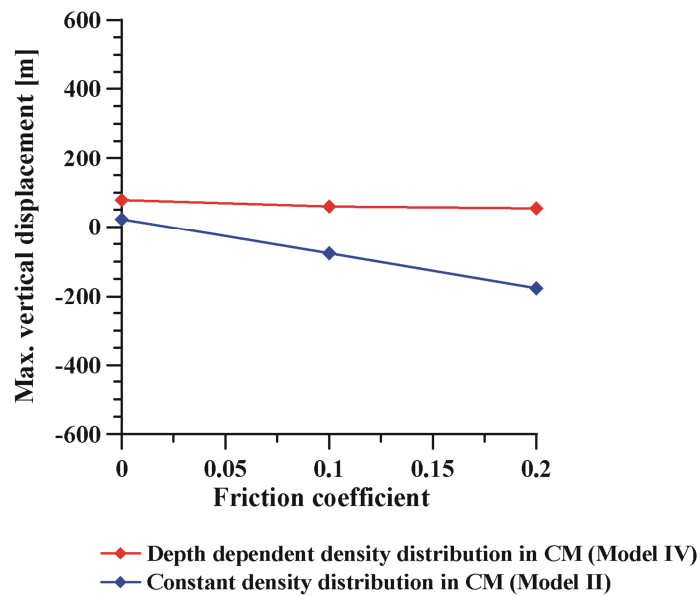


Figure 5.6 Comparison of maximum vertical displacement as a function of inter-plate friction coefficients.

The main results and conclusion from this study can be summarised as:

- The coefficient of friction ($\mu = 0.14$) at the frictionally coupled zone causes approximately 103 m of uplift in 500000 years at the Altiplano plateau region, which is in good agreement with the geological estimated uplift rate of 0.2 mm/yr (Gregory-Wodzicki, 2000) for the Altiplano plateau in the Central Andes. The value is also in a good agreement with the estimation of Cattin et al. (1997).
- The inverse relationship between the strength of the frictionally coupled zone and the overriding plate uplift was observed. This relation is also observed by Van Dinther et al. (2010).
- When the subduction takes place with only slab pull velocity, no uplift was generated, not even with a high coefficient of friction at the frictionally coupled zone. Increase in the coupling strength of frictionally coupled zone increases the downward drag of the subducting plate and leads to increase in overriding plate subsidence. This effect of slab pull was also observed by Hampel and Pfiffner (2006). It implies that the hypothesis relating the high overriding plate topography with the high value of inter plate friction does not hold good in every condition.
- The thickness of the continental crust also has influence on the continental uplift and is inversely related to its uplift. Decrease in the thickness of the

overriding plate implies increase in its uplift. The model with thin continental crust (40 km) and the inter plate coefficient of friction between 0.3 and 0.35 (i.e. $0.3 < \mu < 0.35$) produces geological estimated uplift rate of 0.2 mm/yr for the Altiplano plateau.

- The overriding plate uplift is generated when the trenchward overriding plate moves with the rate ≥ 2 cm/yr. Trenchward movement of overriding plate with the rate ≤ 2 cm/yr fails to generate uplift in it. This trend was also observed in the subduction modelling of Hampel and Pfiffner (2006) and Van Dinther et al. (2010).
- The obliquely subducting plate with an obliquity ($\gamma = 20^\circ$) creates subsidence in the overriding plate for all coefficients of friction ($\mu = 0.0, 0.1, 0.2, 0.5$).
- The dip of the subducting slab plays an important role in controlling the overriding plate deformation. The uplift in the fore-arc region is lower in the Southern segment model ($\beta = 13.4^\circ$) than in the Northern segment model ($\beta = 18.4^\circ$). In contrast the uplift in the back-arc region is higher in the Southern segment model as compared to the Northern segment model.
- Increase in density with depth in the Continental mantle intensifies the overriding plate uplift by reducing the downward drag of the subducting plate and creates higher overriding plate uplift.

The present study shows that the boundary conditions and the physical parameters (thickness of the continental crust, continental drift velocity, convergence obliquity, and dip of subducting slab) regulate the mechanics of the frictionally coupled zone and in turn, the overriding plate deformation. The Southern Andean model with a shallower dip angle ($\beta = 13.4^\circ$) produces lower uplift in the fore-arc region but higher uplift in the back-arc region as compared to the Northern Andean model having a steep slab dip angle ($\beta = 18.4^\circ$). The difference in the geometry of slab can be one possible reason for the differences between the topography of the Northern and the Southern Andes.

In conclusion, the trenchward movement of the overriding plate is the parameter that creates high topography of the Andes on the South American continental plate, while the strength of frictionally coupled zone, slab dip, and the thickness of the overriding plate are the parameters that quantify its topography.

Hence, the findings of this study will be helpful in further understanding of the complexity of geodynamic processes of the South American subduction zone based on realistic geometry as well as for the general subduction zone related investigations. The physical parameters such as thickness of the continental crust and the slab dip have strong influence on the overriding plate deformation. These constraints should be derived in the most realistic sense by using a multidisciplinary integrative approach using geological observations and geophysical studies in order to further increase the understanding of the complex processes of subduction zone by geodynamic modelling.

Bibliography

Abaqus Analysis User's Manual (2010), version 6.10, Dassault Systèmes Simulia Corp., Providence, RI, USA, <http://www.sharenet.ca/Software/Abaqus610/Documentation/docs/v6.10/books/usb/default.htm>.

Allmendinger, R. W. and T. Gubbels (1996), Pure and simple shear plateau uplift, Altiplano-Puna, Argentina and Bolivia, *Tectonophysics*, 259, 1–14.

Allmendinger, R. W., T. E. Jordan, S. M. Kay, and B. L. Isacks (1997), The evolution of the Altiplano-Puna plateau of the central Andes, *Annu. Rev. Earth Planet. Sci.*, 25, 139–174.

ANCORP Working Group (1999), Seismic reflection image revealing offset of Andean subduction-zone earthquake locations into oceanic mantle, *Nature*, 397, 341-344.

ANCORP Working Group (2003), Seismic imaging of a convergent continental margin and plateau in the central Andes (Andean Continental Research Project 1996 (ANCORP'96)), *J. Geophys. Res.*, 108 (B7), 2328, doi: 10.1029/2002JB001771.

Babeyko, A. Y., and S. V. Sobolev (2008), High-resolution numerical modeling of stress distribution in visco-elasto-plastic subducting slabs, *Lithos*, 103, 205-216, doi:10.1016/j.lithos.2007.09.015.

Baby, P., T. Sempere, J. Oller, and G. Hérail (1992a), Evidence for major shortening on the eastern edge of the Bolivian Altiplano: The Calazaya nappe, *Tectonophysics*, 205, 155-169.

Bangs, N. L., and S. C. Cande (1997), Episodic development of a convergent margin inferred from structures and processes along the southern Chile margin, *Tectonics*, 16(3), 489–503.

Barazangi, M., and B. L. Isacks (1976), Spatial distribution of earthquakes and subduction of the nazca plate beneath South America, *Geology*, 4(11), 686-692.

Bohm, M., S. Lüth, H. Echtler, G. Asch, K. Bataille, C. Bruhn, A. Rietbrock, P. Wigger (2002), The Southern Andes between 36° and 40°S latitude: seismicity and average seismic velocities, *Tectonophysics*, 356, 275–289.

Bonnardot, M.-A., R. Hassani, E. Tric, E. Ruellan, and M. Régnier (2008), Effect of margin curvature on plate deformation in a 3-D numerical model of subduction zones, *Geophys. J. Int.*, 173, 1084-1094, doi:10.1111/j.1365-246X.2008.03752.

Bott, M. H. P., G. D. Waghorn and A. Whittaker (1989), Plate boundary forces at subduction zones and trench-arc compression, *Tectonophysics*, 170, 1-15.

Brasse, H. and W. Soyer (2001), A magnetotelluric study in the Southern Chilean Andes, *Geophys. Res. Lett.*, 28(19), 3757-3760.

Broccoli, A. J., and S. Manabe (1997), Mountains and mid latitude aridity, In: Tectonic Uplift and Climate Change, New York, *Plenum Press*, 89-121.

Brooks, B. A., M. Bevis, R. Jr. Smalley, E. Kendrick, R. Manceda, E. Lauria, R. Manturana, M. Araujo (2003), Crustal motion in the Southern Andes (26°–36°S): do the Andes behave like a microplate?, *Geochem. Geophys. Geosyst.*, 4(10), doi 10.1029/2003GC000505.

Buiter, S. J. H., R. Govers, and M. J. R. Wortel (2001), A modelling study of vertical surface displacements at convergent plate margins, *Geophys. J. Int.*, 147, 415–427.

Byerlee, J. (1978), Friction of rocks, *Pure and Applied Geophys.*, 116, 615–626, doi:10.1007/BF00876528.

Cahill, T. A., and B. L. Isacks (1992), Seismicity and shape of the subducted Nazca Plate, *J. Geophys. Res.*, 97(12), 17503–17529.

Campetella, C. M., and C. S. Vera (2002), The influence of the Andes mountains on the South American low-level flow, *Geophys. Res. Lett.*, 29(17), doi 10.1029/2002GL01545.

Cattin, R., H. Lyon-Caen, and J. Chery (1997), Quantification of interplate coupling in subduction zones and forearc topography, *Geophys. Res. Lett.*, 24 (13), 1563–1566.

Cembrano, J., F. Hervé, A. Lavenu (1996), The Liquine Ofqui fault zone: a long-lived intra-arc fault system in southern Chile, In: *Geodynamics of the Andes*, 259, 1–3, *Elsevier*, Amsterdam, 55–66.

Cembrano, J., G. González, G. Arancibia, I. Ahumada, V. Olivares, V. Herrera (2005), Fault zone development and strain partitioning in an extensional strike-slip duplex: a case study from the Mesozoic Atacama fault system, Northern Chile, *Tectonophysics*, 400, 105–125.

Chen, W.-F., and D. J. Han (2007), *Plasticity for Structural Engineers*, *J. Ross Publishing*, 606 pp.

Christensen, U. R., and A. W. Hofmann (1994), Segregation of subducted oceanic crust in the convecting mantle, *J. Geophys. Res.*, 99(B10), 19867–19884, doi:10.1029/93JB03403.

Conard, C. P., S. Bilek, and C. Lithgow-Bertelloni (2004), Great earthquakes and slab pull: interaction between seismic coupling and plate-slab coupling, *Earth Planet. Sci. Lett.*, 218, 109–122, doi: 10.1016/S0012-821X(03)00643-5.

Davidson, J. and R. Arculus (2006), The significance of Phanerozoic arc magmatism in generating continental crust, In: Brown, M. and Rushmer, T. (ed.), *Evolution and Differentiation of the Continental Crust*, *Cambridge University Press*, United Kingdom, 135–172.

Defant, M. J. (1998), *Voyage of Discovery: From the Big Bang to the Ice Age*. *Mancorp.*, 325. ISBN 0-931541-61-1.

Dewey, J. F. and S. H. Lamb (1992), Active tectonics of the Andes, *Tectonophysics*, 205, 79–95.

Dewey, J. F., and J. M. Bird (1970), Mountain belts and the new global tectonics, *J. Geophys. Res.*, 75(14), 2625–2647, doi:10.1029/JB075i014p02625.

Ellis, S., J. Beavan, D. Eberhart-Phillips, B. Stockhert (2006), Simplified models of the Alpine fault seismic cycle: stress transfer in the mid-crust, *Geophys. J. Int.*, 166, 386–402.

Farías, M., G. Vargas, A. Tasara, S. Carretier, S. Baize, D. Melnick, K. Bataille (2010), Land-level changes produced by the Mw 8.8 2010 Chilean earthquake, *Science (Brevia)*, 329, 916, doi: 10.1126/science.1192094, 2010.

Folguera, A., V. Ramos, D. Melnick (2002), Partición de la deformación en la zona del arco volcánico de los Andes neuquinos (36–39°S) en los últimos 30 millones de años, *Rev Geol Chile*, 29(2), 151–165.

Forsyth, D., and S. Uyeda (1975), On the Relative Importance of the Driving Forces of Plate Motion, *Geophys. J. R. astr. Soc.*, 43, 163-200.

Fowler, C. M. R. (2005), *The Solid Earth: An introduction to global geophysics*, Cambridge University press, Cambridge UK.

Gassmöller, R. (2011), Spannungs- und Deformationsverteilung an gebogenen Subduktionszonen, Diploma thesis, Friedrich-Schiller-Universität Jena (unpublished).

Gephart, J. W. (1994), Topography and subduction geometry in the central Andes: Clues to the mechanics of a noncollisional orogen, *J. Geophys. Res.*, 99(B6), 12279–12288,

Gerbault, M., J. Cembrano, C. Mpodozis, M. Farias, and M. Pardo (2009), Continental margin deformation along the andean subduction zone: Thermo-mechanical models, *Physics of the Earth and Planet. Int.*, 177(3-4), 180-205.

Gibert, G., M. Gerbault, R. Hassani and E. Tric (2012), Dependency of slab geometry on absolute velocities and conditions for cyclicity: insights from numerical modelling. *Geophys. J. Int.*, 189: 747–760.

Giese P., E. Scheuber, F. Schilling, M. Schmitz, P. Wigger (1999), Crustal thickening processes in the central Andes and the different nature of the Moho discontinuity, *J. S. Am. Earth Sci.*, 12, pp. 201–210.

González G., J. Cembrano, D. Carrizo, A. Macci, H. Schneider (2003), Link between forearc tectonics and Pliocene-Quaternary deformation of the Coastal Cordillera, Northern Chile, *J. S. Am. Earth Sci.*, 16, 321–342.

Gregory-Wodzicki, K. M. (2000), Uplift history of the Central and Northern Andes: A review, *Geol. Soc. Am. Bull.*, 112 (7), 1091-1105, doi:10.1130/0016-7606(2000)112.

Gutscher M., W. Spakman, H. Bijwaard, E. Engdahl (2000), Geodynamics of flat subduction: seismicity and tomographic constraints from the Andean margin, *Tectonics*, 19, 814–833.

Gutscher, M.-A., W. Spakman, H. Bijwaard, and E. R. Engdahl (2000), Geodynamics of flat subduction: Seismicity and tomographic constraints from the Andean margin, *Tectonics*, 19 (5), 814-833, doi:10.1029/1999TC001152.

Hampel, A., and A. Pfiffner (2006), Relative importance of trenchward upper plate motion and friction along the plate interface for the topographic evolution of subduction-related mountain belts, In: Buiter, S. J. H. and Schreurs, G. (eds.) *Analogue and Numerical Modelling of Crustal-Scale processes*, *Geol. Soc., London*, Special Publication, 253, 105-115.

Hassani, R., D. Jongmans, and J. Chéry (1997), Study of plate deformation and stress in subduction processes using two-dimensional numerical models, *J. Geophys. Res.*, 102(B8), 17951–17965.

Hergert, T., and O. Heidbach (2006), New insights into the mechanism of postseismic stress relaxation exemplified by the 23 June 2001 $M_w=8.4$ earthquake in southern Peru, *Geophys. Res. Lett.*, 33, doi: 10.1029/2005GL024858. issn: 0094-8276.

Hervé, M. (1976), Estudio geológico de la falla Liquiñe-Reloncaví en la área de Liquiñe: antecedentes de un movimiento transcurrente (Provincia de Valdivia), *Actas I Congreso Geológico Chileno*, B, 39–56.

Hetzl, R., and A. Hampel (2005), Slip rate variations on normal faults during glacial–interglacial changes in surface loads, *Nature*, 435, 81–84.

Heuret, A., F. Funiciello, C. Faccenna, and S. Lallemand (2007), Plate kinematics, slab shape and back-arc stress: A comparison between laboratory models and current subduction zones, *Earth Planet. Sci. Lett.*, 256, 473-483.

Hildreth, W., and S. Moorbath (1988), Crustal contributions to arc magmatism in the Andes of Central Chile, *Contrib. Miner. Petrol.*, 98, 455-489.

Hoffmann-Rothe, A., N. Kukowski, G. Dresen, H. Echtler, O. Oncken, J. Klotz, E. Scheuber, and A. Kellner (2006), Oblique Convergence along the Chilean Margin: Partitioning, Margin-Parallel Faulting and Force Interaction at the Plate Interface, In: Oncken, O., Chong, G., Franz, G., Giese, P., Götze, H.-J., Ramos, V. A., Strecker, M. and Wigger, P. (eds.) The Andes: Active subduction orogeny, *Frontiers in Earth Science Series*, 125-146.

Hofmann, A. W. (1997), Mantle geochemistry: the message from oceanic volcanism, *Nature*, 385, 219-29.

Iaffaldano, G., H.-P. Bunge, and T. H. Dixon (2006), Feedback between mountain belt growth and plate convergence, *Geology*, 34, 893-896, doi: 10.1130/G22661.1.

Isacks, B. L. (1988), Uplift of the Central Andean Plateau and bending of the Bolivian orocline, *J. Geophys. Res.*, 93 (B4), 3211-3231.

Isacks, B., J. Oliver and L. R. Sykes (1968), Seismology and the new global tectonics, *J. Geophys. Res.*, 73, 5855-99.

Jarrard, R. D. (1986), Relations among subduction parameters, *Rev. Geophys.*, 24, 217-284.

Jordan, T. E., W. M. Burns, R. Veiga, F. Pángaro, P. Copeland, S. Kelley, C. Mpodozis (2001), Extension and basin formation in the southern Andes caused by increased convergence rate: a mid-Cenozoic trigger for the Andes, *Tectonics*, 20(3), 308-324.

Jordan, T. E., B. L. Isacks, R. W. Allmendinger, J. A. Brewer, V. A. Ramos, C. J. Ando (1983), Andean tectonics related to geometry of subducted Nazca plate, *Geol. Stud. Am. Bull.*, 94, 341-361.

Kanamori, H. (1986), Rupture process of subduction zone earthquakes, *Annu. Rev. Earth Planet. Sci.*, 14, 293–322, doi: 10.1146/annurev.ea.14.050186.001453.

Kearey, P., K. A. Klepeis, J. V. Frederick (2008), *Global tectonics*, 3rd edition, Wiley-Blackwell publishing.

Kellner, A. (2007), Different styles of deformation of the fore-arc wedge along the Chilean convergent margin: Insights from 3D numerical experiments, Ph.D. thesis, Universität Potsdam.

Kelly, P. A. (2012), Lecture Notes in Solid Mechanics Part II: Engineering Solid Mechanics, http://homepages.engineering.auckland.ac.nz/~pkel015/SolidMechanicsBooks/Part_II/08_Plasticity/08_Plasticity_03_YieldCriteria.pdf

Kendrick, E., M. G. Bevis, R. Smalley, and B. A. Brooks (2001), An integrated crustal velocity field for the central Andes, *Geochem. Geophys. Geosyst.*, 2, doi: 10.1029/2001GC000191.

Kirchner, A., H.-J. Götze, and M. Schmitz (1996), 3D-density modelling with seismic constraints in the Central Andes, *Physics and Chemistry of The Earth*, 21 (4), 289-293, doi:10.1016/S0079-1946(97)00050-5.

Kley, J. and C. R. Monaldi (1998), Tectonic shortening and crustal thickening in the Central Andes: how good is the correlation?, *Geology*, 26-8, 723–726.

Kley, J., C. R. Monaldi, J. A. Salfity (1999), Along-strike segmentation of the Andean foreland: causes and consequences, *Tectonophysics*, 301, 75–94.

Klotz, J., A. Abolghasem, G. Khazaradze, B. Heinze, T. Vietor, R. Hackney, K. Bataille, R. Maturana, J. Viramonte, R. Perdomo (2006), Long-term signals in the present-day deformation field of the Central and Southern Andes and constraints on the viscosity of the Earth's upper mantle, In: Oncken O, Chong G, Franz G, Giese P, Götze H-J, Ramos VA, Strecker MR, Wigger P (eds) *The Andes – active subduction orogeny*, *Frontiers in Earth Science Series*, 1, *Springer-Verlag, Berlin Heidelberg New York*, 65–90.

Klotz, J., G. Khazaradze, D. Angermann, C. Reigber, R. Perdomo, O. Cifuentes (2001), Earthquake cycle dominates contemporary crustal deformation in Central and Southern Andes, *Earth Planet. Sci. Lett.*, 193(3–4), 437–446.

Klotz, J., G. Michel, G. Khazaradze, B. Heinze (2001), GPS based Deformation Measurements and Modeling, *Report of SFB 267*, project D5, 361 - 394.

Kösters, M. (1998), 3D-Dichtemodellierung des Kontinentalrandes sowie quantitative Untersuchungen zur Isostasie und Rigidität der Zentralen Anden (20°-26°S), Ph.D. thesis, Berliner geowissenschaftliche Abhandlungen: Reihe B, Geophysik, 32, Freie Universität Berlin.

Köther, N., H.-J. Götze, B. D. Gutknecht, T. Jahr, G. Jentzsch, O. H. Lücke, R. Mahatsente, R. Sharma, S. Zeumann (2012), The seismically active Andean and Central American margins: Can satellite gravity map lithospheric structures?, *Journal of Geodynamics*, 59-60, 207-218, doi:10.1016/j.jog.2011.11.004.

Lallemand, S., A. Heuret, and D. Boutelier (2005), On the relationships between slab dip, back-arc stress, upper plate absolute motion, and crustal nature in subduction zones, *Geochem. Geophys. Geosyst.*, 6, Q09006, doi:10.1029/2005GC000917.

Lamb, S., and P. Davis (2003), Cenozoic climate change as a possible cause for the rise of the Andes, *Nature*, 425 (6960), 792-797, doi:10.1038/nature02049.

Lamb, S., L. Hooke (1997), Origin of the high plateau in the central Andes, Bolivia, South America, *Tectonics*, 16, 623–649.

Lamb, S., L. Hoke, L. Kennan, J. Dewey (1997), Cenozoic evolution of the Central Andes in Bolivia and Northern Chile. In: Burg JP, Ford M (eds), Orogeny through time, *Geol. Soc. Spec. Publ.*, 121, 237–264.

Lavenu, A., J. Cembrano (1999), Compressional and transpressional-stress pattern for Pliocene and quaternary brittle deformation in fore arc and intra-arc zones (Andes of central and southern Chile), *J. Struct. Geol.*, 21, 1669–1691.

Lay, T., and S. Y. Schwartz (2004). Comment on Coupling semantics and science in earthquake research, *EOS*, 85 (36), 339-340.

Leffler, L., S. Stein, A. Mao, T. Dixon, M.A. Ellis, L. Ocola, and I. S. Sacks (1997), Constraints on present-day shortening rate across the central eastern Andes from GPS data, *Geophys. Res. Lett.*, 24, 1031-1034.

Liu, M., Y. Yang, S. Stein, and E. Klosko (2002), Crustal Shortening and Extension in the Central Andes: Insights from a Viscoelastic Model, In: Stein, S., and J. T. Freymueller (eds.) *Plate Boundary Zones, AGU Geodyn. Ser.*, 30, 325-339, doi:10.1029/030GD19.

López-Escobar, L. (1984), Petrology and chemistry of volcanic rocks of the southern Andes, In: Harmon RS, Barreiro BA (eds) *Andean Magmatism, chemical and isotopic constraints, Shiva Publ. Co., Cheshire UK*, 47–71.

Lucassen, F., R. Trumbull, G. Franz, C. Creixell, P. Vásquez, R. L. Romer, O. Figueroa (2004), Distinguishing crustal recycling and juvenile additions at active continental margins: the Paleozoic to Recent compositional evolution of the Chilean Pacific margin (36–41°S), *J. S. Am. Earth Sci.*, 17, 103–119.

Lüth, S., P. Wigger, ISSA Research Group (2003), A crustal model along 39°S from a seismic refraction profile–ISSA (2000), *Rev. Geol Chile*, 30(1), 83–101.

Mamani, M., A. Tassara, and G. Wörner (2008), Composition and structural control of crustal domains in the central Andes, *Geochem. Geophys. Geosyst.*, 9, doi:10.1029/2007GC001925.

McCaffrey, R. (1994), Global variability in subduction thrust zone - forearc systems, *Pure & Applied Geophysics*, 142(1), 173-224.

Melnick, D., B. Bookhagen, M. Strecker, and H. Echtler (2009), Segmentation of megathrust rupture zones from forearc deformation patterns over hundreds to millions of years, Arauco Peninsula, Chile, *J. Geophys. Res.*, 114, B01407, doi:10.1029/2008JB005788.

Mpodozis, C. and V. A. Ramos (1989), The Andes of Chile and Argentina, In: G. G. Ericksen, M. M. Cañas Pinochet, J. Reinemund (Eds.), *Geology of the Andes and its Relation to Hydrocarbon and Mineral Resources, Earth Science Series, Circum-Pacific Council of Energy and Mineral Resources, Houston, TX*, 59–89.

Muñoz, J., R. Troncoso, P. Duhart, P. Cringnola, L. Farmer, C. R. Stern (2000), The relation of the mid-Tertiary coastal magmatic belt in South-Central Chile to the late Oligocene increase in plate convergence rate, *Rev. Geol. Chile*, 27(2), 177–203.

Norabuena, E. O., T. H. Dixon, S. Stein, and C. G. A. Harrison (1999), Decelerating Nazca-South America and Nazca-Pacific plate motions, *Geophys. Res. Lett.*, 26, 3405-3408.

Norabuena, E. O., L. Leffler-Griffin, A. Mao, T. Dixon, S. Stein, I.S. Sacks, L. Ocola, and M. Ellis (1998), Space geodetic observations of Nazca–South America convergence across the Central Andes, *Science*, 279, 358–362, doi: 10.1126/science.279.5349.358.

O' Brien, P. J. (2001), Subduction followed by collision: Alpine and Himalayan examples, *Phys. Earth Planet. Inter.*, 127, 277-291.

Oleskevich, D.A., R. D. Hyndman, K. Wang (1999), The updip and downdip limits to great subduction earthquakes: thermal and structural models of Cascadia, South Alaska, SW Japan, and Chile, *J. Geophys. Res.*, 104, 14965-14991.

Oncken, O., D. Hindle, J. Kley, K. Elger, P. Victor, and K. Schemman (2006), Deformation of the Central Andean Upper Plate System - Facts, Fiction, and Constraints for Plateau Models, In: Oncken, O., Chong, G., Franz, G., Giese, P., Götze, H.-J., Ramos, V. A., Strecker, M. and Wigger, P. (eds.) The Andes – active subduction orogeny, *Frontiers in Earth Science Series*, 1, *Springer-Verlag, Berlin Heidelberg New York*, 3-27.

Pacheco, J. F., Sykes, L. R. and Scholz, C. H. (1993), Nature of seismic coupling along simple plate boundaries of the subduction type, *J. Geophys. Res.*, 98, 14133-14139, doi: 10.1029/93JB00349.

Pankhurst, R. J., S. D. Weaver, F. Hervé, P. Larrondo (1999), Mesozoic–Cenozoic evolution of the North Patagonian Batholith in Aysén, southern Chile, *J. Geol. Soc.*, 156, 673–694.

Pardo-Casas, F. and P. Molnar (1987), Relative motion of the Nazca (Farallon) and South American plates since Late Cretaceous time, *Tectonics*, 6, 233-48.

Peacock, S. M. (1996), Thermal and Petrologic Structure of Subduction Zones, In: Bebout, G. E., Scholl, D. W., Kirby, S. H., and Platt, J. P. (eds.), Subduction: Top to Bottom, Geophysical Monograph 96, *American Geophysical Union*, Washington, D.C., 119-134.

Pérez-Gussinyé, M., A. R. Lowry, J. Phipps Morgan, and A. Tassara (2008), Effective elastic thickness along the Andean margin and their relationship to subduction geometry, *Geochem. Geophys. Geosyst.*, doi:10.1029/2007GC001786.

Pineda, V. (1986), Evolución paleogeográfica de la cuenca sedimentaria Cretácico-Terciaria de Arauco, In: Frutos, J., Oyarzún, R., Pincheira, M. (eds), Geología y Recursos Minerales de Chile, Tomo 1, *Universidad de Concepción*, 375–390.

Prezzi, C. B., H.-J. Götze, and S. Schmidt (2009), 3D density model of the Central Andes, *Phys. Earth Planet. In.*, 177, 217-234, doi:10.1016/j.pepi.2009.09.004.

Ranalli, G. (1995), Rheology of the Earth, *Chapman and Hall*, London, 413 p.

Raymo, M. E., and W. F. Ruddiman (1992), Tectonic forcing of the late Cenozoic climate, *Nature*, 359, 117– 122.

Reutter, K.-J., E. Scheuber, D. Helmcke (1991), Structural evidence of orogen-parallel strike slip displacements in the Precordillera of northern Chile, *Geologische Rundschau, Int. J. Earth Sci.*, 80, 135–153.

Reutter, K.-J., E. Scheuber, G. Chong (1996), The Precordilleran fault system of Chuquicamata, Northern Chile: evidence for reversals along arc-parallel strike-slip faults, *Tectonophysics*, 259, 213–228.

Riquelme, R., J. Martinod, G. Hérail, J. Darrozes, R. Charrier (2003), A geomorphological approach to determining the Neogene to Recent tectonic deformation in the Coastal Cordillera of northern Chile (Atacama), *Tectonophysics*, 361, 255–275.

Ruddiman, W. F., and J. E. Kutzbach (1989), Forcing of late Cenozoic northern hemisphere climate by plateau uplift in southern Asia and the American west, *J. Geophys. Res.*, 94(D15), 18409–18427, doi:10.1029/JD094iD15p18409.

Ruff, L. J. (1989), Do trench sediments affect great earthquake occurrence in subduction zones?, *Pure and Applied Geophysics*, 129, 263-282.

Ruff, L., and H. Kanamori (1983), Seismic coupling and uncoupling at subduction zones, *Tectonophysics*, 99, 99-117.

Russo, R., and P. Silver (1996), Cordillera formation, mantle dynamics, and the Wilson Cycle, *Geology*, 24, 511–514.

Schellart, W.P., J. Freeman, D. R. Stegman, L. Moresi, D. May (2007), Evolution and diversity of subduction zones controlled by slab width, *Nature*, 446, 308–311.

Scheuber, E. and G. González (1999), Tectonics of the Jurassic-early Cretaceous magmatic arc of the north Chilean Coastal Cordillera (22–26°S): a story of coupling and decoupling in the subduction zone, *Tectonics*, 18 (5), 895–910.

Schmitz, M., (1994), A balanced model of the southern Central Andes, *Tectonics*, 13, 484-492.

Scholz, C. H. (1990), The mechanics of earthquakes and faulting, *Cambridge University Press*, Cambridge U K.

Scholz, C. H., and J. Campos (1995), On the mechanism of seismic decoupling and back arc spreading at subduction zones, *J. Geophys. Res.*, 100(B11), 22103–22115, doi:10.1029/95JB01869.

Scholz, C.H. (1998), Earthquakes and friction laws, *Nature*, 391, 37-42, doi:10.1038/34097.

Sheffels, B., (1990), Lower bound on the amount of crustal shortening in the central Bolivian Andes, *Geology*, 18, 812-815.

Shemenda, A. I. (1993), Subduction of the lithosphere and back arc dynamics: Insights from physical modeling, *J. Geophys. Res.*, 98(B9), 16167–16185.

Silver, P. G., R. M. Russo, and C. Lithgow-Bertelloni (1998), Coupling of South American and African plate motion and plate deformation, *Science*, 279 (5347), 60-63, doi:10.1126/science.279.5347.60.

Sobolev S.V., Babeyko A.Y., Koulakov I., Oncken O., 2006. Mechanism of the Andean Orogeny: Insight from Numerical Modeling, In: Oncken, O., Chong, G., Franz, G., Giese, P., Götze, H.-J., Ramos, V. A., Strecker, M. and Wigger, P. (eds.) *The Andes – active subduction orogeny*, *Frontiers in Earth Science Series*, 1, *Springer-Verlag, Berlin Heidelberg New York*, 513-535.

Sobolev, S. V., and A. Y. Babeyko (2005), What drives orogeny in the Andes?, *Geology*, 33(8), 617–620.

Somoza, R. (1998), Updated Nazca (Farallon)–South America relative motions during the last 40 My: implications for mountain building in the central Andean region, *J. S AM. Earth Sci.* 11, 211–215.

Stein, C. A., and S. Stein (1992), A model for the global variation in oceanic depth and heat flow with lithospheric age, *Nature*, 359, 123-129, doi:10.1038/359123a0.

Stern, R. J. (2002), Subduction zones, *Rev. Geophys.*, 40 (4), 1012, doi:10.1029/2001RG000108.

Strunk, S. (1990), Analyse und Interpretation des Schwerefeldes des aktiven Kontinentalrandes der zentralen Anden (20–26°S), Ph.D. thesis, *Berliner geowissenschaftliche Abhandlungen : Reihe B, Geophysik ; Bd. 17*, Freie Universität Berlin.

Suarez, G., P. Molnar, and B. C. Burchfiel (1983), Seismicity, fault plane solutions, depth of faulting, and active tectonics of the Andes of Peru, Ecuador, and southern Colombia, *J. Geophys. Res.*, 88, 10403-10428.

Tašárová, Z. A. (2007), Towards understanding the lithospheric structure of the southern Chilean subduction zone (36°S–42°S) and its role in the gravity field, *Geophys. J. Int.*, 170 (3), 995-1014, doi:10.1111/j.1365-246X.2007.03466.x.

Tassara, A. (2005), Interaction between the Nazca and South American plates and formation of the Altiplano–Puna plateau: review of a flexural analysis along the Andean margin (15–34°S), *Tectonophysics*, 399, 39–57.

Tassara, A. and A. Echaurren (2012), Anatomy of the Andean subduction zone: three-dimensional density model upgraded and compared against global-scale models, *Geophysical Journal International*, 189, 161–168, doi: 10.1111/j.1365246X.2012.05397.x

Tassara, A., H.-J. Götze, S. Schmidt, and R. Hackney (2006), Three-dimensional density model of the Nazca plate and the Andean continental margin, *J. Geophys. Res.*, 111, B09404, doi:10.1029/2005JB003976.

Tichelaar, B. W., and L. J. Ruff (1991), Seismic coupling along the Chilean Subduction Zone, *J. Geophys. Res.*, 96(B7), 11997–12022, doi:10.1029/91JB00200.

Tichelaar, B. W., and L. J. Ruff (1993), Depth of seismic coupling along subduction zones, *J. Geophys. Res.*, 98(B2), 2017–2037, doi:10.1029/92JB02045.

Uyeda, S., and H. Kanamori (1979), Back-arc opening and the mode of subduction, *J. Geophys. Res.*, 84, 1049–1061.

van Dinther, Y., G. Morra, F. Funiciello, and C. Faccena (2010), Role of the overriding plate in the subduction process: insights from numerical models, *Tectonophysics*, 484 (1–4), 74–86.

Vietor, T., and H. Echtler (2006), Episodic Neogene southward growth of the Andean subduction orogen between 30°S and 40°S - plate motions, mantle flow, climate, and upper-plate structure, In: Oncken O, Chong G, Franz G, Giese P, Götze H-J, Ramos VA, Strecker MR, Wigger P (eds), *The Andes – active subduction orogeny*, *Frontiers in Earth Science Series*, 1, Springer-Verlag, Berlin Heidelberg New York, 375–400.

Wang, K, J. He (1999), Mechanics of low-stress fore-arcs: Nankai and Cascadia. *J. Geophys. Res.*, 104(B7):15191–15205.

Wang, K., and K. Suyehiro (1999), How does plate coupling affect stresses in northeast and southwest Japan?, *Geophys. Res. Lett.*, 26, doi: 10.1029/1999GL900528. issn: 0094-8276.

Willett, S., Beaumont, C., and Fullsack, P. (1993), Mechanical model for the tectonics of doubly vergent compressional orogens, *Geology*, 21, 371–374.

Yáñez G., and J. Cembrano (2004), Role of viscous plate coupling in the late Tertiary Andean tectonics, *J. Geophys. Res.*, 109, B02407, doi: 10.1029/2003JB002494.

Zeumann, S. (2013), 3D Finite Element Modelling of the Central Andean subduction zone with realistic geometry, Ph.D thesis, Friedrich-Schiller-Universität Jena.

Zeumann, S., R. Sharma, R. Gassmöller, T. Jahr, G. Jentzsch (2013), New Finite-Element modelling of subduction processes in the Andes using realistic geometries, *Proceedings of the 2011 IAG Symposium*, Melbourne, Australia, IAG Symposia, 139, in press.

Appendix

Abaqus file used for running reference model.

*Heading

** Job name: Fric_1_plastic_N_5E5yrs_C_O_velocity Model name: Model-1

** Generated by: Abaqus/CAE 6.10-EF1

*Preprint, echo=NO, model=NO, history=NO, contact=YES

**

** PARTS

**

*Part, name=Asth

*Element, type=C3D4

*Nset, nset=Asth_left

*Elset, elset=Asth_left

*Nset, nset=Asth_bottom

*Elset, elset=Asth_bottom

*Nset, nset=Asth, generate

*Elset, elset=Asth, generate

*Nset, nset=Asth_front

*Elset, elset=Asth_front

*Nset, nset=Asth_back

*Elset, elset=Asth_back

*Nset, nset=Asth_upper_spring

*Nset, nset=Asth_bottom_OC_line

*Nset, nset=Asth_node_spring, generate

*Surface, type=ELEMENT, name=Asth_OC

*Surface, type=ELEMENT, name=Asth_OC_e

```
** Section: Asth
**Solid Section, elset=Asth, material=Asth
,
*End Part
**
*Part, name=CC
*Element, type=C3D4
*Nset, nset=CC_right
*Elset, elset=CC_right
*Nset, nset=CC_upper_crust
*Elset, elset=CC_upper_crust, generate
*Nset, nset=CC_lower_crust
*Elset, elset=CC_lower_crust, generate
*Nset, nset=CC_mantle
*Elset, elset=CC_mantle, generate
*Nset, nset=CC_front
*Elset, elset=CC_front
*Nset, nset=CC_back
*Elset, elset=CC_back
*Nset, nset=CC_node_spring, generate
*Nset, nset=CC_right_mid_nodes
*Surface, type=ELEMENT, name=Locked
*Surface, type=ELEMENT, name=Updip
*Surface, type=ELEMENT, name=Downdip
*Surface, type=ELEMENT, name=CC_MW
*Surface, type=ELEMENT, name=CC_MW_e
*Surface, type=ELEMENT, name=UPdip_e
```

```
*Surface, type=ELEMENT, name=Locked_e
*Surface, type=ELEMENT, name=Downdip_e
*Surface, type=ELEMENT, name=CC_MW_e_master
** Section: CC_mantle
*Solid Section, elset=CC_mantle, material=CC_mantle
,
** Section: CC_lower
*Solid Section, elset=CC_lower_crust, material=CC_lower
,
** Section: CC_upper
*Solid Section, elset=CC_upper_crust, material=CC_upper
,
*End Part
**
*Part, name=MW
*Element, type=C3D4
*Nset, nset=MW_right
*Nset, nset=MW_right
*Nset, nset=MW_bottom
*Elset, elset=MW_bottom
*Nset, nset=MW, generate
*Elset, elset=MW, generate
*Nset, nset=MW-front
*Elset, elset=MW-front
*Nset, nset=MW_back
*Elset, elset=MW_back
*Nset, nset=MW_CC_spring
```

```
*Nset, nset=MW_slope_spring
*Nset, nset=MW_bottom_OC_line
*Nset, nset=MW_OC_spring
*Nset, nset=MW_node_spring, generate
*Surface, type=ELEMENT, name=MW_OC
*Surface, type=ELEMENT, name=MW_OC_e
*Surface, type=ELEMENT, name=MW_CC_e
** Section: Asth
*Solid Section, elset=MW, material=Asth
,*End Part
**
*Part, name=OC
*Element, type=C3D4
*Nset, nset=OC_left
*Nset, nset=OC_left
*Elset, elset=OC_left
*Nset, nset=OC_bottom
*Elset, elset=OC_bottom
*Nset, nset=Oceanic_crust
*Elset, elset=Oceanic_crust, generate
*Nset, nset=Oceanic_mantle
*Elset, elset=Oceanic_mantle
*Nset, nset=OC_front
*Elset, elset=OC_front
*Nset, nset=OC_back
*Elset, elset=OC_back
*Nset, nset=OC_MW_bottom_edge_X
```

```
*Nset, nset=OC_Asth_bottom_edge_X
*Nset, nset=OC_bottom_edge_mid_nodes
*Nset, nset=OC_MW_edge_line
*Nset, nset=OC_Asth_edge_line
*Nset, nset=OC_node_spring, generate
*Nset, nset=OC_bottom_mid_nodes
*Nset, nset=OC_left_mid_nodes
*Surface, type=ELEMENT, name=OC_Asth
*Surface, type=ELEMENT, name=OC_CC_MW_master
*Surface, type=ELEMENT, name=OC_Asth_e
*Surface, type=ELEMENT, name=OC_CC_MW_e
*Surface, type=ELEMENT, name=OC_Asth_e_upper
*Surface, type=ELEMENT, name=OC_asth_e_slope
*Surface, type=ELEMENT, name=OC_MW_e_slope
** Section: Oceanic_mantle
*Solid Section, elset=Oceanic_mantle, material=Oceanic_mantle
,
*Solid Section, elset=Oceanic_crust, material=Oceanic_crust
,
*End Part
**
**
** ASSEMBLY
**
*Assembly, name=Assembly
**
*Instance, name=Asth-1, part=Asth
```

*End Instance

**

*Instance, name=CC-1, part=CC

*End Instance

**

*Instance, name=MW-1, part=MW

*End Instance

**

*Instance, name=OC-1, part=OC

*End Instance

**

*Nset, nset=Back, instance=Asth-1

*Nset, nset=Back, instance=CC-1

*Nset, nset=Back, instance=OC-1

*Nset, nset=Back, instance=MW-1

*Elset, elset=Back, instance=Asth-1

*Elset, elset=Back, instance=CC-1

*Elset, elset=Back, instance=OC-1

*Elset, elset=Back, instance=MW-1

*Nset, nset=Front, instance=Asth-1

*Nset, nset=Front, instance=CC-1

*Nset, nset=Front, instance=OC-1

*Nset, nset=Front, instance=MW-1

*Elset, elset=Front, instance=Asth-1

*Elset, elset=Front, instance=CC-1

*Elset, elset=Front, instance=OC-1

*Elset, elset=Front, instance=MW-1

*End Assembly

**

** MATERIALS

**

*Material, name=Asth

*Density

3300.,

*Elastic

1.83e+11, 0.25

*Mohr Coulomb

10.,0.

*Mohr Coulomb Hardening

4e+07, 0.

5e+09, 0.01

*Material, name=CC_lower

*Density

2950.,

*Elastic

9.45e+10, 0.25

*Mohr Coulomb

20.,0.

*Mohr Coulomb Hardening

4e+07, 0.

5e+09, 0.01

*Material, name=CC_mantle

*Density

3300.,

*Elastic

1.83e+11, 0.25

*Mohr Coulomb

10.,0.

*Mohr Coulomb Hardening

4e+07, 0.

5e+09, 0.01

*Material, name=CC_upper

*Density

2750.,

*Elastic

8.25e+10, 0.25

*Mohr Coulomb

20.,0.

*Mohr Coulomb Hardening

4e+07, 0.

5e+09, 0.01

*Material, name=Oceanic_crust

*Density

3000.,

*Elastic

9.45e+10, 0.25

*Mohr Coulomb

20.,0.

*Mohr Coulomb Hardening

4e+07, 0.

5e+09, 0.01

*Material, name=Oceanic_mantle

*Density

3280.,

*Elastic

1.83e+11, 0.25

*Mohr Coulomb

10.,0.

*Mohr Coulomb Hardening

4e+07, 0.

5e+09, 0.01

**

** INTERACTION PROPERTIES

**

*Surface Interaction, name=Friction

1.,

*Friction, slip tolerance=0.005

0.14,

*Surface Behavior, direct

*Surface Interaction, name=No_friction

1.,

*Friction, slip tolerance=0.005

0.,

*Surface Behavior, direct

*INITIAL CONDITIONS, TYPE=STRESS, UNBALANCED STRESS=STEP,
INPUT=prestress_fric_0.14_plastic_N.inp

**

** BOUNDARY CONDITIONS

**

** Name: Asth_bottom Type: Symmetry/Antisymmetry/Encastre

*Boundary

Asth-1.Asth_bottom, ENCASTRE

** Name: Asth_left Type: Symmetry/Antisymmetry/Encastre

*Boundary

Asth-1.Asth_left, ENCASTRE

** Name: Back Type: Symmetry/Antisymmetry/Encastre

*Boundary

Back, ENCASTRE

** Name: CC_right Type: Symmetry/Antisymmetry/Encastre

*Boundary

CC-1.CC_right, ENCASTRE

** Name: Front Type: Symmetry/Antisymmetry/Encastre

*Boundary

Front, ENCASTRE

** Name: MW_bottom Type: Symmetry/Antisymmetry/Encastre

*Boundary

MW-1.MW_bottom, ENCASTRE

** Name: MW_right Type: Symmetry/Antisymmetry/Encastre

*Boundary

MW-1.MW_right, ENCASTRE

** Name: OC_bottom Type: Symmetry/Antisymmetry/Encastre

*Boundary

OC-1.OC_bottom, ENCASTRE

** Name: OC_left Type: Symmetry/Antisymmetry/Encastre

*Boundary

OC-1.OC_left, ENCASTRE

**

** INTERACTIONS

**

** Interaction: Asth_OC

*Contact Pair, interaction=No_friction, type=SURFACE TO SURFACE,
tracking=STATE, adjust=2.

OC-1.OC_Asth_e, Asth-1.Asth_OC_e

** Interaction: CC_MW

*Contact Pair, interaction=No_friction, type=SURFACE TO SURFACE,
tracking=STATE, adjust=2.

MW-1.MW_CC_e, CC-1.CC_MW_e_master

** Interaction: Downdip

*Contact Pair, interaction=No_friction, type=SURFACE TO SURFACE,
tracking=STATE, adjust=2.

CC-1.Downdip_e, OC-1.OC_CC_MW_e

** Interaction: Locked

*Contact Pair, interaction=Friction, type=SURFACE TO SURFACE,
tracking=STATE, adjust=2.

CC-1.Locked_e, OC-1.OC_CC_MW_e

** Interaction: MW_OC

*Contact Pair, interaction=No_friction, type=SURFACE TO SURFACE,
tracking=STATE, adjust=2.

MW-1.MW_OC_e, OC-1.OC_CC_MW_e

** Interaction: Updip

*Contact Pair, interaction=No_friction, type=SURFACE TO SURFACE,
tracking=STATE, adjust=2.

CC-1.UPdip_e, OC-1.OC_CC_MW_e

```
** -----  
  
**  
  
** STEP: Step-1  
  
**  
  
*Step, name=Step-1, nlgeom=YES, unsymm=YES  
  
*Static  
  
1., 1., 1e-05, 1.  
  
**  
  
** BOUNDARY CONDITIONS  
  
**  
  
** Name: Asth_bottom Type: Symmetry/Antisymmetry/Encastre  
  
*Boundary, op=NEW  
  
** Name: Asth_bottom_movement Type: Symmetry/Antisymmetry/Encastre  
  
*Boundary, op=NEW  
  
Asth-1.Asth_bottom, XASYMM  
  
** Name: Asth_left Type: Symmetry/Antisymmetry/Encastre  
  
*Boundary, op=NEW  
  
** Name: Asth_left_movement Type: Symmetry/Antisymmetry/Encastre  
  
*Boundary, op=NEW  
  
Asth-1.Asth_left, YASYMM  
  
** Name: Back Type: Symmetry/Antisymmetry/Encastre  
  
*Boundary, op=NEW  
  
** Name: Back_movement Type: Symmetry/Antisymmetry/Encastre  
  
*Boundary, op=NEW  
  
Back, YASYMM  
  
** Name: CC_right Type: Symmetry/Antisymmetry/Encastre  
  
*Boundary, op=NEW
```

** Name: CC_right_movement Type: Symmetry/Antisymmetry/Encastre

*Boundary, op=NEW

CC-1.CC_right, YASYMM

** Name: Front Type: Symmetry/Antisymmetry/Encastre

*Boundary, op=NEW

** Name: Front_movement Type: Symmetry/Antisymmetry/Encastre

*Boundary, op=NEW

Front, YASYMM

** Name: MW_bottom Type: Symmetry/Antisymmetry/Encastre

*Boundary, op=NEW

** Name: MW_bottom_movement Type: Symmetry/Antisymmetry/Encastre

*Boundary, op=NEW

MW-1.MW_bottom, XASYMM

** Name: MW_right Type: Symmetry/Antisymmetry/Encastre

*Boundary, op=NEW

** Name: MW_right_movement Type: Symmetry/Antisymmetry/Encastre

*Boundary, op=NEW

MW-1.MW_right, YASYMM

** Name: OC_bottom Type: Symmetry/Antisymmetry/Encastre

*Boundary, op=NEW

** Name: OC_bottom_movement Type: Symmetry/Antisymmetry/Encastre

*Boundary, op=NEW

OC-1.OC_bottom, XASYMM

** Name: OC_left Type: Symmetry/Antisymmetry/Encastre

*Boundary, op=NEW

** Name: OC_left_movement Type: Symmetry/Antisymmetry/Encastre

*Boundary, op=NEW

OC-1.OC_left, YASYMM

**

** LOADS

**

** Name: Gravity Type: Gravity

*Dload

, GRAV, 9.8, 0., -1., 0.

**

** OUTPUT REQUESTS

**

*Restart, write, frequency=1

*Print, solve=NO

**

** FIELD OUTPUT: F-Output-1

**

*Output, field

*Node Output

CF, COORD, RF, U, V

*Element Output, directions=YES

E, EE, ER, IE, LE, MISES, NE, PE, PEEQ, PEEQT, PEMAG, PRESSONLY, PS,
S

*Contact Output

CDISP, CSTRESS

**

** HISTORY OUTPUT: H-Output-1

**

*Output, history, variable=PRESELECT

*End Step

** -----

**

** STEP: Step-2

**

*Step, name=Step-2, nlgeom=YES, amplitude=RAMP, inc=1000, unsymm=YES

*Visco, cetol=0.01

1.575e+13, 1.575e+13, 1e-07, 1.575e+13

**

** BOUNDARY CONDITIONS

**

** Name: Asth_bottom_movement Type: Symmetry/Antisymmetry/Encastre

*Boundary, op=NEW

Asth-1.Asth_bottom, XASYMM

** Name: Asth_left_movement Type: Symmetry/Antisymmetry/Encastre

*Boundary, op=NEW

**Name: Asth_left_velocity_movement Type: Symmetry/Antisymmetry/Encastre

*Boundary, op=NEW

Asth-1.Asth_left, ENCASTRE

** Name: Back_movement Type: Symmetry/Antisymmetry/Encastre

*Boundary, op=NEW

Back, YASYMM

** Name: CC_right_movement Type: Symmetry/Antisymmetry/Encastre

*Boundary, op=NEW

** Name: CC_right_velocity_3cm_yr Type: Velocity/Angular velocity

*Boundary, op=NEW, type=VELOCITY

CC-1.CC_right_mid_nodes, 1, 1, -9.52e-10

** Name: CC_right_velocity_movement Type: Symmetry/Antisymmetry/
Encastre

*Boundary, op=NEW

CC-1.CC_right, XASYMM

** Name: Front_movement Type: Symmetry/Antisymmetry/Encastre

*Boundary, op=NEW

Front, YASYMM

** Name: MW_bottom_movement Type: Symmetry/Antisymmetry/Encastre

*Boundary, op=NEW

MW-1.MW_bottom, XASYMM

** Name: MW_right_movement Type: Symmetry/Antisymmetry/Encastre

*Boundary, op=NEW

** Name: MW_right_velocity_movement Type: Symmetry/Antisymmetry/
Encastre

*Boundary, op=NEW

MW-1.MW_right, ENCASTRE

** Name: OC_bottom_movement Type: Symmetry/Antisymmetry/Encastre

*Boundary, op=NEW

** Name: OC_bottom_velocity_movement Type: Symmetry/Antisymmetry/
Encastre

*Boundary, op=NEW

OC-1.OC_bottom, ZSYMM

** Name: OC_left_movement Type: Symmetry/Antisymmetry/Encastre

*Boundary, op=NEW

** Name: OC_left_velocity_movement Type: Symmetry/Antisymmetry/Encastre

*Boundary, op=NEW

OC-1.OC_left, XASYMM

** Name: Slab_push_velocity Type: Velocity/Angular velocity

```
*Boundary, op=NEW, type=VELOCITY
OC-1.OC_left_mid_nodes, 1, 1, 1.59e-09
** Name: Slab_pull_velocity Type: Velocity/Angular velocity
*Boundary, op=NEW, type=VELOCITY
OC-1.OC_bottom_mid_nodes, 1, 1, 1.51e-09
OC-1.OC_bottom_mid_nodes, 2, 2, -5.02e-10
**
** OUTPUT REQUESTS
**
*Restart, write, frequency=0
*Print, contact=YES, model change=YES, plasticity=YES, solve=YES
**
** FIELD OUTPUT: F-Output-1
**
*Output, field, number interval=20
*Node Output
CF, COORD, RF, U, V
*Element Output, directions=YES
E, EE, ER, IE, LE, MISES, NE, PE, PEEQ, PEEQT, PEMAG, PRESSONLY, PS,
S
*Contact Output
CDISP, CSTRESS
**
** HISTORY OUTPUT: H-Output-1
**
*Output, history, variable=PRESELECT
*End Step
```

Acknowledgements

Apart from the efforts of myself, the completion of this work depends on the encouragement and guidelines of many others. I take this opportunity to express my gratitude to the people whose assistance and guidance helps in the completion of this project.

First of all, I would like to express my sincere gratitude to my supervisor PD Dr. Thomas Jahr and Prof. Dr. Gehard Jentzsch for providing me the opportunity to work on this project. Their precious time, kind support, trust and passions enabled me to accomplish this work. I would also like to acknowledge Prof. Dr. Hans-Jürgen Götze with much appreciation for his insightful hints and discussion. Furthermore, I am deeply grateful to Prof. Dr. Peter Malischewsky for his keen support and guidance. I would also like to express my gratitude to DFG for the financial support.

I would like to offer my special thanks to Dr. Adelheid Weisse, for her continuous support and sharing daily life experiences. I would like to thanks Stefanie Zeumann for her helpful comments and suggestions.

I would like to express my gratitude to the whole working group of “Applied Geophysics” and the other colleagues of the Institute of Geoscience.

I would like to thanks all project partners of University of Kiel and TU Munich: Benjamien Gutknecht, Dr. Martin Horwath, Michael Hosse, Nils Köther, Oscar Lücke, Rezene Mahatsente, Prof. Dr. Roland Pail for their helpful discussions.

I am indebt to my husband, Sudhir Kumar, without his persistent support and guidance this dissertation would not have been possible and my son, Siddharth Kumar, who was born before the completion of this dissertation and spent a lot of time apart from me. I would like to give a special thanks to my parents and to my in-laws, who have always support, and encourage me.

Lastly, I would like to thank to my brother, sister and to their extended family for their support and encouragement.

Selbständigkeitserklärung

Ich erkläre, dass ich die vorliegende Arbeit selbständig und unter Verwendung der angegebenen Hilfsmittel, persönlichen Mitteilungen und Quellen angefertigt habe.

Jena, den 9 October 2013

Rekha Sharma